

AD\_\_\_\_\_

Award Number: DAMD17-03-1-0480

**TITLE:** Theoretical Modeling of Molecular Mechanisms, Time Scales, and Strains in Prion Diseases

**PRINCIPAL INVESTIGATOR:** Daniel L. Cox, PhD.  
Rajiv R.P. Singh

**CONTRACTING ORGANIZATION:** University of California, Davis  
Davis, CA 95616-8671

**REPORT DATE:** July 2006

**TYPE OF REPORT:** Final

**PREPARED FOR:** U.S. Army Medical Research and Materiel Command  
Fort Detrick, Maryland 21702-5012

**DISTRIBUTION STATEMENT:** Approved for Public Release;  
Distribution Unlimited

The views, opinions and/or findings contained in this report are those of the author(s) and should not be construed as an official Department of the Army position, policy or decision unless so designated by other documentation.

# REPORT DOCUMENTATION PAGE

Form Approved  
OMB No. 0704-0188

Public reporting burden for this collection of information is estimated to average 1 hour per response, including the time for reviewing instructions, searching existing data sources, gathering and maintaining the data needed, and completing and reviewing this collection of information. Send comments regarding this burden estimate or any other aspect of this collection of information, including suggestions for reducing this burden to Department of Defense, Washington Headquarters Services, Directorate for Information Operations and Reports (0704-0188), 1215 Jefferson Davis Highway, Suite 1204, Arlington, VA 22202-4302. Respondents should be aware that notwithstanding any other provision of law, no person shall be subject to any penalty for failing to comply with a collection of information if it does not display a currently valid OMB control number. PLEASE DO NOT RETURN YOUR FORM TO THE ABOVE ADDRESS.

1. REPORT DATE 01-07-2006	2. REPORT TYPE Final	3. DATES COVERED 15 Jun 2003 – 14 Jun 2006		
4. TITLE AND SUBTITLE  Theoretical Modeling of Molecular Mechanisms, Time Scales, and Strains in Prion Diseases		5a. CONTRACT NUMBER		
		5b. GRANT NUMBER DAMD17-03-1-0480		
		5c. PROGRAM ELEMENT NUMBER		
6. AUTHOR(S) Daniel L. Cox, PhD. Rajiv R.P. Singh  E-Mail:		5d. PROJECT NUMBER		
		5e. TASK NUMBER		
		5f. WORK UNIT NUMBER		
7. PERFORMING ORGANIZATION NAME(S) AND ADDRESS(ES)  University of California, Davis Davis, CA 95616-8671		8. PERFORMING ORGANIZATION REPORT NUMBER		
9. SPONSORING / MONITORING AGENCY NAME(S) AND ADDRESS(ES) U.S. Army Medical Research and Materiel Command Fort Detrick, Maryland 21702-5012		10. SPONSOR/MONITOR'S ACRONYM(S)		
		11. SPONSOR/MONITOR'S REPORT NUMBER(S)		
12. DISTRIBUTION / AVAILABILITY STATEMENT Approved for Public Release; Distribution Unlimited				
13. SUPPLEMENTARY NOTES Original contains colored plates: ALL DTIC reproductions will be in black and white.				
14. ABSTRACT We have obtained significant results modeling: (1) the structure of the minimal infectious prion oligomer as a domain swapped beta helical trimer; (2) metal binding to the prion protein showing results consistent with measured affinities and suggesting a detailed molecular role for the protection of the normal prion form against conversion to the infectious scrapies form when copper is bound to a particular site; (3) kinetics of yeast prion aggregation in vitro illustrating the role of fission; (4) kinetic analysis of transgenic mice time course data for anchorless cellular prions, indicating (a) that the membrane is necessary for exponential growth of infectious aggregate, and (b) that the elongation rate of anchorless prions is likely more rapid than anchored ones. In the coming year we will explore the role of our domain swapped model for 1) understanding strains, 2) understanding a subset of point mutations known to induce disease for those who inherit them, 3) possible docking of octarepeats to the beta helical trimers and their role in prion conversion, 4) additional metal binding to the prion protein (iron, sodium, and copper at H111), and (5) the role of the membrane in inducing exponential growth of infectivity.				
15. SUBJECT TERMS Theory/simulations; domain swapping; metal binding and protection; Strain modeling; conversion modeling; kinetics modeling				
16. SECURITY CLASSIFICATION OF:  a. REPORT U		17. LIMITATION OF ABSTRACT UU	18. NUMBER OF PAGES 74	19a. NAME OF RESPONSIBLE PERSON USAMRMC
b. ABSTRACT U				19b. TELEPHONE NUMBER (include area code)
c. THIS PAGE U				

## Table of Contents

<b>Cover.....</b>	<b>1</b>
<b>SF 298.....</b>	<b>2</b>
<b>Table of Contents.....</b>	<b>3</b>
<b>Introduction.....</b>	<b>4</b>
<b>Body.....</b>	<b>4</b>
<b>Key Research Accomplishments/Future Research.....</b>	<b>5</b>
<b>Reportable Outcomes.....</b>	<b>15</b>
<b>Conclusions.....</b>	<b>16</b>
<b>References.....</b>	<b>16</b>
<b>Appendices.....</b>	<b>18</b>

## Introduction

In this final year of our award, we have made significant progress on several areas of theoretical research on the prion problem, particularly on a promising new model for the in vitro mammalian prion fibril which involves a new suggestion for a C-terminal region left handed beta helix. We have also made progress on exploring other domain swapped structures for oligomers and on the role of mutations in our domain swapped prion trimer model. Overall on the award, we have accomplished much: (i) published seven papers and one PhD dissertation (two more are in the works this year), (ii) presented 27 invited lectures at universities or meetings and ten contributed talks at conferences; (iii) co-organized two major international workshop on amyloid diseases (the last being <http://i2cam.org/i2camyloid>); (iv) received national press coverage for our research on prion diseases (see the attached item in Appendix J); (v) received fellowship honors for the participants (a Guggenheim for the PI, a Kevli fellowship at the Kevli Institute for Theoretical Physics of UC Santa Barbara for former student David Mobley, and two fellowships for finishing student Jianping Pan).

We anticipate 2-3 more papers emerging from the final year of research on this grant and we detail those areas of progress in the report that follows, focusing on the above mentioned work on a new model for in vitro grown fibrils, new domain swapped oligomer models, and models of the influence of proline mutations on the kinetics of formation of the domain swapped prion trimer.

## Key Research Accomplishments During the Award Period

1. ***Modeling of Oligomeric Intermediates in prion aggregation.*** See App. B, manuscript published in Biophysical Journal.
2. ***Modeling of insertion of Abeta peptides in model membranes.*** See App. C, manuscript published in Biophysical Journal.
3. ***Dissertation on modeling of prions and Abeta.*** See App. D, directions to online copy of dissertation by David Mobley, with strong review chapter.
4. ***Proposing a new structure for the minimal infectious unit of prion disease: the Domain Swapped Prion Trimer (DSTP).*** See App. E, manuscript of paper published in FASEB Journal.
5. ***Demonstration of the necessity of the membrane in exponential in vivo growth of prion infectivity.*** See App. F, manuscript published in the Letters section of Biophysical Journal.
6. ***Possible mechanism for copper inhibition of prion conversion.*** See App. G, manuscript published in the Letters section of Biophysical Journal.

7. **Detailed modeling of in vitro yeast prion aggregation** See App. H, manuscript of paper published in Phys. Rev. E.

8. **Review of amyloidogenic proteins from a materials perspective.** See App. I, published in Materials Research Bulletin.

### Research Accomplishments during final term of support

***Modeling of in vitro fibrils with left handed beta helices.***

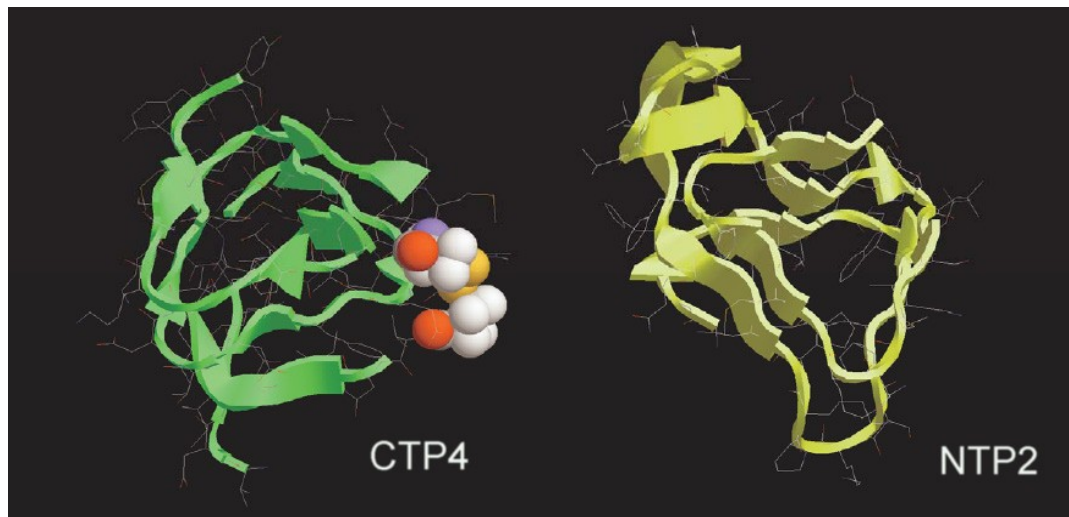


**Figure 1:** Ribbon representations of the nearly four turn C-terminal LH $\beta$ H model (CTP4) and the nearly two turn N-terminal LH $\beta$ H (NTP2) model. Notable in CTP4 is the disulfide bond (cysteines highlighted), and in NTP2 the removed hydrophobic loop of dominant glycine and alanine character. Figures drawn with RASTOP.

Recent work<sup>1</sup> on *in vitro* grown mammalian prion fibrils in low pH shows electron microscopy evidence for prion fibrils with twinned crosslinked filaments, possessing repeat units with lengths consistent with twelve beta strands perpendicular to the fibrillar axis, no alpha helical structure, and no strong evidence for inter-monomer disulfide bonds between cysteines. The cross sectional diameter of the filaments is of order 25-35 angstroms, and the linkers between the filaments are of length 50-60 angstroms. There is a gap of order 8-15 angstroms between these repeat units which is thus likely devoid of beta sheet bonding. The cross linked regions are electron rich and approximately twice as wide as the ``empty'' regions between filaments. These facts alone allow us to begin to build a powerful empirical case for LH $\beta$ H structure to the filaments. We note the following observations:

- With the inclusion of side chains pointing to the outside, it is easy to see that the cross sectional size of LH $\beta$ H motifs are of the order of 25-35 angstroms.
- The two versions of LH $\beta$ H trimers proposed already for the structures of prion oligomers<sup>2,3</sup> contain LH $\beta$ H structures in each monomer on the N-terminal side of the truncated prion protein with 3 beta helical turns in residues 90-144.
- The remnant alpha helical portions of the original LH $\beta$ H trimer model has 63 residues between the structure disrupting proline at residue 165 and the terminal glutamine at residue 228, easily enough to accommodate three full LH $\beta$ H turns.
- The two cysteines with a disulfide bond are at residues 179 and 214 respectively, differing by 35 residues or almost two full turns of a LH $\beta$ H. Indeed, assuming the cysteines are at LH $\beta$ H corners, there is no difficulty in accommodating the intra-monomer disulfide bond. This requirement fixes the three turn C LH $\beta$ H threading to within 1-2 residues.
- The 21 residue linking region between residues 145 and 165 is, fully extended, approximately 60 angstroms and thus of sufficient length to explain the observed cross links.

This suggests that we can build a model in which each filamentary repeat is composed of two N-terminal and two C-terminal derived LH $\beta$ H s such that they add to give six turns. Fig. (1) illustrates an example of such LH $\beta$ H s, in which the C- LH $\beta$ H has almost four turns (CTP4) and the N- LH $\beta$ H has just over two turns (NTP2). In order to provide enhanced stability relative to the threading of the prion trimer models mentioned earlier, we have pulled out a predominant G-A loop which contains the putative transmembrane segment of the prion protein<sup>(4)</sup>. We have also considered fibril models built from three turns at the C-terminal (CTP3) and from taking the three turn LH $\beta$ H of the miniprion trimer model for the N-terminal LH $\beta$ H (NTP3).

There is considerable latitude in building a suitable model. Figure (2) gives an illustration, which shows how we can get into the right general region of model space to describe the fibrils by stacking in an overall prion tetramer the C and N terminal LH $\beta$ H s (C LH $\beta$ H and N LH $\beta$ H) with the arrow denoting the n-to-c terminal sense of the helix. The individual monomers are color coded in the schematic diagram and in the ribbon diagram. The difference between the two schematics is the sense of the filaments; on the left, they stack in the same sense, while on the right they stack in opposite sense.

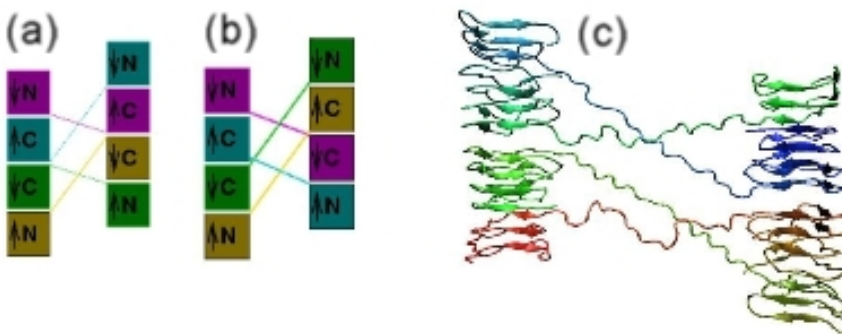


**Figure 2:** Sample models of mammalian prion fibril repeat units. (a) shows same sense filaments with color coding indicating the partner CLH $\beta$ H/NLH $\beta$ H structures from a given monomer; (b) shows antisense filaments; (c) is a ribbon rendering of model (a) generated within VMD using CTP3 and NTP3 models for the C and N terminal LH $\beta$ Hs. Image of (c) created with VMD.

A separate degree of freedom is the number of turns per helix; we have considered both 3 and 4 turn CLH $\beta$ H (abbreviated CTP3 [residues 178-226 of human PrP], CTP4 [residues 166-216 of human PrP]) and 2 and 3 turn NLH $\beta$ H (abbreviated NTP2 [residues 90-145 of human PrP], NTP3 [residues 90-145 of human PrP]). NPT3 is the three turn region taken from the proposed LH $\beta$ H trimer model, while NPT2 is a new model we have produced in which we extract a loop [residues 114-126 of human PrP] of predominantly glycine and alanine residues known to belong to the section of the prion which can cross the membrane [residues 111-134 of human PrP]<sup>4</sup>. We find that the NPT3 LH $\beta$ H by itself is very unstable, in large part due to the poor packing of the middle layer which contains substantial glycine and alanine content, and due to poor side-chain to side-chain hydrogen bonding. As discussed below the NPT2 LH $\beta$ H is, apart from the fluctuating loop region, as stable as the two CLH $\beta$ H models, and contains reasonable side-chain to side-chain hydrogen bonding.

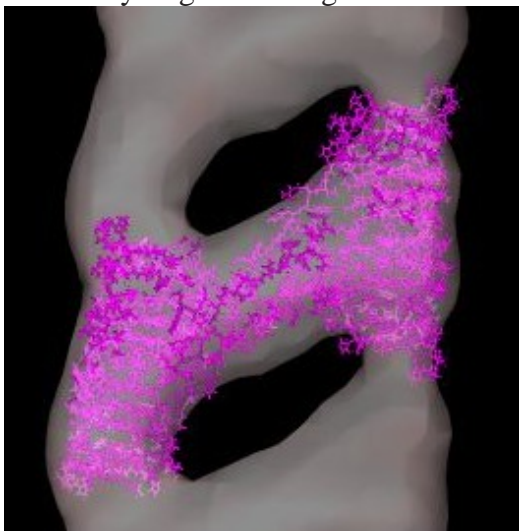


**Fig 3:** Embedding of model tetramer composed of NTP2, CTP4 LH $\beta$ Hs plus connecting loops in experimental density data of Ref. 1 Image created with Chimera.

Fig. (3) shows a model in which we employed approximate mirror symmetry to agree with the densities of the 1200 angstrom helix of Ref. (1). If we make the assumption that the N-terminal region of the NLH $\beta$ H mirrors across the gap of the density, then we can see that the clumping of the cross links gives rise to a low/high density variation similar to that seen in experiment. An attractive feature of this model is that previously proposed domain swapping using the proline containing loop (K101-P105)(see Ref. 3) across the gap is possible and can be a stabilizing feature.

The space of exploration is relatively large even within this simplified model in that we can vary

- over four relative sense orientations in each filament of the tetramer (in addition to that shown, there are C $\uparrow$ N $\uparrow$ N $\downarrow$ C $\downarrow$ , C $\uparrow$ N $\downarrow$ N $\uparrow$ C $\downarrow$ , and N $\uparrow$ C $\uparrow$ C $\downarrow$ N $\downarrow$ ).
- The filaments can run in antisense to one another as shown in the figure.

- In addition to the long filament domain swapping associated with loops between NLH $\beta$ Hs and CLH $\beta$ Hs, there can be domain swapping between adjacent NLH $\beta$ Hs of the type discussed in Ref.(3)
- The orientation of the triangular cross section of the beta helix is not readily determined by the available data though it is constrained by the aspect ratio of the density cuts.
- There is flexibility on how many turns to include in the CLH $\beta$ H and NLH $\beta$ H.

An important key to assessing the model on theoretical grounds is the issue of the stability of the CLH $\beta$ H. We show in Fig. (4) the RMSDs from selected three turn segments of five LH $\beta$ Hs from the PDB together with the CTP3, CTP4, and NTP2 models of LH $\beta$ Hs from our work. The short time frame for the simulation is not intended to confirm stability in any real sense, but rather to be comparative with known structures, for which the RMSD ranges from 1-3 Angstroms. (The NTP3 model drawn from existing prion trimer structure models It is clear that these preliminary, unoptimized prion models are, in this measure, within the range of viability suggested by known stable structures. In particular, the CTP3 model looks quite promising. We suspect this is facilitated by (i) excellent side chain-to-side chain hydrogen bonding, and (ii) added stability from the covalent disulfide bond between the cysteines.

Our plan is to examine those models which have the best overall chance of describing the fibril data, and then optimize the factors above to give the best agreement with experiment using construction programs, electron density map generation with EMAN and electron density map optimization and visualization via tools in the CHIMERA package. We will then prepare all atom AMBER MD runs for octamers of prion protein to ensure that we build in the gap region and validate the stability with relatively low RMSD from the starting structure (1-2 angstroms).

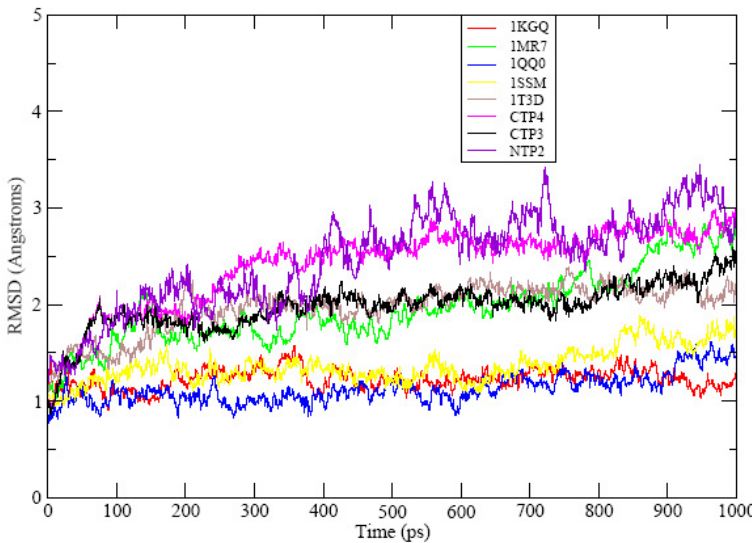


**Figure 4:** RMSD from starting structure in all atom Amber MD runs (npt at 300K) for five LH $\beta$ Hs from the PDB, and for the 3 and 4 turn C-terminal (CTP3, CTP4) and 2 turn N-terminal (NTP2) LH $\beta$ H models discussed here. For the PDB proteins, starting structures were the posted coordinate files.

We note that the conformational diversity obvious within these fibril models may have some relevance to the conformational diversity observed both *in vitro*<sup>5</sup> and in the prion strains. We are particularly intrigued by the notable stability of the CTP3 and CTP4

models in the following sense: small amounts of these structures could play significant templating roles both *in vivo* and *in vitro*. To satisfy the general constraint about the amount of alpha helical content in infectious material, which must derive from the C-terminal region, we cannot have large amounts present from purified brain extracts. On the other hand, the relatively small amount of proteinase resistant material found in many strains by conformation dependent immunoassay<sup>6</sup> may point to a critical role for these CLH $\beta$ Hs in disease propagation, since it is C-terminal stretches that provide the proteinase resistant core in synthesized fibrils<sup>7,8</sup>.

**Stabilization of LH $\beta$ Hs.** A fundamental question we need to address is ``what stabilizes the beta-helices?'' There is an obvious cost to these structures as making the beta helices requires bends or turns in the beta strands, so they can wrap on top of each other allowing the formation of backbone Hydrogen bonds. These turns can be gradual as in Perutz's proposal of a circular beta-helix<sup>9</sup>, or, they can be sharp, as in the triangular beta-helices commonly found in the protein databases<sup>10,11</sup>. In either case, these deviations from planar structure cost torsional energy and can reduce the strength of the backbone hydrogen bonds. Thus, one needs other factors that can compensate for this increase in energy and help stabilize the beta-helical structure.

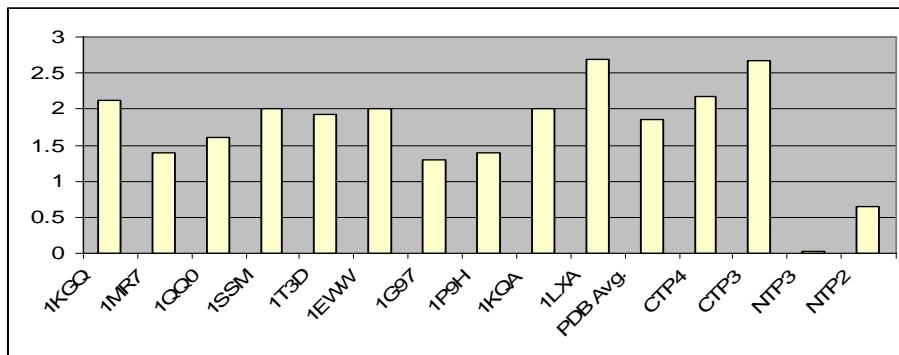


**Figure 5 :** Side chain-to-side chain hydrogen bonds per turn for a number of LH $\beta$ Hs from the Protein Data Bank, together with our C-terminus and N-terminus LH $\beta$ H models (CTP4, CTP3, NTP3, NTP2)

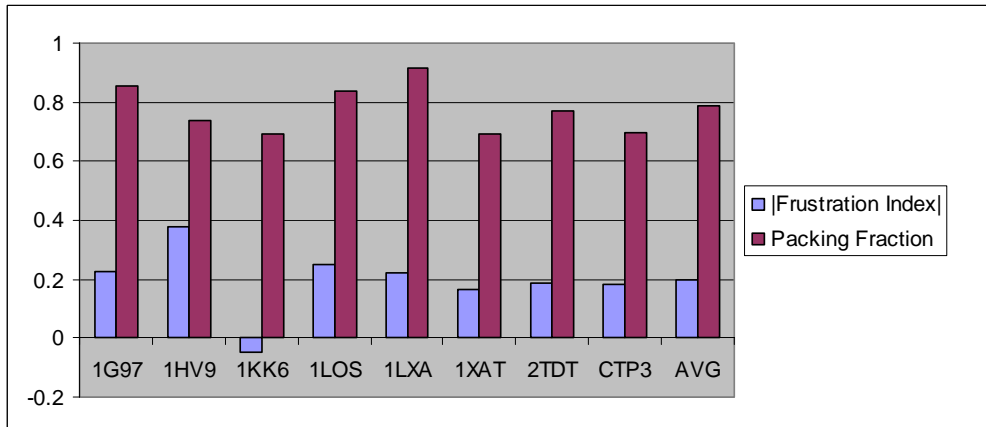


**Figure 6:** Frustration index (CTP4, CTP3, NTP3, NTP2)  $|N_m|$  and packing fraction  $p_f$  for several LH $\beta$ Hs from the PDB along with the three turn C-terminal LH $\beta$ H model discussed in this proposal. AVG is the average of these quantities for the PDB proteins.

Studying the beta-helical structures in the protein databases, we have found three important stabilizing effects:

1. *Side-chain Hydrogen Bonding:* The beta-helix structure allows side-chain to side-chain

as well as side-chain to backbone Hydrogen bonding, for suitably placed residues. We show in Fig. (5) that the CTP3, CTP4 models have superior side chain bonding near the best of selected LH $\beta$ Hs from the PDB, while the as-threaded NTP3 used in modeling prion oligomers has essentially no side chain-to-side chain hydrogen bonding which may account for its relative instability. This situation is substantially improved in the NTP2 model with the extruded loop.

2. *Good packing of the hydrophobic interior:* The known beta-helices pack the interior of the helix rather well and are very compact. This can also lead to a substantially lower free energy for the structure. This is illustrated quantitatively in Fig. (6) for seven LH $\beta$ Hs from the PDB and the CTP3 model. This shows that the CTP3 model is at the low end of packing fractions for known stable LH $\beta$ Hs. The situation is visualized in Fig. (7) which shows a comparison of the packing in three turns of the beta helix labeled 1KGQ on the PDB, and the CTP3 and NTP3 models, where we have placed one angstrom spheres around each atom. Clearly 1KGQ has better packing, but the CTP3 and NTP3 models are not substantially worse.

3. *Good matching of hydrophobic residues in the interior and hydrophilic residues in the exterior of the beta-helix:* By reducing any mismatches of hydrophobic and hydrophilic residues the beta-helix structure can gain substantial stability. Fig. (6) shows a comparison of seven LH $\beta$ Hs from the PDB together with the CTP3 model. On this account, the CTP3 model is in very reasonable accord with known stable structures.

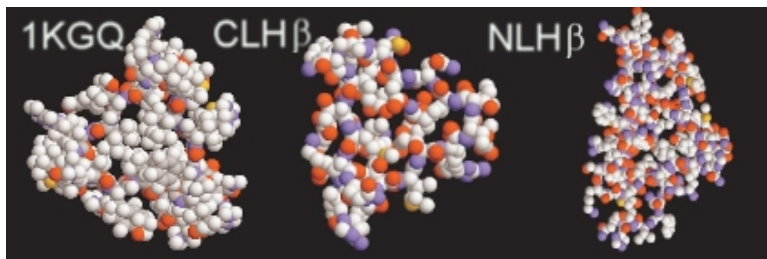


**Figure 7:** Top view of internal packing of three turn segments of LH $\beta$ Hs. Three turns have been taken from 1KGQ on the PDB, and the three turn CLH $\beta$ H and NLH $\beta$ H models for the prion protein are shown. In each case, one angstrom spheres are centered on each atom. Drawings rendered by RASTOP.

These observations are less pertinent to a homo-peptide such as poly-glutamine, but for a hetero-peptide such as part of the prion protein or A-beta peptide, this suggests that any proposal for a threading of a sequence onto a beta-helical structure should take these factors into consideration. Here, we propose to develop a scheme for finding stable beta-helical structures, for different sequences, guided by the known structures in the databases.

In threading a peptide sequence onto a beta-helical structure, there is some flexibility as to which peptide is placed in which location. This flexibility is further increased, when loops are set aside that can take on a non-beta structure. We plan to use the following strategy to obtain stable beta-helix structures given a peptide sequence. First, we will use standard programs to thread the peptide sequence onto the beta-helical structure, including selecting the loop regions which will have non beta-strand dihedral angles. For

this trial structure, after some energy minimization within, e.g., the Amber package, we will measure the number of side-chain Hydrogen bonds  $N_s$ , the packing fraction  $p_f$  (defined as the ratio of the enclosed side chain volume to the volume of the subtended triangular prism), and the number of satisfied Hydrophilic-Hydrophobic matches  $N_m$ , in the beta-helical region. ( $N_m$  is defined as the number of polar/charged residues pointing out of the helix minus those pointing into the helix plus the number of hydrophobic residues pointing into the helix minus the number pointing out of the helix.) We define a dimensionless scoring function  $\rho$ , with  $\langle N_s \rangle$ , e.g., the mean of  $N_s$  from LH $\beta$ Hs of the PDB,

$$\rho = -(N_s/\langle N_s \rangle + p_f/\langle p_f \rangle + N_m/\langle N_m \rangle)/3$$

By normalizing each of the three variables to their mean values, we equally weight their importance. Obviously we can explore other weighting procedures as we consider simulations on LH $\beta$ H structures. The lower the score, the more stable the structure. Note that the sign is positive for  $N_m$  in the score as lower  $N_m$  will be more stable. The mean  $\rho$  score for the structures in the database is -1, and its variance is, assuming no correlations between  $N_s$ ,  $N_m$ , and  $p_f$ , and with, e.g.,  $\Delta N_m$  the variance of  $N_m$

$$\Delta \rho^2 = (\Delta N_s^2/\langle N_s \rangle^2 + \Delta p_f^2/\langle p_f \rangle^2 + \Delta N_m^2/\langle N_m \rangle^2)/9.$$

If we find that the score for a trial threaded structure is within  $\Delta \rho$  of -1, it is a good candidate beta-helical structure, and will be explored more closely through a full Molecular Dynamics simulation. If it has a higher score, it is unlikely to be stable and will be rejected. We plan to use this scheme to obtain stable beta-helical threading for various known amyloid proteins. We will test the scheme for (i) independence of the main scoring variables, (ii) correlations between particular residue frequencies in the PDB and good values of  $\rho$ , and (iii) intra-molecular correlations among residues.

With the specific examination of the NLH $\beta$ H, if we are unable to stabilize via rethreading, we will explore the possibility that extrinsic perturbations, especially in the form of a membrane, might provide the necessary stability. In this case we will attempt first to model the membrane as a mean field with mildly negative surface charge drawing upon our experience in modeling A $\beta$ 40-42 insertion in membranes<sup>12</sup>. In particular, we will investigate how well the G-A loop in the NTP2 model can insert into the membrane, and will update the simulation model, which is biased towards alpha helices, to allow for formation of beta structure outside.

***Disposition to prion disease by point mutations.*** With our domain swapped prion trimer model, the short loop K101-P105 has special significance in terms of gluing the oligomer together. This is also potentially relevant to fibril growth as discussed earlier in this section. Two of the point mutations which dispose individuals to get the inherited GSS form of prion disease involve the mutation of prolines for leucines on this loop (P102L and P105L), and one reported inherited form of Creutzfeldt-Jakob Disease involves the mutation P105T<sup>13</sup>. We note that these mutations can promote enhanced conversion from cellular prion to scrapies form by at least two effects: (i) any substitution for proline in

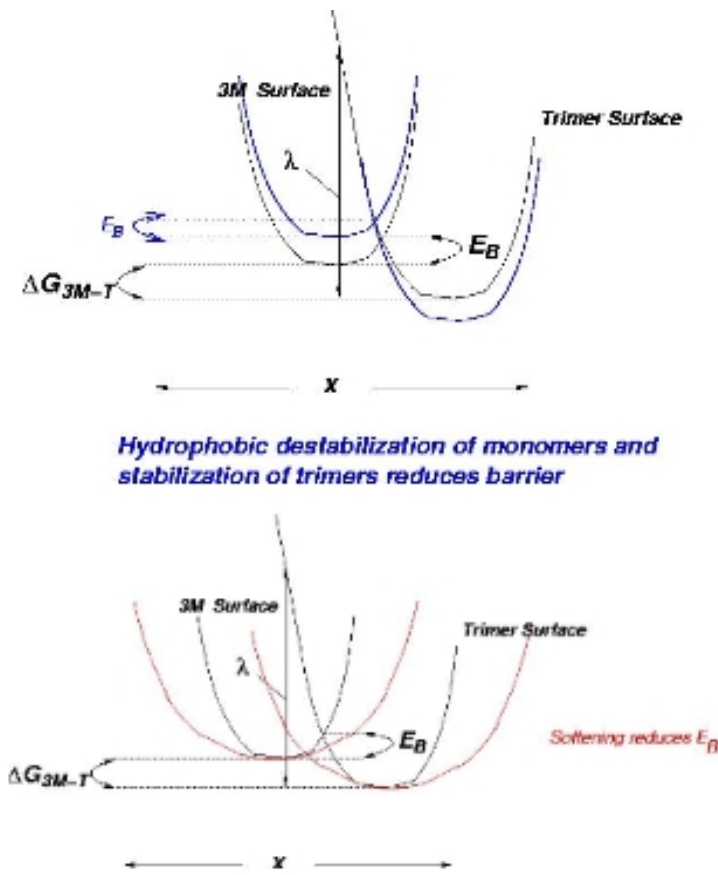
these loops will make them more flexible and hence more likely to convert rapidly if this conversion is important to stabilizing the aggregate, which is true of both the domain swapped oligomers and fibrils and (ii) these substitutions as well as artificial ones studied in transgenic mice by Nazor *et al*<sup>14</sup> are relatively hydrophobic to proline, which means they are inherently destabilizing to the nominal random coil of the wild type cellular form, while if there is favorable water exclusion by hydrophobic clustering in the core of the domain swapped oligomers then the energy surface from cellular prion form to aggregate will be ramped further. We have made a preliminary examination of the influence of mutants on the loop flexibility as measured by the associated B factors, defined for a given atom as  $B = 8\pi\langle u^2 \rangle/3$ .

Fig. (8) illustrates schematically within a simple two-state model how the simultaneous hydrophobic destabilization of the wild type protein and hydrophobic stabilization of the domain swapped trimer can ramp the energy surface to lower the energy barrier and speed the conversion reaction. Obviously this naïve picture ignores intermediates, but we anticipate that even in this case the partial hydrophobic protection which might arise in the domain swapped model can enhance the conversion rate. Fig. (8) also illustrates how the relative softening of the loop can enhance the rate by again reducing the energy barrier. This assumes that the bending stiffness of the loop with proline or mutant participate in the reaction coordinate involved in conversion.

Fig. (9) below shows a preliminary examination of the B-factor for the domain swapped prion trimer model. Uniform substitutions at the three proline containing loops were made, and the LH $\beta$ Hs were restrained while the loops were left free to fluctuate. While there is no systematic favoring of one mutant residue over another, it is clear that the WT DSTP produces a B-factor at or near the bottom for each of the three loops. This supports the notion that softer loops (with proline removed) can search more quickly.

We will study the relative hydrophobic stabilization of the core domain swapped loop region by two approaches: (i) examination of explicit water exclusion in the core, and (ii) energy minimization in the presence of salvation. If we find significant energy lowering in the latter case, we will attempt to carry out free energy perturbation analysis in all atom MD.

Within the fibril model framework discussed earlier in the report, it is of interest to study the fatal familial insomnia mutation D178N, which requires also methionine in codon 129. We note that for the fibril arrangement N $\uparrow$ C $\uparrow$ C $\downarrow$ N $\downarrow$  that there is potential proximity between residue 178 in one monomer and residue 129 in another. With the asparagine substitution, the formation of a stabilizing hydrogen bond between the



**Fig. 8:** Two-state model to motivate perturbation study of mutations on domain swapped hinge regions of the model prion trimer. Upper panel illustrates the effect of mutation to relatively hydrophobic residues from proline. The wild type three monomer surface is modestly destabilized (the hinge regions are in the solvent exposed random coil) while they may be relatively hydrophobically protected in the DSTP structure. As a result the energy surface ramping reduces the kinetic barrier to oligomerization. The lower panel illustrates the generic effect of softening by removing the proline residue. With the assumption that the librational coordinates of the loop are part of the reaction coordinate, the softening flattens each surface (wild type and infectious oligomer) and thus reduces the kinetic barrier between them.

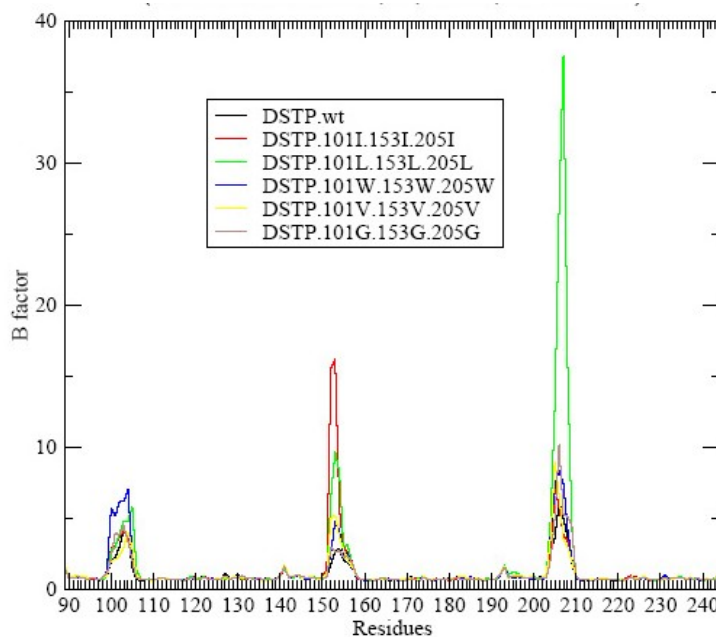


**Figure 9:** B factor of domain swapped prion trimer from 1 ns all atom simulations of mouse prion. The main secondary structures are restrained as the proline bearing loops are allowed to fully fluctuate. In collaboration with S. Yang.

methionine sulfur and the terminal side chain amide of the asparagines is possible, which

is not the case with aspartic acid. The conjecture is that this stabilizing link will hold for an intermediate on the path to conversion with templating via the CLH $\beta$ H of NLH $\square$ H growth. It is interesting to note that such models within our scheme for constructing fibrils will be *less prone* to fibril formation. We will construct such models to examine whether they can account for enhanced conversion kinetics.

**Examining the possible role of the LH $\beta$ H in prion conversion.** We are interested in two models here. First, as shown in the figure below, the novel tri-octarepeat motif first identified by Zahn<sup>15</sup> and illustrated in Fig. (10) has a cross section that matches beautifully to the LH $\beta$ H as illustrated in Fig. (11). Attachment to the beta helix may be facilitated by hydrogen bonds between glutamine side chains. The goal of the modeling will be to see if (a) the tri-octarepeat attachment can indeed occur to any putative LH $\beta$ H structures at the N or C terminus, and if so (b) can this transmit the template information to the N-terminal region. We will study the former with all atom MD using soft restraints for the tri-octarepeat and hard restraints for the different LH $\beta$ H motifs; we will examine bonding for all orientations of the LH $\beta$ H structures and the tri-octarepeat. A second possibility we wish to explore is that the CLH $\beta$ H templates NLH $\beta$ H conversion from either fibrils or proteinase resistant oligomers. In this picture the CLH $\beta$ H anchored structures helps to stabilize less proteinase resistant oligomers.

**Modeling of prion strains with domain swapped oligomers.** We will construct models and explore the possibility that prion strain is encoded in (i) number of monomers in a domain swapped oligomer, (ii) splay of LH $\beta$ Hs in a domain swapped oligomer, and (iii) arrangements of CLH $\beta$ Hs and NLH $\beta$ Hs in fibril repeat units which because of the terminal properties do not promote fibril growth.

We have already tested the stability of a domain swapped dimer of the PrP106 protein in direct analogy to our earlier work on the domain swapped trimer (see Fig. (12) ). As with the trimer there is enhanced overall stability due to entanglement via domain swapping. This suffers, however, from the same nonoptimal threading of the NLH $\beta$ H noted earlier in the proposal. Accordingly, assuming we find the most optimal NLH $\beta$ H threading, we will study other oligomers with different numbers of monomers to assess generic stability of such domain swapped oligomers.

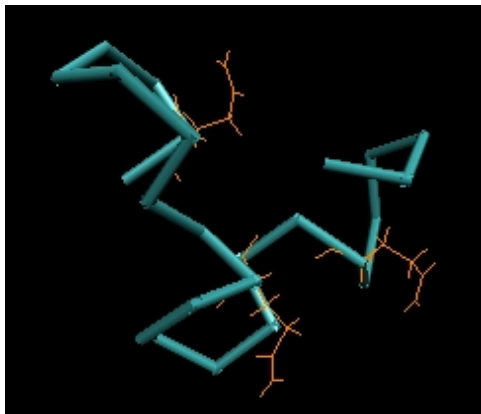


**Figure 10:** Ribbon structure of tri-octarepeat of Ref. (15). Glutamines are highlighted in yellow. Produced by VMD



**Figure 11:** Top view of tri-octarepeat motif laid on CTP3 model from the prion protein. Produced in RASTOP.

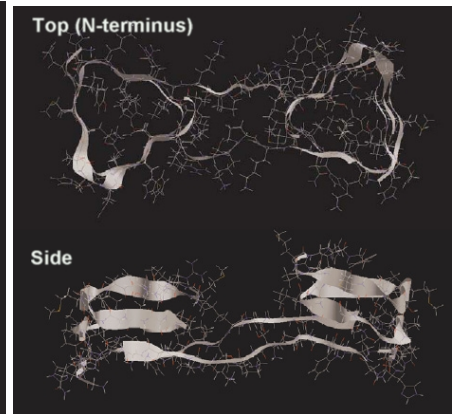


**Figure 12:** Ribbon view of model domain swapped PrP106 dimer (alpha helices not shown). Produced in RASTOP.

Notice in the side view that the individual LH $\beta$ Hs are splayed. This opens the possibility that there are stable or metastable orientations of LH $\beta$ H in oligomers which are splayed relative to the overall oligomer axis, which provides another possible conformation encoding for strains. To study this, we will (i) carry out unbiased long time MD studies of potential oligomer configurations and look for significant residency time in splayed states, and (ii) employ soft restraints together with a systematic sweep of splay angles to hunt for relatively stable starting configurations for unrestrained MD runs.

#### Reportable Outcomes: Awards, Activities, Presentations and Publications

1. **Awards, Activities, and Presentations** (*Appendix A*)
2. **Modelling of Oligomeric Intermediates in prion aggregation.** manuscript published in Biophysical Journal. (*Appendix B*)
3. **Modeling of insertion of Abeta peptides in model membranes.** manuscript published in Biophysical Journal. (*Appendix C*)
4. **Dissertation on modeling of prions and Abeta.** Directions to online copy of dissertation by David Mobley, with strong review chapter. (*Appendix D*)
5. **Proposing a new structure for the minimal infectious unit of prion disease: the Domain Swapped Prion Trimer (DSTP).** manuscript of paper published in FASEB Journal. (*Appendix E*)
6. **Demonstration of the necessity of the membrane in exponential in vivo growth of prion infectivity.** Manuscript published in the Letters section of Biophysical Journal. (*Appendix F*)
7. **Possible mechanism for copper inhibition of prion conversion.** Manuscript published in the Letters section of Biophysical Journal. (*Appendix G*)
8. **Detailed modeling of in vitro yeast prion aggregation** Manuscript of paper published in Phys. Rev. E. (*Appendix H*)

9. Review of amyloidogenic proteins from a materials perspective. Manuscript published in Materials Research Bulletin. (*Appendix I*)
10. Yahoo! News Search Results for Cox Singh "mad cow" (*Appendix J*)

## Conclusions

In summary, through the course of this research we have most significantly (i) produced new and more realistic models for prion membrane associated aggregation kinetics; (ii) modeled insertion of the A-beta peptide into model membranes and noted a possible correlation with inherited forms of Alzheimer's disease (while eyeing possible relevance to insertion of the putative transmembrane segment of the prion protein); (iii) created a new domain swapped prion trimer model which rescues the beta helical trimer model from instability; (iv) shown that the membrane not only mediates toxicity of the prion infectious units but also exponential growth; (v) noted that copper can protect the prion protein against conversion to the infectious form; (vi) demonstrated that a possible C-terminal beta helix structure can potentially explain in vitro fibril structures coupled with N-terminal beta helix formation and novel domain swapping.

## References

---

<sup>1</sup> **Tattum, M.H., S. Cohen-Krausz, A. Khalili-Shirazi, G.S. Jackson, E.V. Orlava, J. Collinge, A.R. Clarke, and H.R. Saibil.** 2006. Elongated oligomers assemble into mammalian PrP amyloid fibrils. *J. Mol. Biol.* **357**: 975-985.

<sup>2</sup> **Govaerts, C., H. Wille, S. B. Prusiner and F. E. Cohen.** 2004. Evidence for assembly of prions with left-handed beta 3-helices into trimers. *Proc. Natl. Acad. Sci. U. S. A.* **101**:8342-8347.

<sup>3</sup> **Yang, S., H. Levine, J. N. Onuchic and D. L. Cox.** 2005. Structure of infectious prions: stabilization by domain swapping. *FASEB J.* **19**:1778-1782.

<sup>4</sup> **Stewart, R.S. and D.A. Harris.** 2005. A transmembrane form of the prion protein is localized in the Golgi apparatus of neurons. *J. Biol. Chem.* **280**: 15855-15864.

<sup>5</sup> **Baskakov, I.V., G. Legname, M.A. Baldwin, S.B. Prusiner, and F.E. Cohen.** 2002. Pathway complexity of prion protein assembly into amyloid. *J. Biol. Chem.* **277**: 21140-21148.

<sup>6</sup> **Safar, J., H. Wille, V. Ittri, D. Groth, H. Serban, M. Torchia, F.E. Cohen, and S.B. Prusiner.** 1998. Eight prion strains have PrPSc molecules with different conformations. *Nat. Med.* **4**: 1157-1165.

<sup>7</sup> **Novitskaya, V., N. Makarava, A. Bellon, O.V. Bocharova, I.B. Bronstein, R.A. Williamson, I.V. Baskakov.** 2006. Probing the conformation of the prion protein within a single amyloid fibril

---

using a novel immunoconformational assay. *J. Biol. Chem.* **281**: 15536-15545.

<sup>8</sup> **Bocharova OV, N. Makarava, L. Breydo, M. Anderson, V.V. Salnikov, and I.V. Baskakov.** 2006. Annealing prion protein amyloid fibrils at high temperature results in extension of a proteinase K-resistant core. *J. Biol. Chem.* **281**:2373-2379.

<sup>9</sup> **Perutz, M. F., J. T. Finch, J. Berriman and A. Lesk.** 2002. Amyloid fibers are water-filled nanotubes. *Proc. Natl. Acad. Sci. U. S. A.* **99**:5591-5595.

<sup>10</sup> **Jenkins, J., O. Mayans and R. Pickersgill.** 1998. Structure and evolution of parallel beta-helix proteins. *J. Struct. Biol.* **122**:236-246.

<sup>11</sup> **Jenkins, J. and R. Pickersgill.** 2001. The architecture of parallel beta-helices and related folds. *Prog. Biophys. Mol. Biol.* **77**:111-175.

<sup>12</sup> **Mobley, D.L. , D.L. Cox, R.R.P. Singh, M.W. Maddox, and M.L. Longo.** 2004. Modeling amyloid beta-peptide insertion into lipid bilayers. *Biophys. J.* **86**: 3585-3597.

<sup>13</sup> **Kong, Q., W.K Surewicz, R.B. Petersen, W. Zou, S.G. Chen, P. Gambetti, P. Parchi, S. Capellari, L. Goldfarb, P. Montagna, E. Lugaresi, P. Piccardo, and B. Ghetti.** 2004. Inherited Prion diseases. Pp. 673-775. in *Prion Biology and Disease.*, ed. S.B. Prusiner (Cold Spring Harbor Press, Cold Spring Harbor, NY),.

<sup>14</sup> **Nazor, K.E., F. Kuhn, T. Seward, M. Green, D. Zwald, M. Purro, J. Schmid, K. Biffinger, A.M. Power, B. Oesch, A.J. Raeber, and G.C. Telling.** 2005. Immunodetection of disease-associated mutant PrP, which accelerates disease in GSS transgenic mice. *EMBO J.* **24**: 2472-2480.

<sup>15</sup> **Zahn, R.** 2003. The octapeptide repeats in mammalian prion protein constitute a pH dependent folding and aggregation site. *J. Mol. Biol.* **334**: 477-488.

## APPENDIX A: ACTIVITIES, HONORS, AND PRESENTATIONS ASSOCIATED WITH THIS RESEARCH AWARD

### *Honors*

D.L. Cox, J.S. Guggenheim Memorial Fellowship, for ``Studies in Theoretical Biological Physics'' (emphasizing prion protein research) during sabbatical leave at the Center for Theoretical Biological Physics of the University of California, San Diego, July 2004-June 2005.

D.L. Mobley, Graduate Fellow, Kavli Institute for Theoretical Physics, Aug.-Dec. 2003.

J. Pan I<sup>2</sup>CAM Junior Fellow (supported collaborative visit with Prof. E. Artacho, Cambridge University, Jan-Feb. 2005)

J. Pan UC Davis Summer Graduate Research Fellow (supports one month of summer research, Summer 2005)

### *Activities*

D.L. Cox, R.R.P. Singh, co-organizers of International Workshop on ``Protein Misaggregation: from Biomolecules to Neurodegenerative Diseases," sponsored by the Institute for Complex Adaptive Matter, Boston, Feb. 2004.

D.L. Cox, R.R.P. Singh, co-organizers of First International ICAM Workshop on **``PROTEIN AGGREGATION AND AMYLOID FORMATION IN SYSTEMIC AND NEURODEGENERATIVE DISEASE: PHYSICAL, MOLECULAR AND BIOLOGICAL APPROACHES,**'' Lausanne, Switzerland, July 16-19 2005. (<http://i2cam.org/i2camyloid>)

### *Invited Presentations*

#### D.L. Cox:

- ``*The Physics of Amyloid Matter*,'' Colloquium, Department of Physics, UC Davis, October 2006.
- ``*ICAM: Studying emergence from quantum matter to the mind*,'' Lecture, Workshop on Emergence, University of Michigan, October 2006
- ``*Physical modeling of prion disease*,'' Seminar, Center for Computational Biology, Washington University, St. Louis, February 2006.
- ``*Molecular level modeling of the prion protein*,'' Biophysics Graduate Group/Center for Biophotonics Seminar, UC Davis, Nov. 2005
- ``*Molecular level modeling of the prion protein*,'' Seminar, Ken Dill Lab, UC San Francisco, October 2005
- ``*Consider a spherical mad cow: a physical look at prions*,'' Sciences Colloquium, Chico State University, Sept. 2005

- ``Physical Modeling of Amyloid Disease,"' Lecture, International I2CAM workshop on PROTEIN AGGREGATION AND AMYLOID FORMATION IN SYSTEMIC AND NEURODEGENERATIVE DISEASE: PHYSICAL, MOLECULAR AND BIOLOGICAL APPROACHES, EPFL Lausanne, Switzerland, July 2005.
- ``Molecular level modeling of the prion protein,"' Brooks group seminar, Scripps Research Institute, June 2005.
- ``Consider a spherical mad cow: a physical look at prions," Condensed matter theory seminar, Department of Physics, The Ohio State University, April 2005.
- ``Consider a spherical mad cow: a physical look at prions," Condensed Matter Journal Club, Department of Physics, UC San Diego, March 2005.
- ``Physical Modeling of Amyloid Diseases," invited lecture, Symposium on Frontiers in Computational Biology, Rice University, December 2004.
- ``Physical Modeling of Amyloid Diseases," seminar, Center for Theoretical Biological Physics, UC San Diego, November 2004.
- *Theoretical Modeling of Prion Disease Incubation Dynamics*, CeresR Forum "Transmissible Spongiform Encephalopathies in Animal and Human Health: The Science and the Policy" sponsored by Virginia Polytechnic Institute, Washington DC, March 2004.

R.R.P. Singh:

- “The mysterious prion protein”, Mathematics Department Seminar, University of California at Davis, November 2004.
- ``Prion Diseases,” Colloquium, Tata Institute for Fundamental Research, Bombay India, July 2004
- “Prion Diseases”, Seminar at Jawaharlal Nehru University, Delhi, India, July 2004.

R.V. Kulkarni:

- *Models of incubation time dynamics in prion diseases*, short talk at Protein Misaggregation: from Biomolecules to Neurodegeneration workshop, Boston, MA, Feb. 9-11, 2004.

D.L. Mobley:

- "Modeling Alzheimer's A-Beta Peptide Insertion into Lipid Bilayers", Vijay Pande group, Stanford University, Dec. 4, 2003
- "Modeling Alzheimer's A-Beta Peptide Insertion into Lipid Bilayers", Theoretical and Computational Molecular Biophysics group, The Scripps Research Institute, San Diego, Dec. 11, 2003
- "Modeling Alzheimer's A-Beta Peptide Insertion into Lipid Bilayers", St. Jude Children's Research Hospital, Jan. 12, 2004.
- "Modeling Alzheimer's A-Beta Peptide Insertion into Lipid Bilayers" and "Simulations of Oligomeric Intermediates in Prion Diseases", Jan. 13, 2004, David Teplow group, Harvard

- "Modeling Alzheimer's A-Beta Peptide Insertion into Lipid Bilayers", Jan. 16, 2004, Center for Theoretical Biological Physics, UC San Diego.
- "Modeling Alzheimer's A-Beta Peptide Insertion into Lipid Bilayers", Feb. 10, 2004, short talk at Protein Misaggregation: from Biomolecules to Neurodegeneration workshop, Boston, MA, Feb. 9-11, 2004.
- "Modeling Alzheimer's A-Beta Peptide Insertion into Lipid Bilayers", Feb. 27, 2004, Biophysics seminar, UC Davis.
- "The Hunt for the Cause of Cell Death in Alzheimer's Disease", March 19, 2004, science colloquium, Shasta College, Redding, CA.
- "Oligomerization and Aggregation in Amyloid Diseases", April 2, 2004, ICAM workshop on "Lifelike Matter", Santa Fe, N.M.

J. Pan:

- ``Theoretical study of metal binding to the cellular prion protein," Seminar, Biophysics Graduate Group, UC Davis, November 2004.

***Contributed Presentations:***

R.R.P. Singh. ``Copper can modulate prion protein conversion'' EMBO International Workshop on Molecular mechanisms of amyloid disease, Florence, Italy, March 2005. (Poster)

D.L. Cox, ``Copper can modulate prion protein conversion'' Gordon Research Conference on Protein Folding, Ventura CA January 2005. (Poster)

D.L. Cox, ``Theoretical investigation of metal binding affinities in the prion protein,'' Keystone Symposium on Transmissible Spongiform Encephalopathies, Snowbird, Utah, January 2005. (Poster)

K. Kunes, *Kinetic and Stochastic Models of 1D yeast ``prions''*, American Physical Society March Meeting, Los Angeles, March 2005.  
[\(http://meetings.aps.org/Meeting/MAR05/Event/21907\)](http://meetings.aps.org/Meeting/MAR05/Event/21907)

J. Pan, *Theoretical study of metal binding in the Prion protein*, American Physical Society March Meeting, Los Angeles, March 2005.  
[\(http://meetings.aps.org/Meeting/MAR05/Event/21906\)](http://meetings.aps.org/Meeting/MAR05/Event/21906)

K. Kunes, *Kinetic and Stochastic Models of 1D yeast ``prions''*, International I2CAM workshop on PROTEIN AGGREGATION AND AMYLOID FORMATION IN SYSTEMIC AND NEURODEGENERATIVE DISEASE: PHYSICAL, MOLECULAR AND BIOLOGICAL APPROACHES, EPFL Lausanne, Switzerland, July 2005. (Poster)

J. Pan, *Theoretical study of metal binding in the Prion protein*, International I2CAM workshop on PROTEIN AGGREGATION AND AMYLOID FORMATION IN

SYSTEMIC AND NEURODEGENERATIVE DISEASE: PHYSICAL, MOLECULAR AND BIOLOGICAL APPROACHES, EPFL Lausanne, Switzerland, July 2005.(Poster)

K. Kunes, *Kinetic Model for 1D aggregation of yeast ``prions''*, American Physical Society March Meeting, Montreal, March 2004.

D.L. Mobley, "Modeling Alzheimer's A-Beta Peptide Insertion into Lipid Bilayers", Feb. 17, 2004, poster at Biophysical Society meeting, Baltimore, MD, Feb. 13-18, 2004.

J. Pan, *Ab initio Study of Transition metal binding to the Prion Protein*, American Physical Society March Meeting, Montreal, March 2004.

## Simulations of Oligomeric Intermediates in Prion Diseases

David L. Mobley, Daniel L. Cox, Rajiv R. P. Singh, Rahul V. Kulkarni, and Alexander Slepoy\*

Department of Physics, University of California at Davis, Davis, California; and \*Sandia National Laboratories, Albuquerque, New Mexico

**ABSTRACT** We extend our previous stochastic cellular automata-based model for two-dimensional (areal) aggregation of prion proteins on neuronal surfaces. The new anisotropic model allows us to simulate both strong  $\beta$ -sheet and weaker attachment bonds between proteins. Constraining binding directions allows us to generate aggregate structures with the hexagonal lattice symmetry found in recently observed *in vitro* experiments. We argue that these constraints on rules may correspond to underlying steric constraints on the aggregation process. We find that monomer-dominated growth of the areal aggregate is too slow to account for some observed doubling-time-to-incubation-time ratios inferred from data, and so consider aggregation dominated by relatively stable but noninfectious oligomeric intermediates. We compare a kinetic theory analysis of oligomeric aggregation to spatially explicit simulations of the process. We find that with suitable rules for misfolding of oligomers, possibly due to water exclusion by the surrounding aggregate, the resulting oligomeric aggregation model maps onto our previous monomer aggregation model. Therefore it can produce some of the same attractive features for the description of prion incubation time data. We propose experiments to test the oligomeric aggregation model.

### INTRODUCTION

Prion diseases are a group of neurodegenerative diseases including bovine spongiform encephalopathy (BSE) in cattle, scrapie in sheep and goats, chronic wasting disease in deer and elk, and kuru and Creutzfeldt-Jakob disease (CJD) in humans. These diseases came to the forefront after BSE reached epidemic proportions in Great Britain in the early 1990s, and it was later shown that transmission of BSE to humans can lead to new variant CJD (vCJD) in humans (Bruce et al., 1997; Hill et al., 1997; Scott et al., 1999).

Prion diseases are unusual in that they appear to be caused by infection with some minimal infectious “seed” of misfolded prion protein, which alone may be able to cause disease by catalyzing further misfolding and, in many cases, aggregation of the prion protein. These aggregates are typically amyloidlike fibrils or amyloid plaques (Caughey, 2000). The infectious agent is unusually hard to eliminate by various methods including ultraviolet irradiation, suggesting it contains no nucleic acid and rather only protein, the so-called “protein-only” hypothesis in prion diseases (Weissmann et al., 2002).

In the case of CJD, a sporadic form of the diseases also exists, occurring more or less randomly worldwide with an incidence of about one in a million people per year. It has been suggested that this incidence is due to the very rare event of nucleating the minimal infectious seed by chance in a healthy individual (Come et al., 1993).

Developing an understanding of these diseases is important because, for one, they are invariably fatal. To

date, no treatment exists. Additionally, it is not yet clear how large the vCJD epidemic in humans will be; an understanding of the disease process is important to be able to guide the search for treatment ideas.

In many cases, prion diseases result in large, up-to-micron-scale plaques in the brains of people and animals with these diseases. They also involve vacuolization or spongiform change in the brain due to death of neurons (Scott et al., 1996). Additionally, the normal form of the prion protein (known as  $\text{PrP}^C$ ) has long been known to misfold and aggregate *in vitro* when catalyzed by the presence of a misfolded prion protein ( $\text{PrP}^{\text{Sc}}$ ) seed (Come et al., 1993). Together, these observations have suggested to some that the aggregation process itself may be important in these diseases (Come et al., 1993; Masel et al., 1999). It has also been suggested that the rate-limiting step in aggregation is nucleation of an appropriate seed, thus the rapid aggregation in the seeded case described above (Come et al., 1993).

Another fact which may be important to this issue is that the prion protein is normally GPI-anchored to the cell surface. Aggregation *in vitro* as mentioned above is observed in solution rather than in the presence of the GPI anchor on a cell surface, leaving the possibility that the aggregation process *in vivo* is different.

Aggregation models developed to explore the aggregation process in prion disease include one-dimensional, fibrillar aggregation-and-fission models (Masel et al., 1999; Slepoy et al., 2001), since aggregates grown *in vitro* are typically seen to be fibrillar. Additionally, our earlier work suggested that an areal aggregation model could explain certain other properties of the diseases (Slepoy et al., 2001). By areal aggregation, we mean two-dimensional aggregation in a relatively regular array, probably on the cell surface due to GPI anchoring, in contrast to the one-dimensional, fibrillar aggregation observed *in vitro*, and also in contrast to

Submitted April 10, 2003, and accepted for publication July 9, 2003.

Address reprint requests to David L. Mobley, Tel.: 530-752-0446; Fax: 530-752-4717; E-mail: mobley@physics.ucdavis.edu.

Rahul V. Kulkarni's present address is NEC Research Labs, 4 Independence Way, Princeton, NJ 08540.

© 2003 by the Biophysical Society

0006-3495/03/10/2213/11 \$2.00

two-dimensional plaques of crossing fibrils which can be observed in vivo. This earlier model is attractive in that it can provide a simple explanation for the long lag phase which is sometimes observed in growth of the amount of infectious material in the brain. This lag phase of little or no growth is followed by a doubling phase with a short characteristic doubling time. Additionally, our earlier model provides a possible explanation of some of the difference between infectious and sporadic forms of CJD (Slepoy et al., 2001). In later work, we used this model to explain and fit experimental dose incubation curves (Kulkarni et al., 2003).

However, there were drawbacks to the earlier aggregation model we proposed. First, no such areal aggregates had so far been observed. Second, the fissioning essential to the model would involve breaking of strong bonds between the proteins, probably bonds between  $\beta$ -sheets (Serag et al., 2002).

More recent experimental work found two-dimensional areal aggregates of prion protein produced during the purification process. These aggregates were examined under electron microscope and found to consist of trimeric or hexameric subunits. These subunits are linked together in a regular array, possibly by their N-terminal sugars or a weak protein-protein interaction (Wille et al., 2002).

This suggested we should modify our earlier model and attempt to reproduce this aggregate morphology. We thought of two basic schemes for growing aggregates of this sort:

1. Growing the aggregate outward, monomer by monomer, from an initial seed, or
2. Oligomeric intermediates (possibly very flexible and of unstable shape), which form on their own in solution and are only catalyzed into stably misfolding in the presence of an existing misfolded seed.

Some evidence in favor of case 2 has already been produced. Monomers of yeast prion can form intermediates if left to stand, which allows aggregation to proceed at an initial faster rate when catalyzed by addition of a seed (Serio et al., 2000). Additionally, the conformation-dependent immunoassay developed by Safar et al. (2002) detects both protease-sensitive and protease-resistant PrP<sup>Sc</sup>. In hamster brains, sensitive PrP<sup>Sc</sup> is observed earlier, followed by resistant PrP<sup>Sc</sup>. This could correspond to case 2 above, where the sensitive PrP<sup>Sc</sup> is the intermediates that are not yet stably misfolded and the resistant PrP<sup>Sc</sup> is stably misfolded intermediates.

Work here has been done to further explore these two potential modifications of our earlier model to examine whether they retain the same features and if additional insight can be gained.

It is important to note that even if areal aggregation is not important to the time course of these diseases, the aggregates observed by Wille and co-workers have already provided insight into the structure of the misfolded prion protein (Wille et al., 2002). Theoretical modeling may be able to place further constraints on the protein or subunit structure

necessary to reproduce these aggregates, and hence provide valuable information because these aggregates *can* form, even if they are not important to the disease progression.

## BASICS OF OUR MODEL

Here we explore the two basic schemes suggested above for growing aggregates like those observed by Wille et al. (2002). To do so, we use a modification of our earlier model. Therefore a recap of common features of these models is useful.

These models are stochastic cellular automata models, meaning that they take place on a lattice with probabilistic interaction and diffusion rules governing the progression of the system. In this case, sites on the lattice are either occupied by individual prion proteins, or water (empty, in the simulation). The protein form at a site can also vary from PrP<sup>C</sup> to PrP<sup>Sc</sup>.

Rules vary depending on the model being explored, but the basic procedure is the same. For every simulation step, which represents a small amount of time, we allow proteins and any aggregates to diffuse a small amount on the lattice (each object has a probability  $1/(\text{size})^{1/2}$  of moving one lattice site in a given step). Then we look at every protein in the lattice and update its state according to the rules. For example, in our original model, the conformation of an individual prion protein is determined solely by its number of neighboring prion proteins, and this can vary from step to step. After doing this, we add more normal prion monomers to replace any that converted to PrP<sup>Sc</sup>. This is due to the assumption that this process would be taking place in a small area on a cell, and the normal prion monomers would be added by the cell or diffuse in from other locations on the cell surface to keep the monomer concentration relatively constant.

## GROWTH VIA MONOMER ADDITION

First, case 1 from above was explored. Simple rules were developed (Fig. 1) which can reproduce aggregates similar to those observed by Wille et al. (2002). It is important to note that although the rules were designed to reproduce such aggregates, most modifications of these rules could not do so. This means that the rules provide some constraints on the protein-protein interactions necessary to reproduce such aggregates. Also, for the purposes of this model, we are assuming the subunits are hexameric, but the corresponding model for trimeric intermediates is actually much simpler than this model and will produce similar results. Details of the algorithm for this model are covered in Fig. 2.

The rules are as follows. The simulation begins with a single hexagonal subunit consisting of six misfolded monomers (*light gray hexagons* in Fig. 1) which stick some of their residues into an adjacent site, excluding anything else from occupying that site (*black*). Healthy monomers (*light gray spheres*) can then attach via a sugar-bond or other

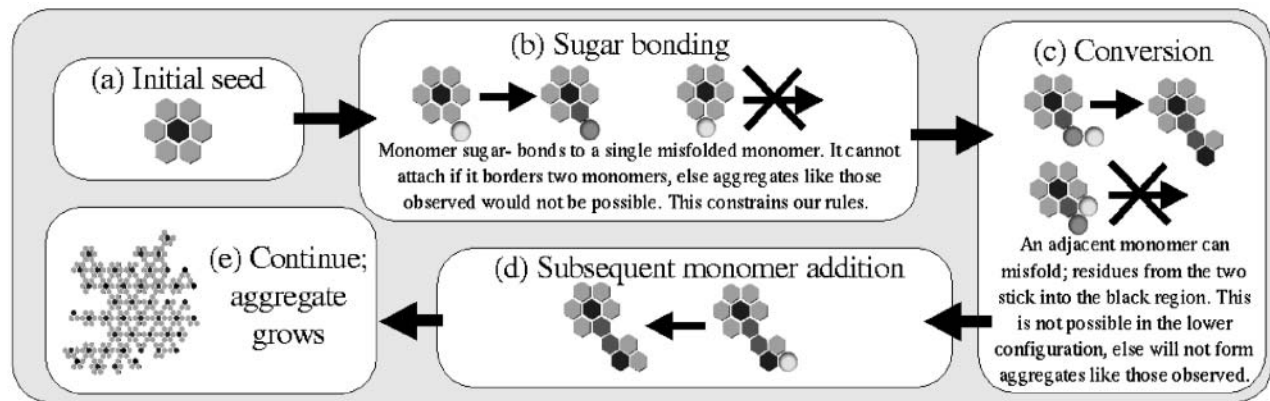


**FIGURE 1** Simple rules for monomer-by-monomer growth of aggregates like those observed. Some possible rules can be excluded, thus these rules give insight into how the proteins involved must be interacting with one another. (a) The initial seed consists of six misfolded monomers (light gray hexagons) surrounding a central region (black) which is occupied by some residues sticking into it from the adjacent six sites. (b) A healthy monomer (light gray sphere) can move adjacent to a misfolded one and attach via a sugar bond or other weak protein-protein interaction (proteins sugar-bonded are colored dark gray). This cannot happen if the monomer moves into the site between two misfolded proteins. (c) Subsequent monomers can move next to the attached one and misfold and begin to form a new hexamer. Residues from the two stick into the black region, preventing anything else from moving there. This cannot happen if the second monomer is adjacent to the existing hexamer; this would produce irregular aggregates unlike those observed by Wille and co-workers (Wille et al., 2002). (d) The forming hexamer can grow and finish via subsequent monomer addition. (e) Continue *a-d* for a long time, and an aggregate like the one shown can form.

weak protein-protein interaction to this subunit (dark gray spheres to dark gray hexagons) but only radially outward from a monomer in the initial hexamer. Additional monomers moving adjacent to the attached monomer can, together with it, misfold but only if the second monomer does not also neighbor the original hexamer. Then additional monomers can attach to this forming hexamer, allowing it to complete. Repeating this process many times can produce mostly regular aggregates with some holes, similar to those observed.

The rules are also probabilistic: above, “can” means that some fraction of the time the event occurs. These probabilities can be changed in the simulation and give different growth rates, but the same essential features and scaling as described below.

If this is in fact how these aggregates are forming, we find out about the orientation of monomers within a hexagonal subunit. We find, as mentioned in the discussion of the rules above, that the N-terminal sugars or attachment sites must stick radially outward from each monomer in a hexagonal subunit (Fig. 1 *b*). This is in agreement with the hexagonal structure proposed by Wille and co-workers (Wille et al., 2002). Additionally, we find that no such regular aggregates can be produced unless the monomer attaching to a previously attached monomer (Fig. 1 *c*) can only attach if it is not adjacent to an existing hexamer. This seems to indicate that the other spaces must be occupied by residues from the existing hexamer, preventing attachment in those sites.

This model can also reproduce gaps in aggregates as observed. In this model gaps are due to variations of the growth rate from average for part of the aggregate, causing several parts of the aggregate to grow apart and then rejoin after leaving a gap.

One reason for developing this model was to see if it would capture the same features of the disease as our original

model. Our original model explained the difference between the lag phase and the doubling phase by suggesting that the doubling phase is initiated when aggregates begin to fission, then regrow to a certain fissioning size and break again. Key to this explanation is our result that aggregation speeds up, so that the time for an aggregate to double in size from half its fission size to its fission size is much less than the time for it to get from its initial size to its fissioning size.

To see if this model could produce the same separation of lag and doubling phases, we examined the aggregate growth rate as a function of size in this model (Fig. 3) and found it speeds up only slowly. Naïvely, one would expect the growth rate to be roughly proportional to the square root of the size, as the growth rate is proportional to the circumference of the aggregate, which, assuming a circular aggregate, is  $2\pi r$ . The size of the aggregate is proportional to the area,  $\pi r^2$ , so the radius is proportional to the square root of the size and thus the rate proportional to the square root of the size. To a good approximation, the growth rate observed here is well-fit by an offset plus a term proportional to  $(size)^{1/2}$ , as expected.

In this simple picture, one can calculate the ratio of the doubling time to the lag time. The lag time is the time to go from the initial size, say size 0 for simplicity, to size  $n$ ; the doubling time from size  $n/2$  to size  $n$ . Integrating the rate to get the times and taking the ratio we find  $t_{\text{doub}}/t_{\text{lag}} = 1 - 1/\sqrt{2}$  or  $\sim 0.293$ . This means that this model cannot produce such a large separation between lag and doubling times as our earlier model could, at least not without further modification.

This also indicates that if there is a lag phase and if the difference between it and the doubling phase is due to acceleration of aggregation, this picture is not sufficient and

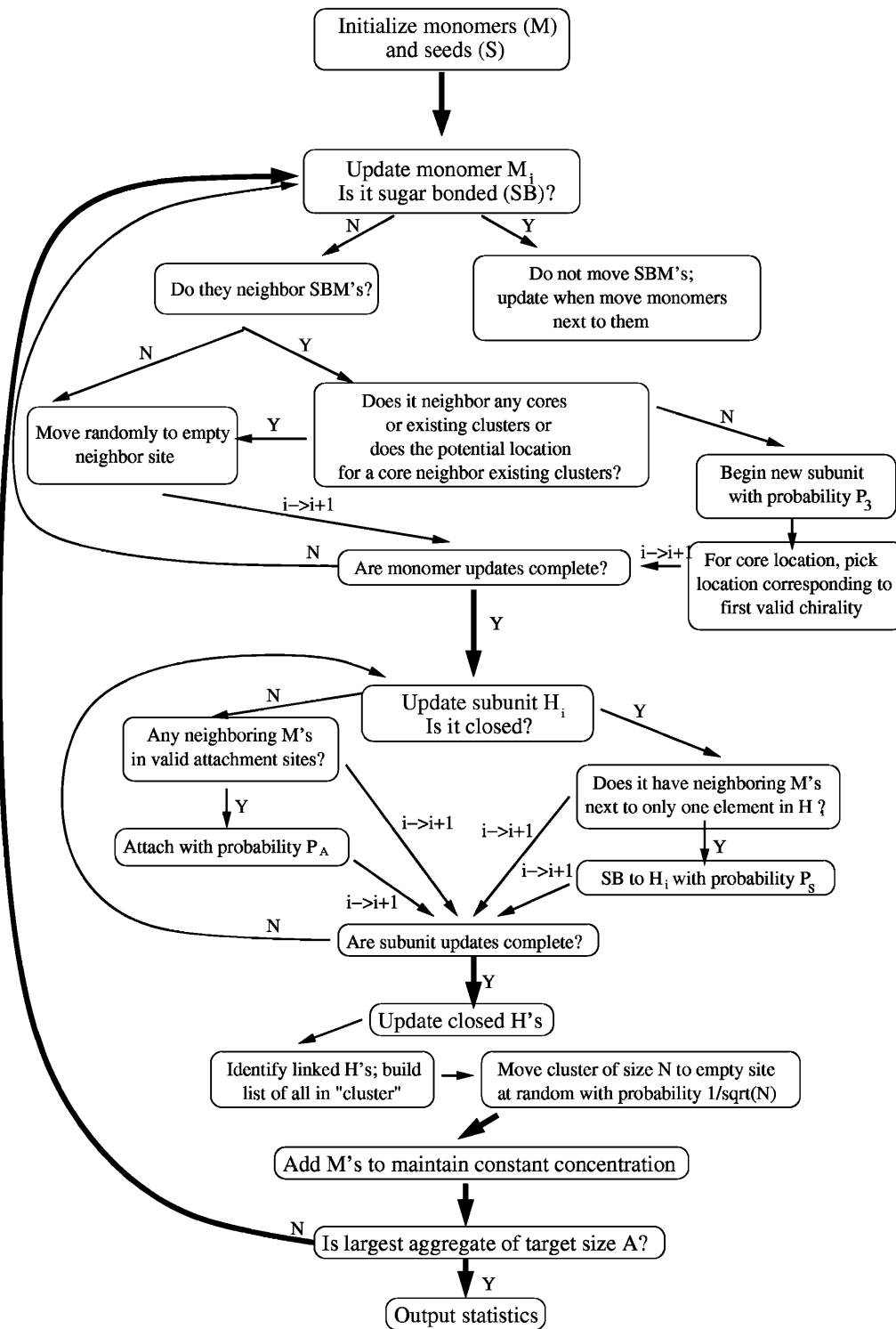


FIGURE 2 Flow chart of simulation for monomer addition model. We typically use  $P_3 = 0.2$ ; we tried a variety of different values for this and values near 0.2 seem to produce the most regular aggregates. We also typically use  $P_S = 0.9$ . This is not important and roughly sets the simulation timescale. Also, for our statistics, we typically average  $>1000$  such runs as the one described here.

something more like case 2, growth from intermediates, may be a better representation of the disease process.

## GROWTH VIA INTERMEDIATES

In this case, aggregation is assumed to be the assembly of independent hexameric intermediates into a larger areal

aggregate. The intermediates themselves are not misfolded but only misfold, in this model, when they either aggregate with an existing misfolded seed, or come together in such a way that they can misfold and form a new stable seed. In this way, the model works essentially just like the model of Slepoy et al. (2001), except now hexameric intermediates are playing the role of monomers (Fig. 4). As

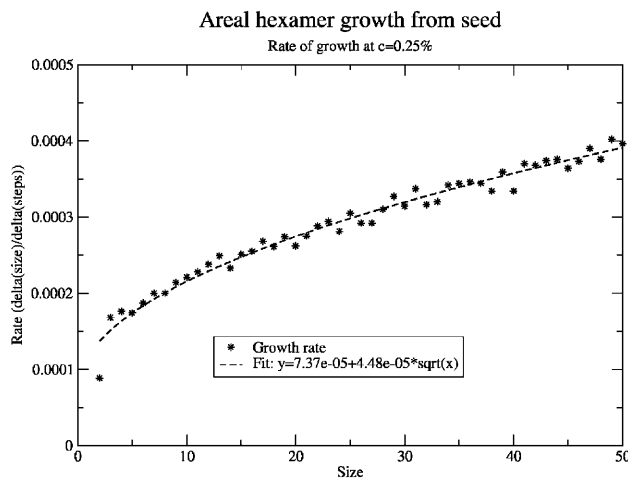


FIGURE 3 Growth rate (change in aggregate size per step) as a function of size for seeded areal aggregation in the monomer growth model. Growth rate goes as the square root of the size with an offset, which was as expected for this model.

mentioned above, there is some evidence that intermediates greatly increase aggregation rate in studies of yeast prions, so this emphasis on the importance of intermediates may be reasonable.

To be able to map this model back into our old model, though, we need to know how the intermediate concentration depends on monomer concentration. And this is not obvious. So a simulation was developed to explore how the concentration of hypothetical hexameric intermediates would depend on monomer concentration. Again, here we are assuming the intermediates are hexameric but we can easily modify the model to accommodate trimers.

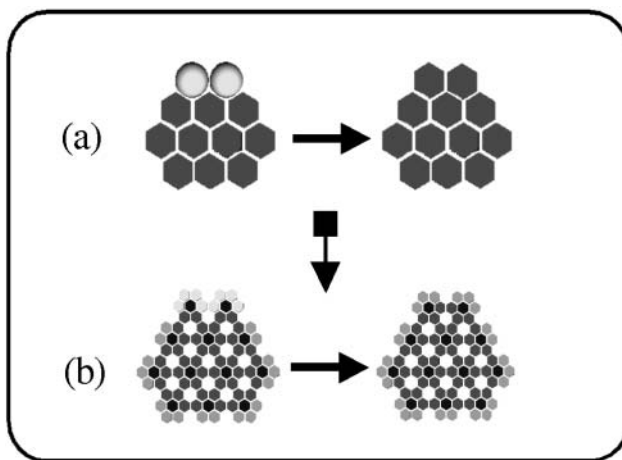


FIGURE 4 (a) As in Slepoy's model (Slepoy et al., 2001), subunits were healthy monomers (light gray spheres) aggregating with misfolded monomers (dark gray hexagons); (b), subunits are hexagonal intermediates (light gray/dark gray) aggregating with misfolded hexagonal structures (medium gray/dark gray). In both cases, the aggregation process and kinetics ought to be, and indeed are, similar.

To get at the concentration of intermediates, it was assumed that two monomers have a probability  $P_1$  of beginning a new hexameric subunit when they come into contact (see Fig. 5). This new subunit can grow by addition of monomers when they move into appropriate positions (changing this probability does not affect the outcome of the simulation, only the timescale, so it was set to 1). However, this growth process competes with a “dissolving” process by which a monomer that is part of an intermediate but only has one neighboring monomer can break off with a probability  $P_3$ . Thus the end destiny of any intermediate that begins is either to form a complete hexameric intermediate, in which case it can persist, or to dissolve completely. Details of the algorithm for this model are shown in Fig. 6.

This dissolving, or reversibility, was included because it was not obvious that at low monomer concentrations, one would expect a reasonable formation rate of intermediates via this mechanism. It was initially thought that at concentrations below something on the order of  $P_3$ , breaking would dominate and the formation rate of intermediates would be almost zero. First, the simulation that was developed was used to examine the dependence of time for intermediate formation as a function of monomer concentration (Fig. 7). It was found that at high monomer concentration, the time to form an intermediate scales between  $1/c$  and  $1/c^2$  ( $c$  is concentration). This is because the likelihood of starting an intermediate scales as the dimer concentration ( $1/c^2$ ), whereas the time to add monomers to it scales as  $1/c$ . On the other hand, at very low monomer concentration, the time asymptotically approaches  $1/c^6$ . This is due to the fact that at these concentrations, dissolving dominates and it is only in the very rare event that six monomers are in the same place at

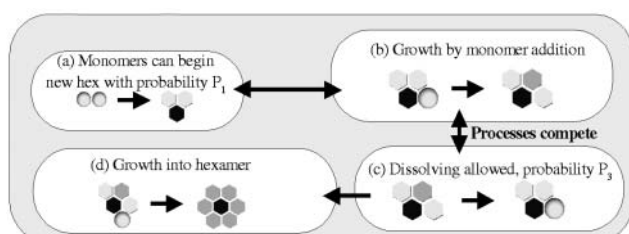


FIGURE 5 Rules for the formation of intermediates. Note that growth and dissolving compete, so that any intermediate eventually either becomes a complete, stable hexagon or dissolves back into monomers. (a) Two monomers have a probability  $P_1$  of joining to begin a new intermediate, which is not yet stably misfolded. Black represents a region blocked by some of their residues. (b) This can grow by addition of monomers to either “end.” After attaching, the monomer sandwiched between the other two has two neighbors and is not allowed to break off, whereas the ones with only one neighbor can. (c) A monomer with only one neighboring monomer has a probability  $P_3$  of breaking off in a given step. This competes with the growth process. (d) Continuing addition of monomers can result in a finished hexameric intermediate where every monomer has two neighbors and is safe from breaking off.

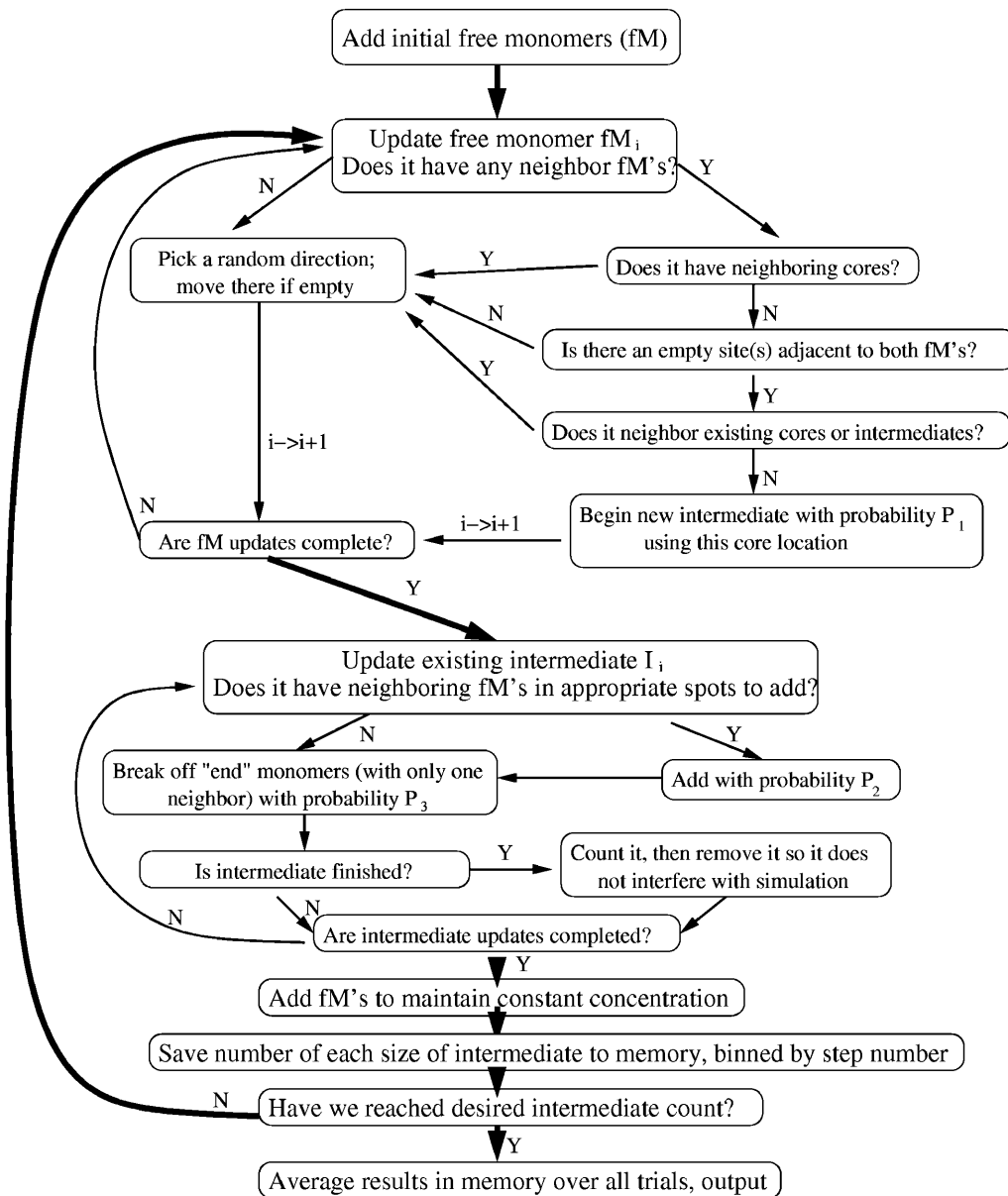


FIGURE 6 Flow chart of simulation for the formation of intermediates. Note that  $P_1$  we vary for different runs,  $P_2$  we typically set to 1 (it sets the simulation timescale and is unimportant), and  $P_3$  we also vary. Finished intermediates are removed so that we can run to a larger number of finished intermediates without the lattice getting clogged. Here, also, we typically average  $>1000$  trials for good statistics.

almost the same time that an intermediate can finish. The probability of that scales as  $1/c^6$ .

It is interesting to note that the beginning of the transition between high concentration behavior, where most intermediates successfully become complete, and low concentration behavior, where only a lucky few do, begins at a concentration on the order of the breaking probability,  $P_3$ . This suggests that if the strength of bonds between intermediates could be weakened somehow, the biological number of intermediates could be drastically decreased by pushing biological monomer concentrations into the  $1/c^6$  regime.

The goal, however, was to determine the dependence of the intermediate concentration on monomer concentration. This just provided a formation rate, and the functional

form was uncertain. So another sort of result was examined, wherein we began examining behavior of the system as a function of time, and measured the number of different partial intermediates (two monomers, ...five monomers, hexameric intermediates). We first examined the case with no breaking ( $P_3 = 0$ ) to check our results, because it is relatively easy to work out kinetics in that case. A sample of one of these plots is shown in Fig. 8, with symbols as data points and solid lines as approximate kinetics fits. It is important to note that in this case, and in the case of nonzero breaking probability, the number of dimers, trimers, tetramers, and pentamers reaches equilibrium relatively quickly and then the hexamer number begins to grow linearly at a rate equal to the rate of dimer formation.

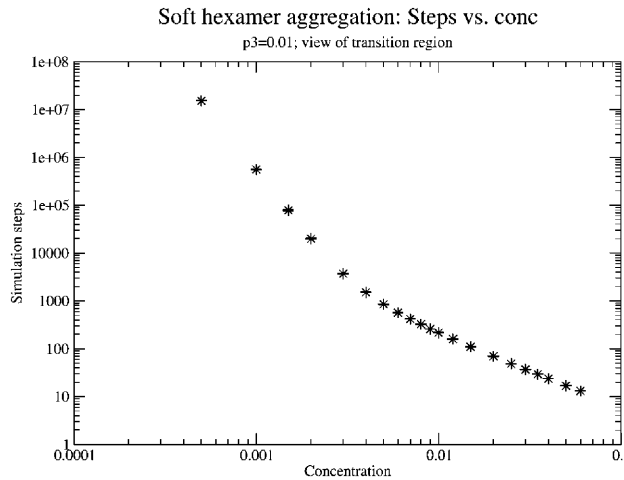


FIGURE 7 Simulation steps (time) to form a hexameric intermediate as a function of monomer concentration. Log-log scale. Note the broad transition to dissolving-dominated behavior at low concentration. The transition actually continues to even lower concentration than can be seen here. At very low concentration the time eventually scales as  $1/c^6$ . Standard deviations fall within the size of the data points on this plot.

Sample results with nonzero breaking are shown in Fig. 9. These results are qualitatively similar, except the number of pre-intermediates that persists is much lower. In the high-breaking limit, the very low level of intermediates demonstrates that either a potential intermediate gets “lucky” and quickly forms an intermediate, or it dissolves back to monomers, leaving few dimers, trimers, and so on.

The kinetics equations we can write down to describe this simulation are relatively simple. With  $r_{nm}$  as the rate constant for forming  $m$ -mers from  $n$ -mers, and  $b_{nm}$  as the rate of breaking  $n$ -mers into  $m$ -mers plus monomers, we can write:

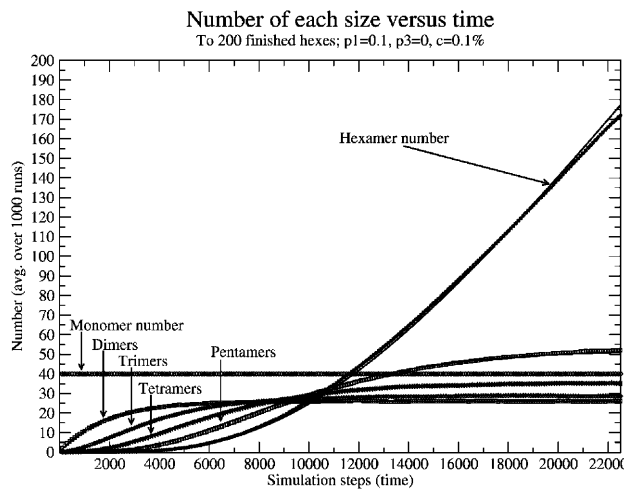


FIGURE 8 Number of each size as a function of time (simulation steps), with zero breaking. Note that, at long times, intermediates reach equilibrium and the hexamer number begins growing linearly with time. Points are simulation data points; solid lines (mostly overlapping points) are approximate kinetics results.

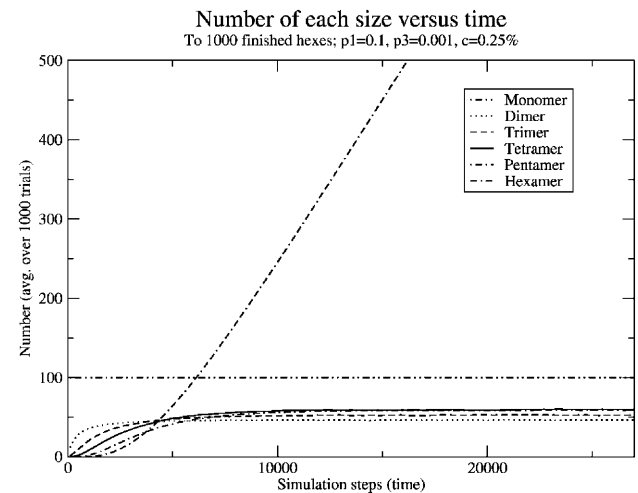


FIGURE 9 Number of each size as a function of time (simulation steps) with nonzero breaking. Compare to Fig. 6; note that the number of intermediates reaches equilibrium faster and at smaller numbers, but that the hexamer number still grows linearly at long times.

$$[c_1] = c \quad (1)$$

$$\frac{d[c_2]}{dt} = r_{12}[c_1]^2 - r_{23}[c_1][c_2] - b_{21}[c_2] + b_{32}[c_3] \quad (2)$$

$$\frac{d[c_3]}{dt} = r_{23}[c_1][c_2] - r_{34}[c_1][c_3] - b_{32}[c_3] + b_{43}[c_4] \quad (3)$$

$$\frac{d[c_4]}{dt} = r_{34}[c_1][c_3] - r_{45}[c_1][c_4] - b_{43}[c_4] + b_{54}[c_5] \quad (4)$$

$$\frac{d[c_5]}{dt} = r_{45}[c_1][c_4] - r_{56}[c_1][c_5] - b_{54}[c_5] \quad (5)$$

$$\frac{d[c_6]}{dt} = r_{56}[c_1][c_5]. \quad (6)$$

Since we know that the hexamer number grows linearly at steady state and all of the other concentrations are unchanging, we can greatly simplify the above kinetics by looking at the steady state only. We can work backward from the steady-state behavior of the hexamers to find the dependence of the steady-state rate of hexamer formation on the different kinetic parameters and ultimately on the monomer concentration.

This straightforward kinetics analysis produces the equilibrium result

$$m = \frac{r_{12}c^2}{1 + \frac{b_{21}}{r_{23}c} \left\{ 1 + \frac{b_{32}}{r_{34}c} \left[ 1 + \frac{b_{43}}{r_{45}c} \left( 1 + \frac{b_{54}}{r_{56}c} \right) \right] \right\}}, \quad (7)$$

where  $m$  is the slope at equilibrium of the hexamer formation rate.

The constants in our simple result for  $m$ , above, can be measured from our simulation. However, our simulation does not necessarily reproduce what these constants would

be in a biological system. So it is difficult to say exactly what the rate of intermediate formation,  $m$ , would be in a real system. However, it is nevertheless useful to know the functional form of its dependence on the monomer concentration.

The result that the hexamer number begins growing linearly eventually is independent of monomer concentration. This is important because it means some hexamers can form given these simple rules even if breaking dominates. Given that result, it seems safe to assume that if hexameric intermediates are stable, some will form in biological systems.

In our model, the hexamer number grows linearly indefinitely, which is obviously unrealistic biologically. The reason for this is that we include no mechanism to remove finished hexamers. Realistically, they would be cleared from the body somehow. They could be endocytosed from the cell surface and degraded via the proteasome mechanism or some other pathway. Additionally, any hexamers being taken up into aggregates would reduce this number. Regardless, realistically the number should stabilize at some fixed value determined by the balance of the clearance rate and the formation rate.

With the result that some hexamers form even at low monomer concentrations (and more would form if they are trimers), a model was developed where now hexameric intermediates occupy a single cell on the lattice (equivalently, these could be trimeric intermediates). This model, described below, largely maintains the same attractive features of the original, showing that if areal aggregation is the explanation for these features, as we suggested, this aggregation could be of hexameric intermediates.

Part of our basis for this model is the observation that the intermediates are not yet stably misfolded since formation of intermediates in studies of yeast prions does not lead to a change in circular dichroism results; it is only when they aggregate with a seed that they stably misfold (Serio et al., 2000). This also is justified by observing that if intermediates were stably misfolded, they could act as seeds on their own, without the necessity of an external seed initiating the infection, and thus there would be no difference between sporadic and infectious CJD. Therefore, for aggregates consisting of misfolded oligomers like those observed by Wille et al. (2002), intermediate misfolding must be catalyzed by existing aggregates or few-hexamer misfolded oligomers. We hypothesize that the mechanism for this is intermediates forming bonds to an existing seed. When solvent is excluded locally around these oligomers and their neighbors include a misfolded oligomer or aggregate, they misfold. The important point is that it is solvent exclusion around an intermediate that can cause it to misfold, making this a very rare sporadic event. But a misfolded seed can help this process by providing a place where intermediates bond, helping the solvent-exclusion process. These rules make this model essentially identical in terms of kinetics to our original

model. Details of the algorithm for this model and mapping are shown in Fig. 10.

However, from our old model we estimated the sporadic form of the disease could have a peak at  $\sim 1000$  years, given a biological concentration of  $10^{-3}\%$ . In our new model we find that it is very difficult to estimate this number as the scaling of the time as a function of monomer concentration is complicated. It was hoped that this model would give a result for the onset of sporadic disease that could be compared with the time for onset of the infectious form to see if the results were consistent with the roughly 1-in- $10^6$  incidence of sporadic CJD that we earlier pointed out. Unfortunately, it is difficult for our model to give a concrete answer at this time as the answer depends too much on the value of the biological monomer concentration. We do find, however, that the power law used previously to scale the sporadic data,  $c^{-3}$ , is a lower bound on the separation. That is, the actual exponent should be larger, meaning that we previously underestimated the separation of timescales. Thus although we cannot say exactly what the separation of timescales here will be, we can say that it will be greater than the two orders of magnitude that we previously estimated.

This work suggests that a model like our earlier one, modified to involve areal aggregation of hexameric or trimeric intermediates, could maintain the same attractive features of our earlier model in explaining certain aspects of the diseases. However, without precise knowledge of the biological monomer concentration and a way to measure relevant rate constants, it is difficult to make numerical predictions from this model.

## DISCUSSION

Our work has shown that both in the case of monomer addition to a seed, and in the case of growth via intermediates, it is possible to produce aggregates like those observed by Wille et al. (2002). This leaves the question of how such aggregates actually grew. If areal aggregation is the cause, or part of the cause, of the difference between lag and doubling times, as suggested by Slepoy et al. (2001), then our work suggests that intermediates are already present *in vivo* before aggregation.

Our work has also shown that a model can be developed which, with suitable parameters, can reproduce areal aggregates like those actually observed while maintaining the same features of our original model.

Whether or not areal aggregation is actually important in these diseases, we can gain insight from this model. If the aggregates observed are growing via monomer addition, we gain some constraints on the structure simply from our rules. On the other hand, if intermediates are important to aggregation, then our results indicate the intermediate concentration can be quite important. At high intermediate concentrations, intermediates form relatively fast. However, at low intermediate concentrations, intermediate formation

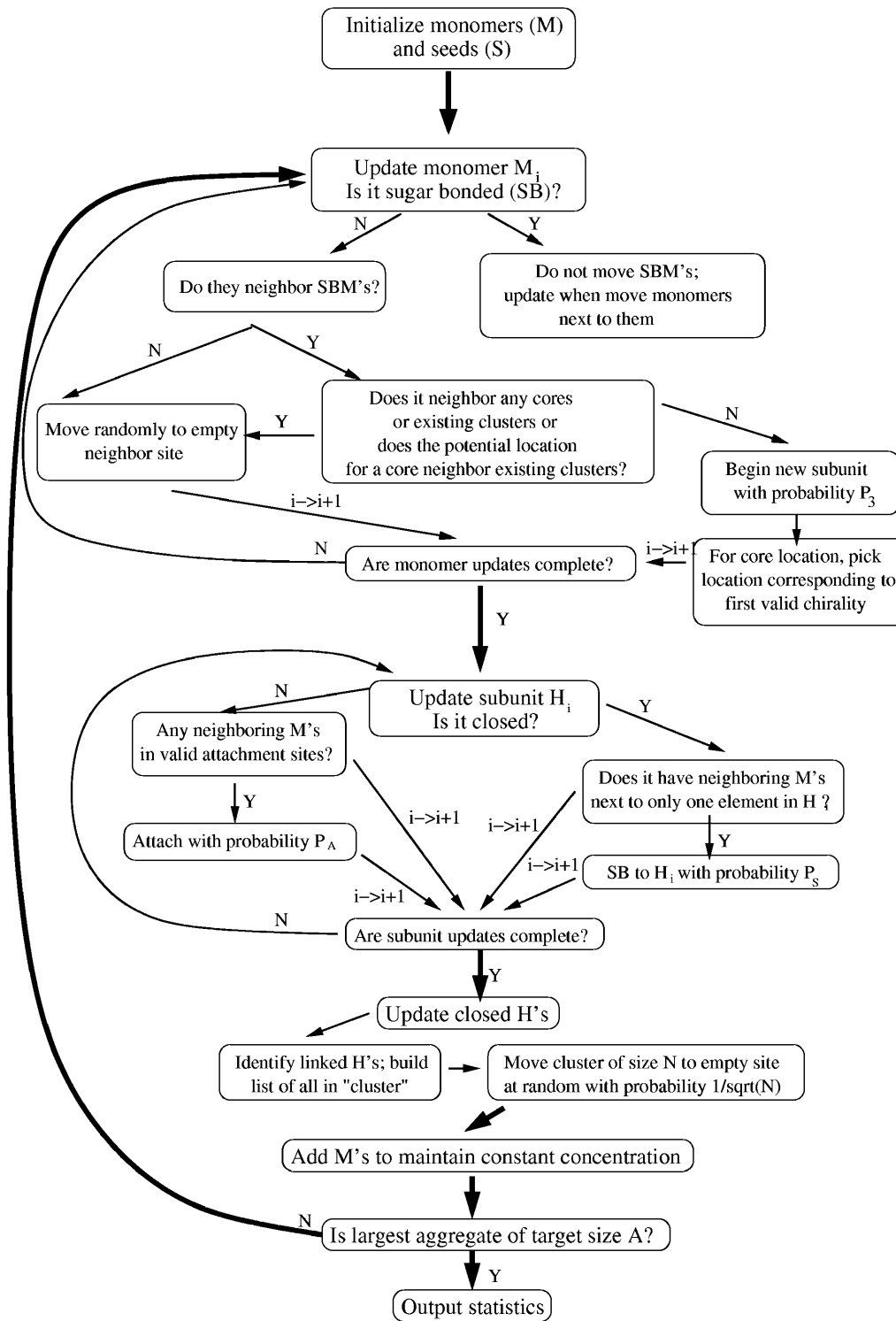


FIGURE 10 Flow chart for simulation mapping back into our original model. Here we basically have free monomers ( $fM$ ), attached monomers that are not yet stably misfolded ( $aM$ ), and monomers that have stably misfolded and aggregated ( $H$ ). We have some choice of a parameter,  $Q_{bc} = m$ . This model will capture the features of our original model for  $m$  between 3 and 6, and the simulation will proceed in exactly the same way. We compute  $N_{bc}$ , the bond coordination number, with  $N_{bc} = n_{fM} + n_{aM} + (m - 1) \times n_H$ , where the  $n$  is the number of neighboring  $fM$ s, and so on.  $N_{hc}$ , the “hardening” or aggregating coordination number, is given by  $N_{hc} = n_{fM} + n_{aM} + n_H$ . We refer to  $Q_{bc}$  as the bonding critical coordination number and  $Q_{hc}$  as the “hardening” critical coordination number.

timescales as  $1/c^6$ . This result is exciting because it suggests the intermediates as a target to prevent aggregation. Simply reducing the monomer concentration by a factor of 2 would decrease the number of intermediates by a factor of  $2^6$  or 64. Within our model, this would certainly increase the aggregation time, and thus slow down the disease, by at least the

same factor. For a disease which can typically incubate for years, this obviously would be a great advantage.

In this case, the location of the transition between low concentration behavior and high concentration behavior is, roughly speaking, set by the probability of monomers breaking off from an intermediate before it becomes a sta-

ble hexamer. Thus if this probability could be increased slightly—that is, the bonds between monomers could be weakened slightly—it would have the result described above. This could provide an explanation for one experimental observation. Humans have a methionine/valine polymorphism at codon 129 of the gene for the prion protein. To date, everyone affected by vCJD has been methionine/methionine homozygous. This effect was also seen in the prion disease Kuru, where the methionine/methionine genotype was associated with increased susceptibility and the shortest incubation time (Goldfarb, 2002). If replacing methionine with valine weakened the monomer-monomer bonds within a forming intermediate and reduced intermediate concentration, this could have exactly the effect described above. This is, however, highly speculative, but as Wille et al. (2002) refine their model of the oligomer structures, it will be interesting to see if this residue falls in the region important to bonding between monomers.

In all, our work shows that our earlier model can be extended to produce aggregates like those observed *in vitro* while still maintaining its attractive features. Our work also suggests possible mechanisms for formation of these aggregates. If the aggregates form by monomer addition, it constrains protein structure. If they form by addition of intermediates, it highlights the importance of bonds within the intermediates as a target for possible treatment strategies. Our model suggests that an experiment to measure the biological intermediate concentration, if there is such a concentration, would be very useful. That would indicate whether such intermediates are present at a high enough concentration to be important biologically. Additionally, this work suggests that experimentalists should check and see whether reasonably-sized aggregates of prion protein can be found *in vivo* on the cell surface. This confinement to the cell surface conceivably could make the difference between the one-dimensional fibrillar aggregates typically observed *in vitro* and two-dimensional areal aggregates like those suggested by the model of Slepoy et al. (2001). Direct measurements, or detailed simulations, giving the strengths of  $\beta$ -bonds between monomers compared to bonds between subunits would be very useful.

One simple way to experimentally discern between growth via monomers or intermediates may be to look at high resolution at the boundary of actual areal aggregates. If growth is by monomers, aggregates will form with monomer-scale roughness at their boundaries (Fig. 1 *e*) while if growth is by intermediates, there will be no such roughness (Fig. 4 *b*). Experimentally, the absence of such roughness would not prove the growth via intermediate hypothesis because incomplete oligomers at the edge of the aggregate could be removed in the purification process, possibly by proteinase K digestion. However, the presence of such roughness would certainly suggest that monomer growth is important.

A more general scheme for experimentally testing the possible role of intermediates and estimating their concentration is via spin labeling (Hubbell et al., 1998; Columbus and Hubbell, 2002). Briefly, a small molecule with a free spin can preferentially react and attach to cysteine residues in proteins. Frequently, these residues are moved around a protein via mutagenesis to then map out structures, but for these purposes a less refined approach is required. Since the PrP protein already possesses cysteine residues at the position of the disulfide bond, the spin labels can attach there (and will not disrupt the disulfide bond). Then the spin-spin interactions will produce a different characteristic spectrum for monomers, incomplete intermediates, and complete intermediates, in particular, with a progressive broadening upon moving from monomers to complete intermediates. Since the spins can have interactions with other spins within a 3-nm sphere, we do not doubt that the broadening will be observable. Of course, since the spin labels will react with *any* cysteines present, it is important to carry this out first by *in vitro* aggregation experiments with purified prion extracts. This will help to identify the conditions which can lead to areal aggregation as observed by Wille et al. (2000), and serve as an existence proof at least for significant oligomeric intermediate concentrations.

We gratefully acknowledge fruitful discussions on spin labeling with John Voss, and on areal prion aggregates with Holger Wille. R.R.P.S. and D.L.C. have benefited from discussions at workshops of the Institute for Complex Adaptive Matter. Sandia is a multiprogram laboratory operated by Sandia Corporation, a Lockheed Martin Company, for the United States Department of Energy's National Nuclear Security Administration under contract DE-AC04-94AL85000.

This research is supported in part by the Nanophases in the Environment, Agriculture and Technology Integrative Graduate Education, Research and Training program sponsored by the National Science Foundation (IGERT grant DGE-9972741), and by the U.S. Army (Congressionally Directed Medical Research Fund, grant NP020132).

## REFERENCES

- Bruce, M. E., W. G. Will, J. W. Ironside, I. McConnell, D. Drummond, A. Suttie, L. McCardle, A. Chree, J. Hope, C. Birkett, S. Cousens, H. Frasier, and C. J. Bostock. 1997. Transmissions to mice indicate that "new variant" CJD is caused by the BSE agent. *Nature*. 389:498–501.
- Caughey, B. 2000. Prion protein interconversions. *Philos. Trans. R. Soc. Lond. B Biol. Sci.* 356:197–202.
- Columbus, L., and W. L. Hubbell. 2002. A new spin on protein dynamics. *Trends Biochem. Sci.* 27:288–295.
- Come, J. H., P. E. Fraser, and P. T. Lansbury, Jr. 1993. A kinetic model for amyloid formation in the prion diseases: importance of seeding. *Proc. Natl. Acad. Sci. USA*. 90:5959–5963.
- Goldfarb, L. G. 2002. Kuru: The old epidemic in a new mirror. *Microbes Infect.* 4:875–882.
- Hubbell, W. L., A. Gross, R. Langen, and M. A. Lietzow. 1998. Recent advances in site-directed spin labelling of proteins. *Curr. Opin. Struct. Biol.* 8:649–656.

Hill, A. F., M. Desbruslais, S. Joiner, K. C. L. Sidle, I. Gowland, J. Collinge, L. J. Doey, and P. Lantos. 1997. The same prion strain causes vCJD and BSE. *Nature*. 389:448–450.

Kulkarni, R., A. Slepoy, R. R. P. Singh, and F. Pázmándi. 2003. Theoretical modeling of prion disease incubation. *Biophys. J.* 85:707–718.

Masel, J., V. A. A. Jansen, and M. A. Nowak. 1999. Quantifying the kinetic parameters of prion replication. *Biophys. Chem.* 77:139–152.

Safar, J. G., M. Scott, J. Monaghan, C. Deering, S. Didorenko, J. Vergara, H. Ball, G. Legname, E. Leclerc, L. Solforosi, H. Serban, D. Groth, D. R. Burton, S. B. Prusiner, and R. A. Williamson. 2002. Measuring prions causing bovine spongiform encephalopathy or chronic wasting disease by immunoassays and transgenic mice. *Nature Biotech.* 20:1147–1150.

Scott, M. R. D., G. C. Telling, and S. B. Prusiner. 1996. Transgenetics and gene targeting in studies of prion diseases. In *Prions Prions Prions*. S. B. Prusiner, editor. Springer-Verlag, Berlin, Heidelberg, pp. 95–123.

Scott, M. R., R. Will, H.-O. B. Nguyen, P. Tremblay, S. DeArmond, and S. B. Prusiner. 1999. Compelling transgenic evidence for transmission of bovine spongiform encephalopathy prions to humans. *Proc. Natl. Acad. Sci. USA*. 96:15137–15142.

Serag, A. A., C. Altenbach, M. Gingery, W. L. Hubbell, and T. O. Yeates. 2002. Arrangement of subunits and ordering of  $\beta$ -strands in an amyloid sheet. *Nat. Struct. Biol.* 9:734–739.

Serio, T. R., A. G. Cashikar, A. S. Kowal, G. J. Sawicki, J. J. Moslehi, L. Serpell, M. F. Arnsdorf, and S. I. Lindquist. 2000. Nucleated conformational conversion and the replication of conformational information by a prion determinant. *Science*. 289:1317–1321.

Slepoy, A., R. R. P. Singh, F. Pázmándi, R. V. Kulkarni, and D. L. Cox. 2001. Statistical mechanics of prion diseases. *Phys. Rev. Lett.* 87: 581011–581014.

Wille, H., M. D. Michelitsch, V. Guenebaut, S. Supattapone, A. Serban, F. E. Cohen, D. A. Agard, and S. B. Prusiner. 2002. Structural studies of the scrapie prion protein by electron crystallography. *Proc. Natl. Acad. Sci. USA*. 99:3563–3568.

Weissmann, C., M. Enari, P.-C. Klohn, D. Rossi, and E. Flechsig. 2002. Transmission of prions. *J. Infect. Dis.* 186:S157–S165. (Suppl.)

# Modeling Amyloid $\beta$ -Peptide Insertion into Lipid Bilayers

David L. Mobley,\* Daniel L. Cox,\* Rajiv R. P. Singh,\* Michael W. Maddox,† and Marjorie L. Longo†

\*Department of Physics, and †Department of Chemical Engineering and Materials Science, University of California, Davis, California

**ABSTRACT** Inspired by recent suggestions that the Alzheimer's amyloid  $\beta$  peptide ( $A\beta$ ) can insert into cell membranes and form harmful ion channels, we model insertion of the 40- and 42-residue forms of the peptide into cell membranes using a Monte Carlo code which is specific at the amino acid level. We examine insertion of the regular  $A\beta$  peptide as well as mutants causing familial Alzheimer's disease, and find that all but one of the mutants change the insertion behavior by causing the peptide to spend more simulation steps in only one leaflet of the bilayer. We also find that  $A\beta$ 42, because of the extra hydrophobic residues relative to  $A\beta$ 40, is more likely to adopt this conformation than  $A\beta$ 40 in both wild-type and mutant forms. We argue qualitatively why these effects happen. Here, we present our results and develop the hypothesis that this partial insertion increases the probability of harmful channel formation. This hypothesis can partly explain why these mutations are neurotoxic simply due to peptide insertion behavior. We further apply this model to various artificial  $A\beta$  mutants which have been examined experimentally, and offer testable experimental predictions contrasting the roles of aggregation and insertion with regard to toxicity of  $A\beta$  mutants. These can be used through further experiments to test our hypothesis.

## INTRODUCTION

Scientific and public interest in Alzheimer's disease has surged in the last several decades. The reason for this is simple: with increasing life expectancy, Alzheimer's disease has emerged as the most prevalent form of late-life mental failure in humans (Selkoe, 2001).

Alzheimer's disease (AD) is a neurodegenerative disease involving progressive memory impairment, altered behavior, decline in language function, disordered cognitive function, eventual decline in motor function, and, finally, death (Selkoe, 2001). In AD, the brain is typically marked by lesions (Selkoe, 2001), neuronal damage, and vascular damage (Durell et al., 1994). These lesions are typically associated with extracellular plaques, called amyloid plaques, and intraneuronal fibrillar tangles (Durell et al., 1994; Selkoe, 2001). The tangles are composed of a protein called *Tau* and are called Tau tangles, whereas the extracellular plaques are largely composed of amyloid  $\beta$  peptide ( $A\beta$ ) in 40- and 42-residue forms (Selkoe, 2001) (denoted  $A\beta$ 40 and  $A\beta$ 42, respectively). These insoluble amyloid plaques composed of  $A\beta$  are considered a hallmark of AD. However, they are not specific to AD (Dickson and Vickers, 2001) and have been observed in older patients free from AD symptoms (Jarrett et al., 1993). It has been pointed out that correlations between amyloid plaque density and severity of dementia are weak, whereas there are stronger correlations between soluble  $A\beta$  levels and severity of dementia (Walsh et al., 2002). This is one reason for the suggestion that oligomers of  $A\beta$  may be more important to toxicity than large insoluble aggregates or plaques. Evidence for this idea has been

provided *in vivo* (Walsh et al., 2002) and *in vitro* (Hartley et al., 1999; Lambert et al., 1998).

One mechanism by which oligomers can damage cells is formation of pores or ion channels through the cell membrane. Early work in this area showed that  $A\beta$  can insert into planar lipid bilayers and allow a calcium current upon insertion, and further that these channels can be blocked (Arispe et al., 1993), suggesting that the calcium current is really due to channel formation, not just bilayer permeabilization by the peptide. Theoretical modeling based on predicted secondary structures for membrane-bound  $A\beta$  has suggested that the  $A\beta$  peptide can form channels with four or six  $A\beta$  subunits in each leaflet of the bilayer (for a total of 8 or 12 per channel; Durell et al., 1994). More recent work has been done using atomic force microscopy to look at the structure of  $A\beta$  inserted in planar lipid bilayers and has found what appear to be channels consisting of four or six visible subunits around a central pore, consistent with the theoretical picture described above. The monomers oligomerize after insertion into the bilayer. Furthermore, in the presence of these oligomers, current can flow (Lin et al., 2001). Lin et al. (2001) also show that, under similar conditions,  $A\beta$ 42 induces neuritic degeneration and death in cell culture and that this toxicity is calcium-dependent and blocked by zinc. Imaging work by another group has also shown that  $A\beta$ 40 oligomers with the E22G mutation (where glutamate, *E*, at residue 22 is replaced with glycine, *G*), which causes a form of familial AD, can form pore-like structures (Lashuel et al., 2002). These pore-like structures actually could be intermediates which, when not membrane-bound, build up into the amyloid plaques observed in the brain of AD patients (Lashuel et al., 2002).

Based on these suggestions, and the observation of Lin et al. (2001) that oligomers in the membrane form after insertion of monomers, we model insertion of the  $A\beta$  peptide

Submitted July 30, 2003, and accepted for publication March 5, 2004.

Address reprint requests to David Lowell Mobley, Physics Department, University of California at Davis, One Shields Avenue, Davis, CA 95616. Tel.: 530-752-0446; E-mail: mobley@physics.ucdavis.edu; web: <http://asaph.ucdavis.edu/~dmobley>.

© 2004 by the Biophysical Society

0006-3495/04/06/3585/13 \$2.00

doi: 10.1529/biophysj.103.032342

into the cell membrane. We first examine the regular  $\text{A}\beta 40$  and  $\text{A}\beta 42$  peptides, then the 40- and 42-residue versions of all of the mutations in the  $\text{A}\beta$  peptide that are known to cause familial AD (FAD) and reduce the average age of onset for the disease compared to people with sporadic AD (Selkoe, 2001). We believe FAD mutants provide a tool for assessing proposed toxicity mechanisms, in that the biological toxicity mechanism should explain why these mutants cause FAD. Our reasoning in looking at these mutants is that if the insertion behavior of the FAD mutant peptides is different, this could make a difference in the prevalence of oligomers in the membrane and thus have an effect on toxicity, if membrane-associated oligomers are indeed important for toxicity *in vivo*. Although some earlier modeling work has dealt with the structure of  $\text{A}\beta 40$  in a lipid bilayer (Pellegrini-Calace et al., 2003), we believe this work is the first to compare insertion of FAD mutants.

This system is modeled using a Monte Carlo (MC) code which has been developed to study insertion behavior of peptides into lipid bilayers. This model, which is specific at the amino acid level, allows us to simulate larger peptides and longer timescales than traditional molecular dynamics simulation studies. The configurational steps are sufficiently small that it has been used successfully to suggest insertion mechanisms, as well as to describe insertion conformations for some peptides (Maddox and Longo, 2002a,b). Here, we find that in all cases the peptide inserts relatively easily. However, we find differences in the conformations the peptide adopts once inserted. These differences in the prevalence of conformations are our central result. Relative to the normal  $\text{A}\beta$  peptide, most of the FAD mutant peptides are more likely to insert only partially in the bilayer. We point out similarities between this partially inserted conformation and the predicted channel structures (Durell et al., 1994). Thus we suggest that FAD mutants may, in this way, facilitate formation of harmful channels. Moreover, the  $\text{A}\beta 42$  peptide, with additional hydrophobic residues, has a greater tendency than  $\text{A}\beta 40$  to hang up in this conformation, and this may correlate with the increased toxicity of  $\text{A}\beta 42$ .

## INTRODUCTION TO THE MODEL AND METHOD

### Model energy function

The Monte Carlo model used here has been described in detail in an earlier publication in this journal (Maddox and Longo, 2002a). Accordingly, we give a brief overview of the essentials here and direct the interested reader to the earlier reference for greater detail.

The model follows previous work from the past decade, most notably and closely that of Milik and Skolnick (1992, 1993) and Baumgaertner (1996). Each amino acid residue is treated as a sphere of identical 1.5 Å radius. There are three contributions to the potential energy function which are residue-independent: 1),  $U_s$ , which is a hard-core steric interaction preventing residue-residue overlap; 2),  $U_T$ , an energy measuring the cost of rotating the peptide planes of successive residues, which is periodic in the torsional angle  $\phi$  between successive residues and has a shallow minimum at  $\phi =$

52.1°; and 3),  $U_A$ , characterizing the energy of distortion of the angle  $\theta$  between adjacent bonds, with a shallow minimum at  $\theta = 89.5^\circ$ .

The lipid bilayer with surrounding water is modeled as a medium without molecular specificity, but with three different spatial regions. The bilayer's normal is taken to lie along the  $z$  axis, so these regions are invariant in the  $x$ - $y$  plane. The bilayer has overall thickness  $2(z_0 + z_h)$ , where  $z_0$  is the length of the acyl chains of a given leaflet, and  $z_h$  is the width of the headgroup region. We have used  $z_h = 4.5$  Å and  $z_0 = 13.5$  Å. We have also tried different chain lengths  $z_0$  but we do not present the results here as they were not significantly different except for reductions in the amount of the transbilayer conformation of the inserted peptide when the membrane is sufficiently thick, as we discuss in Results.

The water-lipid medium is characterized by three dimensionless functions, two of which couple linearly to residue specific parameters we discuss in the next paragraph. These functions are (as shown in Fig. 1):

1.  $w(z)$ , which measures the fractional water content; this is modeled as a step function with exponentially rounded edges (decay length of 2 Å) that is zero in the hydrophobic acyl chains, one in the water region, and varies smoothly through the head region.
2. A polarity function  $p(z)$ , also exponentially rounded with the same decay length, and chosen to be one in the lipid head regions and water while falling to some small value  $1-f_q$  (where  $f_q$ , the polarity factor, determines the polarity of the tail region, with larger  $f_q$  corresponding to a less polar tail region) after approximately one residue diameter into the tail region.
3. A hydrophobicity function  $y(z)$ , which is the sum of two exponentially rounded step functions: one which is zero in the water region and saturates in the head region, proportional to the total gain of hydrophobic energy in the head region, and a second which saturates in the tail region after approximately one residue diameter and accounts for the hydrophobic energy gained for residues penetrating the acyl tail region. The water content  $w(z)$  couples linearly to the external hydrogen bonding energy of each residue, which is residue independent in form. The net hydrogen bonding energy is taken as  $U_H$  given by a sum over residues  $i$  as

$$U_H = \sum_i (w(z_i)H_0 + (1 - w(z_i))H_{int}(i)), \quad (1)$$

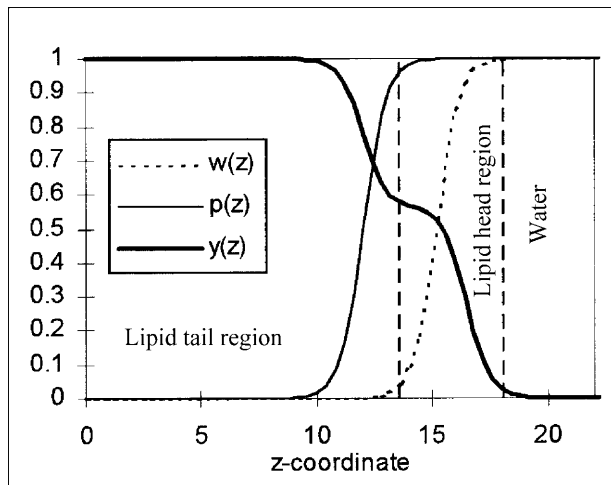


FIGURE 1 Functions characterizing bilayer properties. The lipid bilayer is described by three functions,  $w(z)$  for the fractional water content,  $p(z)$  for the polarity, and  $y(z)$  for the hydrophobicity. Here the  $z$  axis is perpendicular to the plane of the bilayer, and the functions (and the bilayer) are symmetric at  $\sim z = 0$ .

where  $H_0 = -6.12$  kcal/mol is the transfer energy of an unbonded peptide group to water and  $H_{\text{int}}(i)$  the internal hydrogen bonding energy associated with  $\alpha$ -helix formation given by

$$H_{\text{int}}(i) = \frac{H_0}{4} \sum_{n=-4,-3,3,4} V_{\text{H}}(|\vec{r}_{n+i} - \vec{r}_i|). \quad (2)$$

$V_{\text{H}}$  is a nearly hard-core function of the separation between residue  $i$  and the potential helical hydrogen bonding partners along the peptide chain, as proposed by Milik and Skolnick (1993).

Residue specificity is included in two energies associated with polarity and hydrophobicity. First, a potential energy term  $U_Q = \sum_i q_0(i)p(z_i)$  is included, where  $q_0(i)$  is the residue-specific polar energy associated with charged or partially charged functional groups. Second, a hydrophobic energy  $U_B = \sum_i B(i)$  is included, where

$$B(i) = y(z_i)b_0(i) + (1 - y(z_i))\frac{b_1(i)}{4} \times \sum_{n=-4,-3,3,4} V_{\text{H}}(|\vec{r}_{n+i} - \vec{r}_i|). \quad (3)$$

Here,  $b_0(i)$  is residue-specific and measures the water-to-alkane Gibbs hydrophobic transfer energy for residue  $i$ , and  $b_1(i)$  is the maximum reduction in hydrophobic energy due to helical folding. The value  $b_0(i)$  is taken to be proportional to the stochastic accessible area of the residue. The helical-folding related term derives from the loss of accessible surface area associated with helix formation. Values for  $q_0(i)$ ,  $b_0(i)$ , and  $b_1(i)$  for all residues are tabulated in the previous work (Maddox and Longo, 2002a). Note that because the model treats the lipids and water only as media, the hydrophobic energy must be included explicitly in our model energy function.

Because of the way the hydrophobic and hydrogen bonding energies are calculated—simply based on local helicity—the simulation is biased toward  $\alpha$ -helices, as  $\beta$ -structure involves longer range interactions and is not taken into account by the model. Therefore, the model will not accurately describe insertion behavior of any peptide that inserts while in a conformation rich in  $\beta$ -structure. Fortunately, the monomeric A $\beta$  peptide is predicted, based on secondary structure, to be  $\alpha$ -helical between residues 15 and 40 or 42 (Durell et al., 1994; Pellegrini-Calace et al., 2003) when membrane-bound. Experimental NMR work in aqueous sodium dodecyl sulfate micelles, which to some extent resemble a water-membrane medium, confirms this for A $\beta$ 40 (Coles et al., 1998). Thus the model's bias away from  $\beta$ -structure should not play a significant role here. Indeed, we find that the region mentioned above inserts into the membrane in a largely helical structure, as described below.

Our total energy is then taken as the sum  $U = U_S + U_T + U_A + U_B + U_Q + U_H$ . All of our modeling presented below is done at pH 7.0 with temperature 305 K, and uses a polarity factor  $f_q = 0.85$ , corresponding to a polarity between that of octanol and hexadecane. The choice of this value is based on experimental studies (Griffith et al., 1974; Roseman, 1988) and earlier simulation work (Maddox and Longo, 2002a).

## Monte Carlo simulation details

The simulation method is the canonical MC method. We use periodic boundary conditions in all three directions, and in the case where the peptide runs across the boundary, interactions are calculated using the minimum separation between the two residues in question (the minimum image convention). New peptide conformations are generated using three different sorts of moves:

1. Peptide translation: The whole peptide is randomly translated a small distance (between 0 and 0.2 Å) along each Cartesian axis.
2. Spike move (two sorts): (a) For an end residue, the virtual bond connecting it to the chain is rotated slightly, first in the  $x$ - $y$  plane, and then in the  $y$ - $z$  plane. The angle of rotation is random, between 0° and 20°. (b) For a central residue, the residue is rotated a random (between 0° and 20°) amount around an axis joining the centers of its nearest neighbors, while keeping all virtual bond lengths fixed.
3. Slide move: A random virtual bond is selected and all residues on one side (selected randomly, either up or down the chain) of it are moved a small, random amount (between 0 and 0.2 Å), while remaining fixed relative to one another. The move leaves the initial virtual bond the same length but rotated relative to the residues it connects.

One MC step consists of one modification of each type 1, 2, and 3, where the choice of residue is random for moves 2 and 3. Modifications are accepted or rejected with a probability given by the usual Boltzmann factor  $p = e^{-\frac{\Delta U}{kT}}$  so that favorable moves, with a negative  $\Delta U$ , are always accepted, and some unfavorable moves are accepted.

In our work, we wanted to capture insertion behavior without biasing results by initial peptide conformations. We have done two groups of simulations to accomplish this. First, we have started the peptide outside the bilayer in the aqueous phase in a random conformation. Second, we have started the peptide in an initially helical, fully inserted conformation.

MC simulations can be used to investigate nonequilibrium properties (e.g., insertion mechanisms) or equilibrium properties (e.g., inserted conformations) of a system. When these simulations are used to study equilibrium properties, it is important to ensure that the system has fully equilibrated before data collection begins. If this is not done carefully, one consequence is that the so-called equilibrium state might depend on the initial conditions. To establish an appropriate period of equilibration, we monitored the average energy of the peptide as a function of simulation steps. As the peptide equilibrates (reaching its energetically preferred conformation(s)), the average energy decreases from an initially higher value. Thus we can get a reasonable idea how many simulation steps it takes for this to happen simply by plotting energy versus step number.

Using this method, we find that for insertion from an initial conformation outside the bilayer, a 30-million-step equilibration period is usually sufficient, whereas for an initially inserted and helical conformation, 30 million steps is *always* sufficient. Although both initial conformations eventually produce the same equilibrated state, the inserted helical conformation converges more rapidly and is used, with an equilibration period of 50 million steps, in all our simulations (unless otherwise noted).

As a further test that our equilibration period is sufficient, we have also used conformations from peptides at the end of an entire simulation run as starting points for new simulations, and the results at the end of both simulations are within our error bars of one another.

It is worth pointing out that no equilibration would be required if the insertion mechanism is being studied. However, in this work, we find that in every case insertion is fairly easy, as we discuss in Results. Thus we focus on peptide conformations at equilibrium.

## Data collection

Every MC simulation run employs a unique set of random numbers, resulting in a slightly different result each trial (similar to the way in which no two experimental measurements are identical). More accurate data are therefore generated by averaging multiple runs. Here, we have run a minimum of 10 trials for every peptide: five beginning in initially helical and inserted conformations, and five with initially random conformations outside the bilayer. Following equilibration (discussed above), data is collected for 50 million steps. In this article we report the results of the initially inserted conformations, thus our results are averaged over a minimum of five such trials. However, as we will discuss in the appendix on data analysis, in some cases we use more trials.

## RESULTS

### Overview

Overall, we simply input the sequence of  $A\beta 40$  and  $A\beta 42$  and various mutants and run the simulations. As discussed above, we do multiple trials for each peptide and average the results. What we find, briefly, is that the peptides all insert relatively easily into the bilayer if they begin initially outside the bilayer, and we do not find that the FAD mutations significantly effect this ease of insertion. However, we find that the mutations do influence the conformation the peptide adopts once inserted into the bilayer. Therefore, our focus in this work is not on details of how the peptide inserts, though we believe it is likely that insertion proceeds via one of the two main insertion mechanisms described previously (Baumgaertner, 1996; Maddox and Longo, 2002a).

One of our fundamental results is that the peptide appears to exhibit multiple possible inserted conformations which have nearly the same energies, thus allowing the peptide to switch between conformations often in the course of a simulation. We have previously described such behavior as conformational partitioning (Maddox and Longo, 2002b). We find that that the  $A\beta$  peptide and its mutants can always adopt the same small set of conformations. However, the mutations alter the number of MC steps the peptide spends in each of these conformations (which, in a real system, would correspond to the number of inserted peptides in each conformation). These conformations are shown in Figs. 2 and 3.

Essentially, it is quite easy to distinguish three conformations: the first has the last several residues anchored in the lower head region. We call this conformation *transbilayer*. The second conformation is similar, but usually much more prevalent since the last residues are hydrophobic and prefer

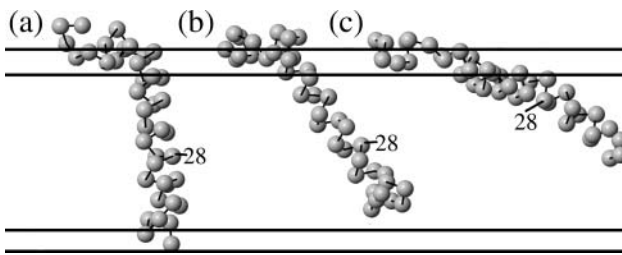


**FIGURE 2** Primary inserted conformations of the  $A\beta$  peptide. We find that in every case, the inserted peptides can adopt essentially three different conformations. Mutations appear to alter the percentage of steps the peptide spends in each conformation but do not fundamentally change the conformations. (a) Transbilayer. The peptide inserts with the last several residues near the C-terminus in the lower lipid head region; the portion crossing the bilayer is roughly helical. (b) Fully inserted. Just like a, except the last several residues are not anchored in the lower head region, meaning that the conformation is fairly flexible. (c) Partially inserted. Like b, except now much more of the peptide is tethered to the upper head region by the polar residues 22–23 and 26–28, whereas before only residues 1–15 or so were in the upper head region. The conformations shown are for  $A\beta 40$ , but  $A\beta 42$  has similar conformations with two additional residues (isoleucine and alanine) at the C-terminus.

to remain in the tail region. This is especially true in the case of  $A\beta 42$ . In this conformation, the essential difference is that the tail of the peptide is not anchored and thus is fairly floppy and able to change the angle it makes with the  $z$  axis easily. We call this conformation *fully inserted*. The third conformation is different in that in the first two, only residues 1–15 or so remain in the upper lipid head region, while in the third conformation, the polar residues 22–23 and/or 26–28 also remain in the upper head region (along with some of their neighbors), where there is still some water content. As a result, the C-terminus (residue 40 or 42) does not stick down into the lipid tail region nearly as far as in the other two conformations. We call this conformation *partially inserted*. In this case all, or almost all, of the peptide is only in the upper leaflet of the bilayer.

This third, partially inserted conformation can be divided into two conformations simply by distinguishing whether it is residues 22–23 that remain in the upper head region, or residues 26–28. This separation of conformations is shown in Fig. 3. Some of our analysis is done grouping these together, and some by separating them, as we will discuss below.

Briefly, we find that when the FAD mutations have an effect on the insertion behavior, it is usually by causing the mutant peptides to favor the partially inserted conformation more than wild-type. The E22G mutant is an exception, as it essentially eliminates this conformation. We refer the reader to the Appendix for detailed discussion of our data analysis procedure. Overall, however, the basic output of the simulation is the number of steps, or percentage of steps, each residue in the peptide spends at each  $z$ -coordinate. We can plot this for all residues (Fig. 4) or particular residues (Figs. 5–7). With some analysis of these (the data analysis is explained in the Appendix) we are able to get accurate measurements of increases or decreases in the number of steps the peptide spends in a given conformation, relative to wild-type. We are able to do this whether we choose to separate the peptide's conformations into three or four groups. Results obtained using these methods are presented in Table 1 and Table 2.

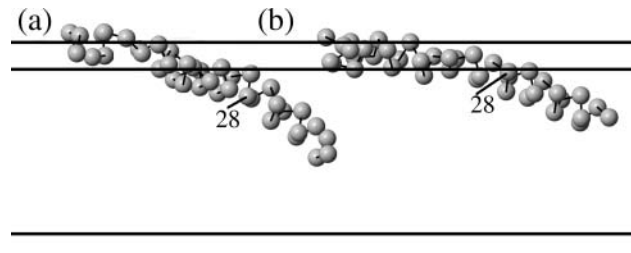


**FIGURE 3** Subconfigurations associated with locations of the polar residues. We can further break up the partially inserted conformation, from Fig. 2 c, into two conformations: (a) a conformation where only residues 22–23 remain in the upper head region, and (b) a conformation where both residues 22–23 and 26–28 remain in the upper head region.

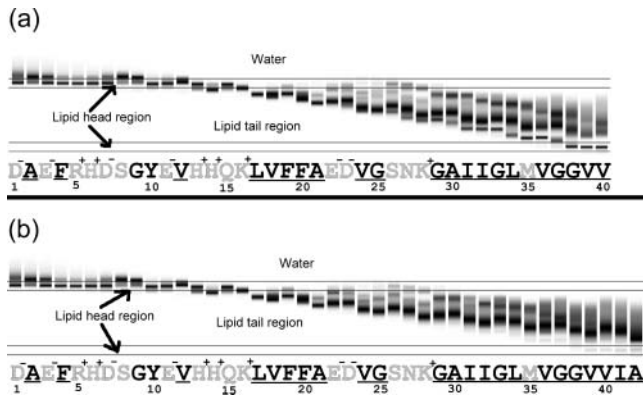


FIGURE 4 Number of steps at each  $z$ -coordinate (vertical axis is  $z$  axis; darker means more steps) plotted versus residue number (sequence shown), from 1–40 for A $\beta$ 40, *a*, and from 1–42 for A $\beta$ 42, *b*. Note that on residue 30, there appear three dark regions, corresponding to three peaks, whereas residues 26 and 28, for example, have four peaks. This result is important for our data analysis. Note also that the transbilayer conformation for A $\beta$ 42 is less common than for A $\beta$ 40 (compare the darkness, or number of steps, of the lowest peak on residue 40 for A $\beta$ 40 and A $\beta$ 42). The sequence of A $\beta$  has polar residues shaded, hydrophobic residues underlined, and charged residues with charges indicated.

### Normal A $\beta$ peptide insertion

As detailed in the Appendix, some results for A $\beta$ 40, A $\beta$ 42, and various mutants, are shown in Figs. 5–7. We have also extracted the number of steps in each conformation and present these (measured as percentages of total steps) in Table 1, along with standard deviations. As we discuss in the Appendix, the percentages for conformations (*b*) and (*c*) are not completely accurate as absolute measures of the number of steps in those conformations, but the change relative to wild-type is accurate.

It is important to note that there is a fundamental difference between A $\beta$ 40 and A $\beta$ 42. While both can adopt all the conformations of Fig. 2, A $\beta$ 42 spends many fewer steps in conformation (*a*). This is because the last two residues of A $\beta$ 42 add significantly to the hydrophobicity of the C-terminus (see sequence in Fig. 4), as both are nonpolar and isoleucine is strongly hydrophobic. One might well ask, however, why A $\beta$ 40 has its last three residues in the lower head region at all, especially the final two valines, which are nonpolar and strongly hydrophobic. To understand this effect, it is worth noting that in this conformation, the transbilayer helix begins after, or around, residue 16, lysine, which is the final charged and polar residue before a number of nonpolar, hydrophobic residues, beginning with leucine. To remove residues 39 and 40 from the lower head region would require either the peptide to insert at a more shallow angle so that these residues do not make contact with the lower head region, or putting a kink in the helix (as in Fig. 2 *b*) so that they do not make contact. In the first case, changing the insertion angle would move lysine, and possibly residues after it (it is immediately followed by

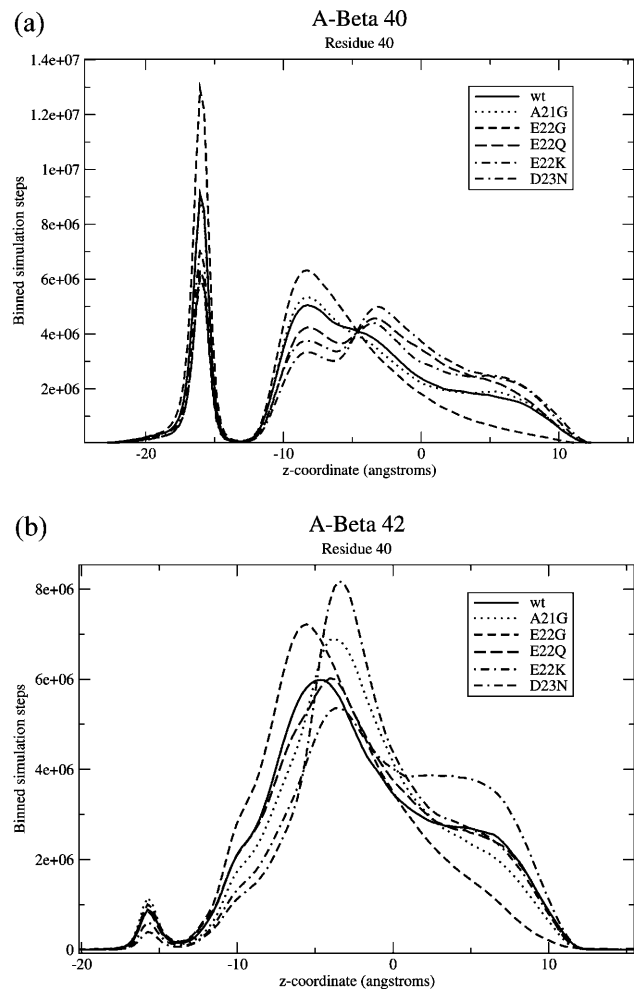


FIGURE 5 Binned numbers of steps spent at each  $z$ -coordinate for residue 40 of (a) A $\beta$ 40 and (b) A $\beta$ 42. Each plot also shows various FAD mutations. It is easily apparent that A $\beta$ 42 spends significantly fewer steps in the fully inserted conformation (*leftmost peak*) compared to A $\beta$ 40. It is difficult to tell much about the other conformations by looking at this distribution for residue 40, but the prevalence of these can be extracted from other residues. Note that the lipid head regions are from  $z = 13.5$  Å to  $z = 18$  Å (and similarly for negative  $z$ ).

valine), into the upper head region where there is still some water. This would be costly energetically. So is putting a kink into the helix. Thus we believe that, in the case of A $\beta$ 40, the energy cost of either putting a kink in the helix, or imbedding K16 and V17 in the upper head region, is comparable to the energy cost of imbedding V39 and V40 in the lower head region, thus the conformation in Fig. 2 *a* does occasionally happen. On the other hand, for A $\beta$ 42, the additional I41 makes this conformation so costly that it almost never happens. This reduction in the transmembrane conformation results in an increase in the prevalence of the other two conformations relative to A $\beta$ 40 which, if correct, could help explain why A $\beta$ 42 is typically more toxic.

It is probably important to point out that our results do not necessarily mean A $\beta$ 40 would be biologically

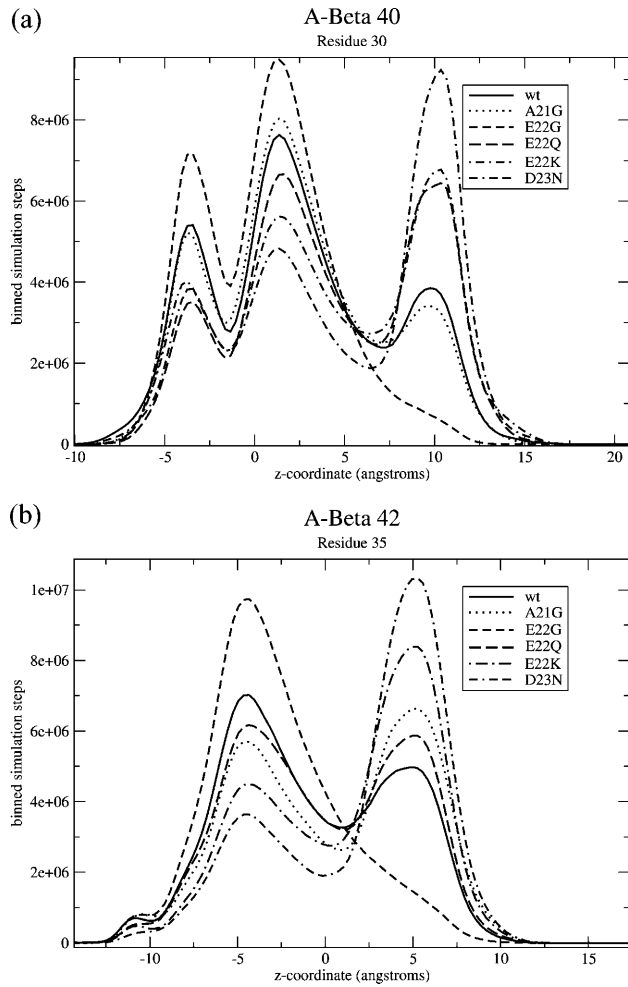


FIGURE 6 Binned number of steps spent at each  $z$ -coordinate for (a) residue 30 of  $\text{A}\beta 40$  and (b) residue 35 of  $\text{A}\beta 42$ . These are the residues we picked which best distinguish three groups of conformations. The leftmost group on both, which is very small for  $\text{A}\beta 42$ , is in conformations that appear nearly transbilayer. The middle group is in conformations that are inserted and fairly floppy, as in Fig. 2 b, and the rightmost group is in the partially inserted conformation. It can be clearly seen that for  $\text{A}\beta 40$ , all of the mutations but E22G and A21G result in an increase in this last peak relative to wild-type, and for  $\text{A}\beta 42$  all of them except E22G do, as well.

transmembrane. We have tried making the bilayer slightly thicker (by 5 Å) and the transbilayer conformation essentially disappears. This means the transmembrane insertion is due to the limited space between head regions, as we argued above. Biologically, the membrane could be slightly thicker than our model, or the peptide might cause a small bulge in the membrane to accommodate a fully inserted, rather than transbilayer, conformation. So, although the simulation does produce this transbilayer conformation, we have no reason to believe that this conformation would be distinct from the fully inserted conformation in biological systems. On the other hand, this conformation does exist in our model. Here, it is the reduction in the prevalence of this conformation that makes the other two conformations more prevalent for  $\text{A}\beta 42$  than  $\text{A}\beta 40$ .

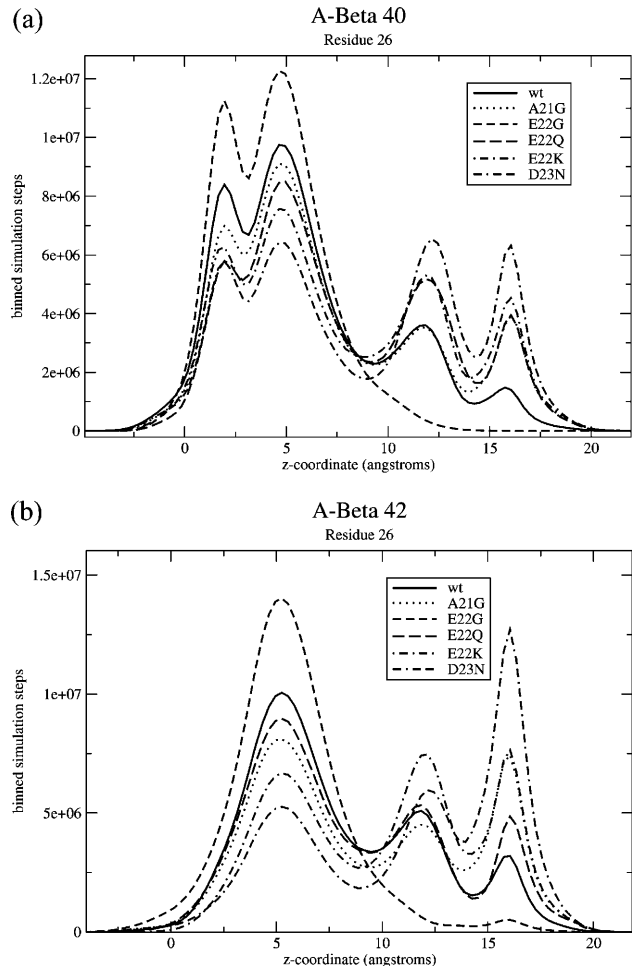


FIGURE 7 Binned number of steps spent at each  $z$ -coordinate for residue 26 of (a)  $\text{A}\beta 40$  and (b)  $\text{A}\beta 42$ . For this residue, there are four apparent peaks, corresponding to the conformations of Fig. 2, a and b, and Fig. 3. For  $\text{A}\beta 42$ , the transbilayer conformation is so small that there is no apparent peak. For  $\text{A}\beta 40$ , it is the leftmost peak, followed by the fully inserted peak, then the partially inserted peaks: the peak of Fig. 3 a, and then the peak of Fig. 3 b. Notice that for both  $\text{A}\beta 40$  and  $\text{A}\beta 42$ , the FAD mutants increase the weight of the rightmost conformations (those of Fig. 3) relative to wild-type, except for the E22G mutant.

## FAD $\text{A}\beta$ peptide insertion

### FAD mutations

There are a number of known FAD mutations, including some involving  $\text{A}\beta$  (as well as others involved in other aspects of the disease including  $\text{A}\beta$  production). These are named by the populations they were first found in and include Flemish (A21G), Arctic (E22G), and Iowa (D23N) (Murakami et al., 2002). Murakami et al. also include Dutch (E22Q) and Italian (E22K) but there is some dispute about whether these are properly to be considered AD mutations (Melchor et al., 2000; Nilsberth et al., 2001; Wattendorff et al., 1995). To understand this, it is important to note that AD is often accompanied by cerebral amyloid angiopathy

**TABLE 1** Frequency of each conformation for native and FAD A $\beta$  peptides

Peptide form	Onset	% Trans.	Three-peak analysis		Four-peak analysis	
			% Fully ins.	% Partially ins.	$\Delta\%$ Upper(a)	$\Delta\%$ Upper(b)
WT A $\beta$ 40	72.8	15.6 $\pm$ 3.8	48 $\pm$ 5.2	36.3 $\pm$ 6.8	—	—
A $\beta$ 42		2.1 $\pm$ 0.5	58.5 $\pm$ 5.6	39.4 $\pm$ 5.8	—	—
A21G A $\beta$ 40	52	17.6 $\pm$ 3.0	48.3 $\pm$ 6.8	34.1 $\pm$ 8.0	0.5 $\pm$ 1.8	2.9 $\pm$ 8.4
A $\beta$ 42		1.9 $\pm$ 0.7	44.4 $\pm$ 5.4	53.7 $\pm$ 5.4	-2.8 $\pm$ 3.2	14.8 $\pm$ 6.9
E22G A $\beta$ 40	57	27.4 $\pm$ 7.5	67.4 $\pm$ 7.0	5.13 $\pm$ 7.0	-11.8 $\pm$ 1.6	-13.2 $\pm$ 6.2
A $\beta$ 42		2.3 $\pm$ 1.7	94.8 $\pm$ 7.0	1.29 $\pm$ 1.0	-16.8 $\pm$ 3.7	-9.6 $\pm$ 5.6
E22Q A $\beta$ 40	?	13.6 $\pm$ 4.6	43.6 $\pm$ 5.5	42.8 $\pm$ 5.5	6.4 $\pm$ 3.5	2.8 $\pm$ 11.0
A $\beta$ 42		2.0 $\pm$ 0.3	55.8 $\pm$ 6.9	42.2 $\pm$ 7.0	4.5 $\pm$ 3.4	-1.8 $\pm$ 8.7
E22K A $\beta$ 40	?	15.5 $\pm$ 9.6	37.9 $\pm$ 5.2	46.6 $\pm$ 6.0	9.9 $\pm$ 2.3	2.2 $\pm$ 10.0
A $\beta$ 42		1.3 $\pm$ 0.8	34.2 $\pm$ 10.5	64.5 $\pm$ 9.4	9.4 $\pm$ 8.0	14.6 $\pm$ 17.1
D22N A $\beta$ 40	69	13.1 $\pm$ 9.2	30.0 $\pm$ 8.8	56.8 $\pm$ 10.2	8.6 $\pm$ 7.2	10.8 $\pm$ 16.2
A $\beta$ 42		1.2 $\pm$ 0.5	41.1 $\pm$ 16.3	57.7 $\pm$ 16.7	0.6 $\pm$ 5.8	16.0 $\pm$ 11.4

Ages of onset (where known) (Grabowski et al., 2001; Li et al., 2002; Nilsberth et al., 2001; Roks et al., 2000) and simulation results: percentage transbilayer, percentages in the fully inserted (Fig. 2 *b*) and partially inserted (Fig. 2 *c*) conformations as calculated from the three-peak analysis on residue 30. The last two columns measure the change in percentage of the conformations of Fig. 3, *a* and *b*, relative to wild-type (from the four-peak analysis). For each mutation, one row represents A $\beta$ 40 and the next A $\beta$ 42. Onset age is not specific to the 40- or 42-residue forms. Here, the only consistent trend that we find is that most of the FAD mutants, with the exception of E22G, appear to increase the percentage of the partially inserted conformation relative to wild-type. This appears to be true for both A $\beta$ 40 and A $\beta$ 42. By way of comparison, the FAD mutations increase fibrillar aggregation of A $\beta$ 42 in vitro in every case except the A21G mutant (Murakami et al., 2002) and increase soluble A $\beta$  levels in every case but the E22G mutant (Lashuel et al., 2002; Nilsberth et al., 2001). To improve statistics, wild-type A $\beta$ 40 results are the average of 25 trials rather than the usual 5; wt A $\beta$ 42 are the average of 20; A21G A $\beta$ 40 20 trials; A21G A $\beta$ 42 10 trials, and A $\beta$ 42 E22Q and D23N 10 trials each. All the rest are five trials, as described in Appendix: Data Analysis.

(CAA), deposition of A $\beta$  in blood vessels of the brain potentially leading to vessel rupture and stroke, especially in FAD cases (Murakami et al., 2002). Wattendorff et al. (1995) point out that classic Alzheimer's plaques are rarely found in the Dutch CAA case and dementia and death are due to cerebral hemorrhage involving damage to blood vessels, as is also the case in the Italian E22K mutant (Melchor et al., 2000). But the fact that AD also involves amyloid angiopathy leaves open the possibility that the Dutch and Italian forms are vascular forms of AD (Wattendorff et al., 1995).

Here, we set aside the issue of whether or not the Dutch and Italian A $\beta$  mutations are actually AD mutations or whether they should be regarded as something different and simply model insertion of these peptides into cell membranes. It is known that even the Dutch E22Q and Italian E22K mutant peptides interact with cell surfaces of cerebral vascular smooth muscle cells and cause cell death in vitro (Melchor et al., 2000). Thus, it is conceivable that the mechanism may be similar to that described by Lin et al. (2001) and the type of cells being damaged may simply be different—either cerebral vascular smooth muscle cells (Melchor et al., 2000) or brain pericytes (Verbeek et al., 1997) rather than neurons. For simplicity, we will call all of these FAD mutations.

It is also important to note that these A $\beta$  mutations are autosomal-dominant (Nilsberth et al., 2001) and, in addition to lowering the age of onset for AD compared to sporadic cases, cause AD in all subjects with the mutations who live long enough. Many of these mutations also lead to increased

A $\beta$  levels, but that cannot be the sole cause, as at least the Arctic mutation (Lashuel et al., 2002) leads to decreased levels. The cause of disease also cannot be simply the increased propensity to form fibrils or aggregates, because at least the Flemish mutation does not increase fibril formation (Murakami et al., 2002).

#### FAD mutation results

Results for these mutations are shown in Figs. 5–7, and presented in reduced form in Table 1. We find that the most consistent difference in results relative to wild-type, for both A $\beta$ 40 and A $\beta$ 42, is that four of the five FAD mutants increase the number of steps the peptide is in a conformation like that of Fig. 2 *c*. The E22G mutant, however, results in a huge decrease of this conformation.

To understand our results, consider the changes in polarity and hydrophobicity the mutations involve. The polarity and hydrophobicity values used in this model have been tabulated before (Maddox and Longo, 2002a) and will not be repeated here, but it is worthwhile to discuss the mutations briefly. The A21G mutant involves a decrease in hydrophobicity, hence should cause residue 21 to more strongly prefer to be in the upper head region and thus result in an increase in the prevalence of the partially inserted conformation (Fig. 2 *c*). This is what we find, at least for A $\beta$ 42 (for A $\beta$ 40, the percentage stays about the same). The E22Q mutant involves a fairly large increase in polarity and slight increase in hydrophobicity, thus the polarity should dominate and cause

**TABLE 2** Frequency of each conformation for artificial A $\beta$  mutants

Peptide form	% Trans.	Three-peak analysis		Four-peak analysis	
		% Fully ins.	% Partially ins.	$\Delta\%$ Upper(a)	$\Delta\%$ Upper(b)
WT A $\beta$ 40	15.6 $\pm$ 3.8	48 $\pm$ 5.2	36.3 $\pm$ 6.8	—	—
A $\beta$ 42	2.1 $\pm$ 0.5	58.5 $\pm$ 5.6	39.4 $\pm$ 5.8	—	—
E22QD23N A $\beta$ 40	15.5 $\pm$ 5.0	30.0 $\pm$ 6.4	54.6 $\pm$ 6.9	4.4 $\pm$ 6.3	13.9 $\pm$ 16.2
A $\beta$ 42	0.9 $\pm$ 0.7	24.6 $\pm$ 11.4	74.4 $\pm$ 11.4	4.0 $\pm$ 10.5	30.9 $\pm$ 19.0
E22A A $\beta$ 40	23.1 $\pm$ 7.6	71.7 $\pm$ 7.1	5.2 $\pm$ 0.7	-10.8 $\pm$ 2.3	-13.3 $\pm$ 6.3
A $\beta$ 42	2.0 $\pm$ 0.4	85.6 $\pm$ 2.1	12.4 $\pm$ 2.0	-13.8 $\pm$ 7.0	-11.4 $\pm$ 4.2
E22D A $\beta$ 40	22.9 $\pm$ 8.9	64.9 $\pm$ 7.6	12.2 $\pm$ 2.0	-3.9 $\pm$ 2.6	-13.1 $\pm$ 6.2
A $\beta$ 42	1.9 $\pm$ 1.1	62.9 $\pm$ 6.6	35.2 $\pm$ 6.6	-5.9 $\pm$ 3.4	-0.4 $\pm$ 10.7
A2S A $\beta$ 40	17.6 $\pm$ 9.1	49.3 $\pm$ 6.4	33.1 $\pm$ 5.0	-1.2 $\pm$ 9.9	-3.2 $\pm$ 9.7
A $\beta$ 42	2.2 $\pm$ 1.3	60.4 $\pm$ 3.4	37.4 $\pm$ 3.3	2.4 $\pm$ 3.3	-5.3 $\pm$ 8.7
F19S A $\beta$ 40	1.6 $\pm$ 2.4	5.3 $\pm$ 4.4	93.1 $\pm$ 4.9	4.9 $\pm$ 10.3	57.9 $\pm$ 16.1
A $\beta$ 42	0.1 $\pm$ 0.1	10.8 $\pm$ 5.2	89.1 $\pm$ 5.2	7.8 $\pm$ 13.6	43.6 $\pm$ 14.9
I32S A $\beta$ 40	14.2 $\pm$ 7.0	34.7 $\pm$ 8.7	51.1 $\pm$ 10.7	-1.7 $\pm$ 3.2	17.0 $\pm$ 12.6
A $\beta$ 42	1.5 $\pm$ 0.7	49.5 $\pm$ 13.9	49.1 $\pm$ 14.1	-1.1 $\pm$ 4.5	10.2 $\pm$ 11.5
I32V A $\beta$ 40	16.0 $\pm$ 3.9	58.8 $\pm$ 2.8	25.3 $\pm$ 1.3	4.4 $\pm$ 1.6	-10.8 $\pm$ 6.8
A $\beta$ 42	2.5 $\pm$ 1.2	63.2 $\pm$ 2.1	34.4 $\pm$ 2.0	-0.1 $\pm$ 3.7	-5.7 $\pm$ 5.6
V36E A $\beta$ 40	83.0 $\pm$ 13.9	10.6 $\pm$ 9.3	6.4 $\pm$ 6.2	-12.7 $\pm$ 3.0	-5.3 $\pm$ 13.3
A $\beta$ 42	16.7 $\pm$ 11.9	36.2 $\pm$ 19.5	47.1 $\pm$ 10.5	1.6 $\pm$ 5.1	5.6 $\pm$ 11.8
H6R A $\beta$ 40	17.3 $\pm$ 4.8	47.7 $\pm$ 7.7	35.0 $\pm$ 8.4	2.2 $\pm$ 2.5	-1.2 $\pm$ 8.8
A $\beta$ 42	2.0 $\pm$ 0.6	52.9 $\pm$ 8.2	45.1 $\pm$ 8.4	1.8 $\pm$ 3.7	2.5 $\pm$ 7.3

Shown are results for artificial A $\beta$  mutants mentioned in the literature: percentage transbilayer, percentages in the fully inserted (Fig. 2 b) and partially inserted (Fig. 2 c) conformations as calculated from the three-peak analysis on residue 30. The last two columns measure the change in percentage of the conformations of Fig. 3, a and b, relative to wild-type (from the four-peak analysis). The A $\beta$ 40 E22QD23N mutant is more toxic to HCSM cells than either mutant alone (Van Nostrand et al., 2001), whereas the E22D mutant of A $\beta$ 40 is not toxic to HCSM cells and the E22A mutant is (Melchor et al., 2000). The A2S, F19S, I32V, I32S, and V36E mutants are known to reduce aggregation of A $\beta$ 42 (Wurth et al., 2002), and the H6R mutant has been suggested as an FAD mutant (Janssen et al., 2003).

residue 22 to strongly prefer the upper head region, as we find. The E22K mutant is quite similar, but involves an even larger increase in polarity, and should also cause residue 22 to prefer the upper head region, as we find. And the D23N mutant involves a similar increase in polarity and slight increase in hydrophobicity, so again the polarity should dominate and increase this conformation, as we find. On the other hand, the E22G mutant replaces a polar, charged residue with a neutral, nonpolar residue and thus residue 22 is now mostly indifferent. This results in the observed huge decrease in the partially inserted conformation.

On one hand, the different behavior of the E22G mutant could be taken as evidence that there is no consistent change in insertion behavior, and thus suggest that this may not be the toxicity mechanism, or at least that oligomerization, not insertion, is important. That is certainly a possible meaning of these results. However, we would suggest that the reader compare the conformation of Fig. 2 c with the channel structure of Durell et al. (1994), specifically in Fig. 4 of that article. Note that there are two helices predicted, from residues 15–24, running near the upper head region, and from 25–40 or 25–42, inserted. In Fig. 2 c, we have a nearly helical region from around residues 14–24 or 25 that is near the upper head region, and one from 25–40 which hangs

down inserted. Thus it resembles the predicted structure more than either of the other conformations. In the structure prediction, the part of the chain before residue 15 folds down inside the oligomer and forms a  $\beta$ -barrel, which we obviously do not capture here because we do not have oligomers necessary to stabilize such a structure, and because the model is not designed to capture  $\beta$ -structure. With the similarity of Fig. 2 c to the predicted channel structure in mind, we form the hypothesis that the partially inserted conformations (Fig. 2 c, or Fig. 3, a and b) are more likely to form channels, simply because of their resemblance to the structure of the monomers making up the channels. Below, in the subsection “Insertion of other mutant A $\beta$  peptides”, we test this hypothesis against some experimental data for artificial A $\beta$  mutants, and present predictions for further tests. One might argue that the observed changes in the prevalence of different conformations are relatively small and thus would be unlikely to result in a large difference in the toxicity of the different mutants. However, these channels consist of eight or twelve monomers. If one thinks of a large number of monomers inserted in a bilayer, some will be in each conformation at any given time, so we can think of the concentration of each conformation. Consider, then, the concentration of the conformation that can form channels.

The time it takes for 12 monomers within a bilayer to find each other, or the probability, should scale as  $c^{12}$ , where  $c$  is this concentration. Thus a small difference in the amount in the proper conformation could make a big difference in the likelihood of forming channels.

### Insertion of other mutant A $\beta$ peptides

A variety of other data is available on mutant A $\beta$  peptides. Some reduce aggregation in vitro (Wurth et al., 2002), some might cause FAD (Janssen et al., 2003), and some have various effects on cultured cerebrovascular smooth muscle cells (Melchor et al., 2000; Van Nostrand et al., 2001). Here, we examine some of the mutations which have been mentioned in the literature as a test of our hypothesis—if it is right, and toxicity depends in part on the relative prevalence of the partially inserted conformation, our results ought to correlate with the experimental toxicity measurements.

First, we address the E22Q,D23N A $\beta$ 40 double mutant created by Van Nostrand et al. (2001). This mutation's effect has been examined on human cerebrovascular smooth muscle cells (HCSM cells) because the E22Q mutation causes especially pronounced cerebral amyloid angiopathy and patients with this mutation typically die of hemorrhage, as discussed above. HCSM cells are known to degenerate in CAA in a manner that is associated with A $\beta$  deposition (Melchor et al., 2000). Van Nostrand et al. (2001) found that the E22Q,D23N double mutant is even more toxic to HCSM cells than E22Q or D23N alone. Our idea was that the mechanism for this toxicity also involves insertion of the peptide and formation of channels, so we modeled this mutant as well. Results for this mutant are shown in Table 2; we find that the prevalence of the partially inserted conformation does increase relative to wild-type. Relative to the D23N mutant, which we would predict would be the more toxic of the E22Q and D23N mutants, we observe an increase in the partially inserted conformation only for A $\beta$ 42. Again, however, we would argue simply based on the residue properties that since both the E22Q and D23N mutants increase preference of those residues for the upper head region, the double mutant should have a stronger effect on this than either alone, and thus we expect that, given better statistics, we would agree with Van Nostrand et al. (2001) and predict that the double mutant is more toxic than either alone.

Melchor et al. (2000) have found that an artificial E22D mutant of A $\beta$ 40 does not effect HCSM cells, in contrast to biological E22Q and E22K mutants. They also observed that the A $\beta$ 40 E22A mutant is toxic to HCSM cells. Therefore we model insertion of E22D and find (Table 2) that the E22D mutant results in a decrease in the partially inserted conformation (as one would expect due to the decrease in polarity), especially for A $\beta$ 40. The E22A mutant results in a large decrease in the partially inserted conformation for both A $\beta$ 40 and A $\beta$ 42 (again, as one would expect due to the decrease in polarity). Thus, based on our hypothesis, we would

agree that the E22D A $\beta$ 40 mutant would not be toxic, but disagree that the E22A mutant would be toxic. This could be taken as evidence against our hypothesis or evidence that the toxicity mechanism is different for HCSM cells.

Janssen et al. (2003) recently identified a previously unknown mutation in the A $\beta$  peptide in two early-onset AD patients in the same family. This mutation, H6R, produced ages of onset  $\sim$ 55. We have here tried this mutation (results in Table 2) and find that it produces insertion behavior that is within error bars of wild-type. Given the position of the mutation, this is what we would expect, as it is within the range of amino acids (1–14 or more) that are firmly anchored in or near the upper head region, where there is some water content. Replacing histidine with arginine, which is even more polar, does not have a strong effect on this as both try to remain where there is water, i.e., the surface of the upper head region. Thus, if toxicity depends only on insertion conformation, we would suggest that this is indeed *not* a FAD mutation. Thus we would suggest testing toxicity of this mutant in cell culture, particularly as already done for A $\beta$ 42 by Lin et al. (2001).

Some in vitro work has been done to find artificial mutants that can reduce aggregation of A $\beta$ 42 (Wurth et al., 2002). Unfortunately, this has not yet been extended to include A $\beta$ 40. However, we selected some of the point mutations which are known to reduce aggregation of A $\beta$ 42 and modeled the insertion of these. We tried A2S, F19S, I32V, I32S, and V36E. Results are shown in Table 2. We find that F19S and I32S strongly increase the prevalence of the partially inserted conformation for both A $\beta$ 40 and A $\beta$ 42. For F19S, this is due to the substitution of polar serine for strongly hydrophobic phenylalanine, causing residue 29 to prefer the upper head region; for I32S, the reason is similar. In this case, the conformation is actually different from normal in that residue 32 also sticks in the upper head region. In contrast, the I32V mutant does not result in a large change relative to wild-type, consistent with the relatively small change between isoleucine and valine. Unsurprisingly, the A2S mutant makes no change to insertion behavior (residue 2 is firmly in the upper head region, so changing it to polar makes little difference). The V36E mutant, however, as one might expect, drastically increases the number of steps that the peptide is transbilayer, as the polar and charged glutamic acid strongly prefers to be in an environment with more water. Thus it decreases the prevalence of the partially inserted and fully inserted conformations. Thus we would predict that, if our hypothesis is correct, F19S and I32S should be the most toxic, I32V and A2S should be comparable to wild-type, and V36E *might* be much less toxic than wild-type. We say *might* because this probably depends on the thickness of the bilayer; if the bilayer is too thick it will probably behave just like wild-type since the E36 could not reach the lower head region. Thus a testable experimental prediction of our hypothesis is that toxicity of these mutants would be related to their insertion behavior as just described.

We can make a second prediction which is simply based on the observed insertion behavior of  $\text{A}\beta$ 42. Looking at the insertion behavior of the  $\text{A}\beta$ 42 versions of the Wurth et al. (2000) mutants, we find that I32V, A2S, and possibly V36E insert more like natural  $\text{A}\beta$ 42, whereas F19S, I32S, and possibly V36E insert differently. The reduction in aggregation splits the group differently—I32S aggregates most, then A2S, V36E, and F19S are similar to one another and intermediate, and I32V aggregates least (Wurth et al., 2002). So if fibrillar aggregation primarily causes toxicity, experiments looking at toxicity should see the latter grouping, whereas if insertion behavior is of much more importance, toxicity experiments should see the former grouping.

## DISCUSSION AND CONCLUSIONS

We have here presented work applying a model of peptide insertion to  $\text{A}\beta$ , a peptide implicated in Alzheimer's disease. Specifically, we have examined the effect of FAD mutations on the peptide's insertion behavior, with the idea that any successful hypothetical toxicity mechanism should be able to explain why FAD mutations are toxic. Thus if FAD mutants do not affect peptide insertion into, or oligomerization within, membranes, the ion channel toxicity mechanism proposed previously (Arispe et al., 1993; Durell et al., 1994; Lin et al., 2001) is probably not relevant biologically.

What we find is that the FAD mutations do affect peptide insertion. Four of these five mutations involve an increase in polarity or decrease in hydrophobicity and thus cause the peptide to prefer (relative to wild-type) a conformation where those residues are in the upper lipid head region (i.e., Fig. 2 c). It is interesting to note that a channel structure suggested previously (Durell et al. (1994), see Fig. 4) has these residues laying along the surface of the bilayer. Thus we find that four of the five FAD mutations increase the resemblance to this configuration.

Based on this similarity, we develop the hypothesis that causing the peptide to hang up in the upper leaflet (the partially inserted conformation) facilitates formation of harmful channels. We test this hypothesis on several artificial mutations examined in vitro and find that it can explain the change in toxicity of two and is wrong on a third. As a further test of our hypothesis, we can offer some testable predictions. For example, if the hypothesis is right, we would suggest that the F19S mutant would increase toxicity of  $\text{A}\beta$  relative to wild-type. Additionally, there are several mutations known to reduce aggregation of  $\text{A}\beta$ 42 that we predict would promote the insertion behavior that would facilitate channel formation. Thus, it would be simple to distinguish between the channel formation toxicity mechanism and the aggregation toxicity mechanism by looking at the toxicity of these mutants. Even more evidence could be provided by replicating the work of Lin et al. (2001) but using various FAD mutants and looking at how these effect the abundance of channels. Additional information could

also be gained from theoretical work along the lines of that by Durell et al. (1994) to see what effect these FAD mutants would have on channel structures.

Overall, this approach of modeling peptide insertion provides a simple way of making concrete predictions to distinguish the proposed mechanism of channel formation from others. The limitation of this approach, however, is that we can only look at insertion of single peptides, and not interaction between these. This is fine if formation of channels depends on having peptides initially in the correct conformations, which seems reasonable. However, it is also possible that interaction between inserted peptides causes them to adopt conformations appropriate for channel formation. If this is the case, then insight into channel formation would require a more sophisticated model that can include interaction between peptides. Even if this is not the case, including interaction between peptides will certainly answer the question of whether FAD mutants affect channel formation in a consistent way much more thoroughly than we are able to do here. Therefore, this would be a logical continuation of this work and is something we hope to do in the future.

Even if our hypothesis proves to be wrong, we have shown that the FAD mutants affect insertion behavior of the  $\text{A}\beta$  peptide into lipid bilayers, and provided an understanding as to why the FAD mutants affect insertion in the way they do.

In conclusion, our work shows that most FAD mutations have a significant effect on the insertion of the  $\text{A}\beta$  peptide in lipid bilayers in this theoretical model, and this effect can easily be understood by looking at the change in polarity and hydrophobicity accompanying the mutations. The effect of FAD mutations on insertion has not been studied previously, and may be significant. Additionally, we offer a hypothesis based on promoting channel formation by causing peptides to insert less fully that can help explain toxicity of  $\text{A}\beta$  FAD mutants, as well as several artificial mutants studied in vitro. While this hypothesis is unproven, it is based on the observation that these peptides do insert into cell membranes and form ion channels (Lin et al., 2001), and similarities to theoretically predicted channel structures (Durell et al., 1994). We provide testable predictions based on this hypothesis. It should be simple for experimentalists to disprove this hypothesis, if it is false, or to offer additional evidence for it, if they follow the experimental suggestions we offer above. Additionally, our work suggests the value of further modeling work to describe the full formation of these channels, rather than just single-peptide insertion.

## APPENDIX: DATA ANALYSIS

The basic output of the simulation is the binned number of steps—essentially the frequency with which each residue is found at each  $z$ -coordinate. This can be plotted across all residues and illustrates, as in Fig. 4, that there are multiple conformations that the peptide can switch between.

In terms of data analysis, it is more useful to plot  $z$ -distributions of specific residues which can be used to distinguish between the conforma-

tions described above. For example, residue 40 has a well-defined peak in the lower head region that can be used to distinguish the transbilayer conformation from the other conformations. A plot of residue 40  $z$ -distributions for various mutations is shown in Fig. 5.

It is somewhat more difficult to distinguish exactly how many steps the peptide spends in the fully inserted and partially inserted conformations (Fig. 2, *b* and *c*). To understand this, it is important to recognize that each conformation results in a peak for a given residue. That is, from Fig. 2, one can easily see that the position of residue 28 has three significantly different locations depending on which conformation the peptide is in. As it turns out, it also has a fourth, which is not very different from the third, as can be seen in Fig. 3. Unfortunately, these peaks tend to overlap with each other quite significantly—that is, residue 28 can sometimes have similar locations whether it is in the partially inserted conformation or the fully inserted conformation. This means that, to extract the number of steps in a given conformation from the data, it becomes necessary to fit some function to the peaks and then calculate the number of steps from that.

To do this, we select residues where the peaks appear to be particularly well separated. For one, we choose residue 30 (for A $\beta$ 40), because at that residue, the peaks corresponding to the two partially inserted conformations actually overlap—that is, residue 30 has the same average location no matter whether it is residues 22–23 alone that are stuck in the upper head region, or 22–23 and 26–28. This means that we can extract the weight of conformation from Fig. 2 *c*—the conformation grouping these two together—by looking at this residue. For A $\beta$ 42, the two peaks of the partially inserted conformation do not quite overlap for residue 30, but do for residue 35, so we do the same analysis, but for residue 35. A plot of the number of steps at each  $z$ -value for these residues is shown in Fig. 6.

To separate the two partially inserted conformations of Fig. 3, we choose three residues that have four peaks that are the most well-separated (unlike residue 30 or 35, where these two peaks merge into one). These are residues 26, 28, and 31. Plots of the number of steps at each  $z$ -value for different mutations for one of these residues, residue 26, are shown in Fig. 7.

Our goal was to find the number of steps in each conformation. Having chosen the residues where the peaks are the best separated, it is necessary to find the number of steps under each peak. Since they overlap, we find that the best way to do this is to use the least-squares method to find fits to each peak that best describe the whole function. This is probably best understood using a concrete example, for which we choose residue 26.

For residue 26, we know there are four peaks, and, as seen in Fig. 7, the locations of these are fairly clearly visible. To fit these peaks, we begin by averaging all of our results for the wild-type form of A $\beta$ 40. We assume that the peaks are Gaussian. Since the peaks are reasonably well separated, we assume initially that the center of each Gaussian is at the maximum. Then, we perform a least-squares fit of the standard deviation and amplitude of each Gaussian. Particularly, we perform our fit by looping through the peaks and suggesting changes first to the standard deviation and then to the amplitude. Each time, we try both increasing and decreasing the standard deviation by a specified step size, and check whether this improves the quality of the fit. We then move on to the next peak and do the same thing, then repeat the process for the amplitude. Then we reduce the step size and repeat the whole process. We do this until the fit can no longer be improved by further iterations of the process. Having done all that, we also then try altering the locations of the centers of the Gaussians slightly to see if it improves the fit. Having then selected optimal standard deviations and center locations, we store those, and assume that the shape and location of each peak will remain the same for other simulations, and that simply the amplitudes will vary. A sample such fit is shown in Fig. 8. As is apparent from the figure, the fit is good. Therefore, we concluded that assuming the peaks are Gaussian is sufficient, at least to get a reasonable estimate of the number of steps in each conformation.

Having done this, we are able to then perform a four parameter fit for every other data set for every A $\beta$ 40 mutation data set, simply by fitting the amplitudes while keeping the standard deviations and peak locations fixed. We have also tried allowing the standard deviations to vary when doing these subsequent fits but this does not substantially improve the quality of

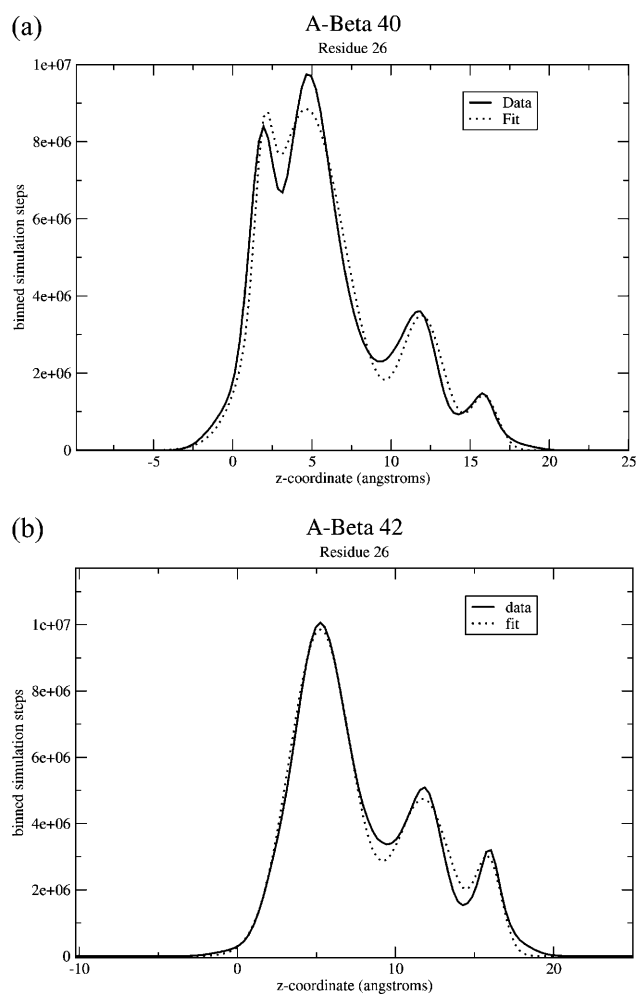


FIGURE 8 Binned number of steps spent at each  $z$ -coordinate for residue 26 of (a) A $\beta$ 40 and (b) A $\beta$ 42, along with fits used for data analysis. Shown here are the data for wild-type, compared to fits of Gaussians, as described in Appendix: Data Analysis. The Gaussians appear to provide fairly good fits and thus we use these in this work to calculate the number of steps in each conformation.

the fit, and it seems reasonable that the shape of a given peak for a given residue should be constant.

We apply a similar technique to fitting residues 28 and 31, and residue 30, but we fit residue 30 using only three peaks, and we do the same for A $\beta$ 42. Additionally, using this technique, we are able to calculate standard deviations for a given peptide or mutant. For example, for the D23N mutant, where residue 23 is changed from aspartate (D) to asparagine (N), we perform a fit separately for each of our five MC runs and calculate the area under each peak. Then, we average the results over all five trials and calculate the standard deviation.

For the four-peak case, it is somewhat difficult to accurately separate the third and fourth peaks, thus it helps that we are able to separately perform fits to four peaks on residues 26, 28, and 31. We are thus able to take the apparent change of steps under each of these three peaks relative to the wild-type and average over all three residues. This significantly reduces our error.

There is one more factor which complicates issues. Going back to our earlier example of the location of residue 28 in Fig. 2, it appears in very different positions along the  $z$  axis depending on which conformation the peptide is in. However, it is also possible to have conformations where residue 28 may, for example, be quite low, like it is in the transbilayer

conformation (Fig. 2 *a*) but residues 38–40 are not in the lower leaflet. This effect gets worse the further the residue being examined is from residue 40, and is apparent in Figs. 6 and 7 as the area under the transbilayer peak on those residues is obviously much larger than the area under the same peak on residue 40, simply because more conformations look similar to the transbilayer conformation.

This means that the calculated number of steps under each peak for residues 26, 28, 30, and 31, while accurate, are not really to be taken as a measure of how many simulation steps the peptide spends in each of those conformations. Since the peak shapes remain constant over the different mutations, however, these *do* accurately describe the change relative to the wild-type. That is, an increase in the prevalence of the conformation of Fig. 2 *c* relative to wild-type for a given mutation is correct, while the absolute number of steps in that conformation may not be accurate, except for the conformation of Fig. 2 *a*, which we can extract accurately from residue 40.

As we discussed above, for many of the peptides we have studied results are averaged over five trials. However, for some we have used significantly more trials. Specifically, for wild-type of  $\text{A}\beta 40$  and  $\text{A}\beta 42$ , we used more trials, as it was particularly important to have a good average for those results since we compare all of our other results to those. For  $\text{A}\beta 40$  we used 25 trials; for  $\text{A}\beta 42$  we used 20. Additionally, for mutants with particularly small changes relative to wild-type, or particularly large standard deviations, we also used more runs. We did 20 trials for A21G  $\text{A}\beta 40$ ; 10 for A21G  $\text{A}\beta 42$ ; and 10 each for  $\text{A}\beta 42$  E22Q and D23N. Of the artificial mutants, we did 10 trials for  $\text{A}\beta 40$  and  $\text{A}\beta 42$  of both I32S and H6R.

We are grateful to R. Lal and G. Millhauser for useful discussions, and W. Pickett for a donation of computer time.

We acknowledge support of the National Science Foundation (Integrative Graduate Education and Research Traineeship Program grants DGE-9972741 and PHY99-07949 to D.L.M.), the U.S. Army (Congressionally Directed Medical Research Fund, grant N0020132 to D.L.C.), the Materials Research Science and Engineering Center Program of the National Science Foundation (under award number DMR-0213618 to M.L.L.), and the Nanoscale Interdisciplinary Research Teams Program of the National Science Foundation (under award number 0210807). M.L.L. acknowledges the generous gift of Joe and Essie Smith for endowing part of this work.

## REFERENCES

Arispe, E., E. Rojas, and H. B. Pollard. 1993. Alzheimer disease amyloid  $\beta$  protein forms calcium channels in bilayer membranes: blockade by tromethane and aluminum. *Proc. Natl. Acad. Sci. USA*. 90:567–571.

Baumgaertner, A. 1996. Insertion and hairpin formation of membrane proteins: a Monte Carlo study. *Biophys. J.* 71:1248–1255.

Coles, M., W. Bicknell, A. A. Watson, D. P. Fairlie, and D. J. Craik. 1998. Solution Structure of the amyloid  $\beta$ -peptide (1–40) in a water-micelle environment. Is the membrane-spanning domain where we think it is? *Biochemistry*. 37:11064–11077.

Dickson, T. C., and J. C. Vickers. 2001. The morphological phenotype of  $\beta$ -amyloid plaques and associated neuritic changes in Alzheimer's disease. *Neuroscience*. 105:99–107.

Durell, S. R., H. R. Guy, N. Arispe, E. Rojas, and H. B. Pollard. 1994. Theoretical models of the ion channel structure of amyloid  $\beta$ -protein. *Biophys. J.* 67:2137–2145.

Grabowski, T. J., H. S. Cho., J. P. G. Vonsattel, G. W. Rebeck, and S. M. Greenberg. 2001. Novel amyloid precursor protein mutation in an Iowa family with dementia and severe cerebral amyloid angiopathy. *Ann. Neurol.* 49:697–705.

Griffith, O. H., P. H. Dehlinger, and S. P. Van. 1974. Shape of the hydrophobic barrier of phospholipid bilayers (evidence of water penetration). *J. Membr. Biol.* 15:159–192.

Hartley, D. M., D. M. Walsh, C. P. Ye, T. Diehl, S. Vasquez, P. M. Vassilev, D. B. Teplow, and D. J. Selkoe. 1999. Protomembrane intermediates of amyloid  $\beta$ -protein induce acute electrophysiological changes and progressive neurotoxicity in cortical neurons. *J. Neurosci.* 19:8876–8884.

Janssen, J. C., J. A. Beck, T. A. Campbell, A. Dickinson, N. C. Fox, R. J. Harvey, H. Houlden, M. N. Rossor, and J. Collinge. 2003. Early onset familial Alzheimer's disease: mutation frequency in 31 families. *Neurology*. 60:235–239.

Jarrett, J. T., E. P. Berger, and P. T. Lansbury, Jr. 1993. The carboxy terminus of the  $\beta$  amyloid protein is critical for the seeding of amyloid formation: implications for the pathogenesis of Alzheimer's disease. *Biochemistry*. 32:4693–4697.

Lambert, M. P., A. K. Barlow, B. A. Chromy, C. Edwards, R. Freed, M. Liosatos, T. E. Morgan, I. Rozovsky, B. Trommer, K. L. Viola, P. Wals, C. Zhang, C. E. Finch, G. A. Kraft, and W. L. Klein. 1998. Diffusible, nonfibrillar ligands derived from  $\text{A}\beta_{1–42}$  are potent central nervous system neurotoxins. *Proc. Natl. Acad. Sci. USA*. 95:6448–6453.

Lashuel, H. A., D. Hartley, B. M. Petre, T. Walz, and P. T. Lansbury, Jr. 2002. Amyloid pores from pathogenic mutations. *Nature*. 418:291.

Li, Y.-J., W. K. Scott, D. J. Hedges, F. Zhang, P. C. Gaskell, M. A. Nance, R. L. Watts, J. P. Hubble, W. C. Koller, R. Pahwa, M. B. Stern, B. C. Hiner, J. Jankovic, F. A. Allen, Jr., C. G. Goetz, F. Mastaglia, J. M. Stajich, R. A. Gibson, L. T. Middleton, A. M. Saunders, B. L. Scott, G. W. Small, K. K. Nicodemus, A. D. Reed, D. E. Schmeichel, K. A. Welsh-Bohmer, P. M. Conneally, A. D. Roses, J. R. Gilbert, J. M. Vance, J. L. Haines, and M. A. Pericak-Vance. 2002. Age at onset in two common neurodegenerative diseases is genetically controlled. *Am. J. Hum. Genet.* 70:985–993.

Lin, H., R. Bhatia, and R. Lal. 2001. Amyloid  $\beta$  protein forms ion channels: implications for Alzheimer's disease pathophysiology. *FASEB J.* 15:2433–2444.

Maddox, M. W., and M. L. Longo. 2002a. A Monte Carlo study of peptide insertion into lipid bilayers: equilibrium conformations and insertion mechanisms. *Biophys. J.* 82:244–263.

Maddox, M. W., and M. L. Longo. 2002b. Conformational partitioning of the fusion peptide of HIV-1 gp41 and its structural analogs in bilayer membranes. *Biophys. J.* 83:3088–3096.

Melchor, J. P., L. McVoy and W. E. Van Nostrand. 2000. Charge alterations of E22 enhance the pathogenic properties of the amyloid  $\beta$ -protein. *J. Neurochem.* 74:2209–2212.

Milik, M., and J. Skolnick. 1992. Spontaneous insertion of polypeptide chains into membranes: a Monte Carlo Model. *Proc. Natl. Acad. Soc. USA*. 89:9391–9395.

Milik, M., and J. Skolnick. 1993. Insertion of peptide chains into lipid membranes: an off-lattice Monte Carlo dynamics model. *Proteins Struct. Funct. Genet.* 15:10–25.

Murakami, K., K. Irie, A. Morimoto, H. Ohigashi, M. Shindo, M. Nago, T. Shimizu, and T. Shirasawa. 2002. Synthesis, aggregation, neurotoxicity, and secondary structure of various  $\text{A}\beta_{1–42}$  mutations of familial Alzheimer's disease at positions 21–23. *Biochem. Biophys. Res. Commun.* 294:5–10.

Nilsberth, C., A. Westlind-Danielson, C. B. Eckman, M. M. Condron, K. Axelman, C. Forsell, C. Sten, J. Luthman, D. B. Teplow, S. G. Younkin, J. Näslund, and L. Lannfelt. 2001. The “Arctic” APP mutation (E693G) causes Alzheimer's disease by enhanced  $\text{A}\beta$  protofibril formation. *Nat. Neurosci.* 4:887–893.

Pellegrini-Calace, M., A. Carotti, and D. T. Jones. 2003. Folding in lipid membranes (FILM): a novel method for the prediction of small membrane protein 3D structures. *Proteins*. 50:537–545.

Roks, G., F. Van Harskamp, I. De Koning, C. De Jonghe, S. Kumar-Singh, A. Tibbel, H. Tanghe, M. F. Niermeijer, A. Hofman, J. C. Van Swieten, C. Van Broeckhoven, and C. M. Van Duijn. 2000. Presentation of amyloidosis in carriers of the codon 692 mutation in the amyloid precursor protein gene (APP692). *Brain*. 123:2130–2140.

Roseman, M. A. 1988. Hydrophilicity of polar amino acid side chains is markedly reduced by flanking peptide bonds. *J. Mol. Biol.* 200:513–522.

Selkoe, D. J. 2001. Alzheimer's disease: genes, proteins and therapy. *Physiol. Rev.* 82:741–766.

Van Nostrand, W. E., J. P. Melchor, H. S. Cho, S. M. Greenberg, and G. W. Rebeck. 2001. Pathogenic effects of D23N Iowa mutant amyloid  $\beta$ -protein. *J. Biol. Chem.* 276:32860–32866.

Verbeek, M. M., R. M. W. de Waal, J. J. Schipper, and W. E. Van Nostrand. 1997. Rapid degeneration of cultured human brain pericytes by amyloid  $\beta$  protein. *J. Neurochem.* 68:1135–1141.

Walsh, D. M., I. Klyubin, J. V. Fadeeva, W. K. Cullen, R. Anwyl, M. S. Wolfe, M. J. Rowan, and D. J. Selkoe. 2002. Naturally secreted oligomers of amyloid  $\beta$  protein potently inhibit hippocampal long-term potentiation in vivo. *Nature*. 416:535–539.

Wattendorff, A. R., B. Frangione, W. Luyendijk, and G. T. A. M. Bots. 1995. Hereditary cerebral haemorrhage with amyloidosis, Dutch type (HCHWA-D): clinicopathological studies. *J. Neurol. Neurosurg. Psychiatry*. 698:699–706.

Wurth, C., N. K. Guimard, and M. H. Hecht. 2002. Mutations that reduce aggregation of the Alzheimer's A $\beta$ 42 peptide: an unbiased search for the sequence determinants of A $\beta$  amyloidogenesis. *J. Mol. Biol.* 319:1279–1290.

## APPENDIX D

Dr. David Mobley's dissertation includes chapter versions of the articles appearing in Apps. **B,C** as well as an extensive review of prion proteins and disease in its introductory chapter. Dr. Mobley graduated in June 2004 and is now a postdoctoral researcher in the group of Prof. Ken Dill at UC San Francisco. The entire dissertation is too large to attach to the present document, but is available for downloading at

<http://sexton.ucdavis.edu/CondMatt/cox/mobleydissertation.pdf>

# Structure of infectious prions: stabilization by domain swapping

Sichun Yang,\* Herbert Levine,\* José N. Onuchic,\* and Daniel L. Cox\*,†,1

\*Center for Theoretical Biological Physics, University of California San Diego, La Jolla, California, USA; and †Department of Physics, University of California, Davis, California, USA

**ABSTRACT** A candidate structure for the minimal prion infectious unit is a recently discovered protein oligomer modeled as a  $\beta$ -helical prion trimer (BPT); BPTs can stack to form cross- $\beta$  fibrils and may provide insight into protein aggregates of other amyloid diseases. However, the BPT lacks a clear intermonomer binding mechanism. Here we propose an alternative domain-swapped trimeric prion (DSTP) model and show with molecular dynamics (MD) that the DSTP has more favorable intermonomer hydrogen bonding and proline dihedral strain energy than the BPT. This new structural proposal may be tested by lysine and N terminus fluorescent resonance energy transfer (FRET) either directly on recombinant prion protein amyloid aggregates or on synthetic constructs that contain the proline/lysine-rich hinge region critical for domains to swap. In addition, the domain swapping may provide 1) intrinsic entanglement, which can contribute to the remarkable temperature stability of the infectious prion structure and help explain the absence of PrP<sup>Sc</sup> monomers, 2) insight into why specific prolines are potentially relevant to three inherited forms of prion disease, and 3) a simple explanation of prion strains assuming the strain is encoded in the monomer number of the oligomers.—Yang, S., Levine, H., Onuchic, J. N., Cox, D. L. Structure of infectious prions: stabilization by domain swapping. *FASEB J.* 19, 1778–1782 (2005)

**Key Words:** prion • domain swapping •  $\beta$ -helix • amyloid

## MODEL $\beta$ -HELICAL PRION TRIMER

THE PROTEIN-ONLY MODEL for prion diseases remains the leading candidate to explain the infectious form of the disease (1), and this has been significantly strengthened by the successful production of disease from synthetic prion protein aggregates (2). Clearly, the understanding of prion disease pathology, propagation within the body, and therapeutic approaches will be greatly enhanced by a detailed knowledge of the structure of the minimal infectious protein unit.

The discovery of areal aggregates of infectious prion protein oligomers in purified brain extracts from mice has inspired a leading candidate model for the minimal infectious unit, a trimer in which large portions of the N terminus are converted to left-handed  $\beta$ -helices (3,

4). We call this the  $\beta$ -helical prion trimer (BPT) model. Figure 1A shows a top view of the BPT in the  $\beta$ -helical region. This BPT displays a 3-fold symmetry consistent with maps of the electron density difference between the PrP 27-30 oligomers and the “miniprion” PrP<sup>Sc</sup>106 oligomers. The BPT can easily be stacked to form filaments, which can then be wound into amyloid fibrils. The model trimer also shares detailed structural features with the bacterial protein carbonic anhydrase trimer (5). Inspired in part by this model, others have explored the possibility that the  $\beta$ -helix plays a role in other amyloid structures such as aggregates of polyglutamine peptides (6),  $\beta$ -amyloid peptides (7), and yeast prion-like proteins (8).

However, it is not clear in the BPT model what holds the trimer together. The carbonic anhydrase trimer, which was the template for the BPT model is in fact held together by intermonomeric covalent bonding of zinc ions (5), which are not present in PrP<sup>Sc</sup>. It was suggested that a hydrogen bonding network is responsible for this binding (4), as in the case of the bacterial  $\beta$ -helical trimer serine acyltransferase (SAT) (9), but no effort was made to test this idea quantitatively. Moreover, the yellow loops of the BPT model (which are highly conserved (10)) shown in Fig. 1A, B and expanded in Fig. 1C contain two prolines, and prolines tend to disfavor this type of bending.

## HYPOTHESIS: A DOMAIN-SWAPPED PRION TRIMER IS THE MINIMAL INFECTIOUS UNIT

We hypothesize that a stable oligomeric structure for the infectious prion is the domain-swapped trimeric prion (DSTP) of Fig. 1B, which can increase hydrogen bonding and reduce elastic energy relative to the BPT structure proposed earlier. Further, we conjecture that the DSTP structure may be relevant to 1) the unusual temperature stability of the prion protein and the lack of observation of PrP<sup>Sc</sup> monomers (both due to the entanglement of the DSTP structure), 2) the kinetics of at least three inherited forms of human prion disease, and 3) the encoding of prion strains in conformation.

<sup>1</sup> Correspondence: CTBP, UC San Diego, MC 0374, 9500 Gilman Dr., La Jolla, CA 92093-0374, USA. E-mail: cox@physics.ucdavis.edu  
doi: 10.1096/fj.05-4067hyp

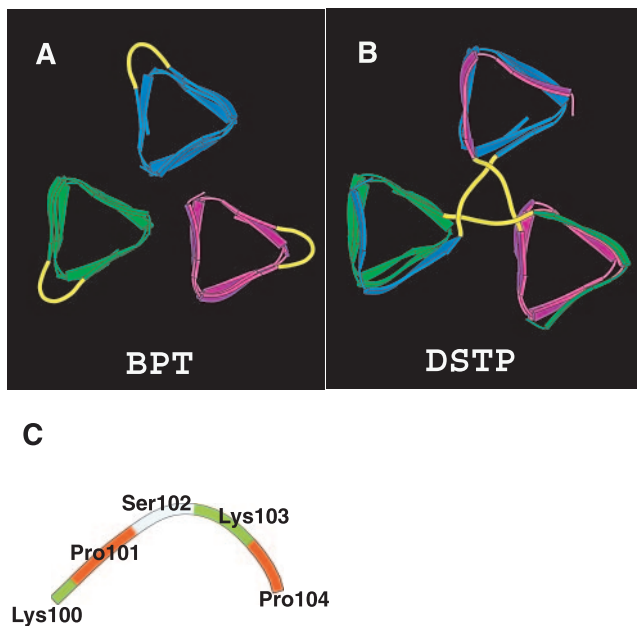


**Figure 1.** *A)* Proposed  $\beta$ -helical structure of the truncated PrP<sup>Sc</sup>106 prion trimer (BPT) taken from ref 4 (residues G89-F140). *B)* Structural model of domain-swapped trimeric prion (DSTP) of the present paper. *C)* The proposed hinge region expanded from the yellow loops in panels *A. B.*

## DOMAIN SWAPPING: MOTIVATION AND RESULTS

Concern with stability of the BPT model led us to modify it by domain swapping (11–13), especially since prolines are present in the hinge or bridging regions of several proteins that domain swap (14). For example, in p13suc1, the strain on two prolines in the hinge modulates the equilibrium between monomers and domain-swapped dimers (15, 16).

We constructed our DSTP model of Fig. 1*B* from the proposed BPT structure (we thank C. Govaerts for providing his coordinate file) by reorienting the monomers to place the loop regions near the trimer center and swapping residues 89–99 to a neighboring  $\beta$ -helix in a cyclical fashion, with the BPT loops serving as hinges. This DSTP model straightens these loops, adds more possible hydrogen bonds in the loop region, and preserves the putative monomer-monomer spacing and 3-fold symmetry of the electron density maps (3). We ran all-atom, explicit solvent MD (see Appendix for details) on energy minimized DSTP and BPT structures using AMBER8 (<http://amber.scripps.edu>). As a control, we applied the same protocol to the serine acyltransferase (SAT)  $\beta$ -helical trimer, which has no strained prolines and for which there is direct crystallographic evidence for intermonomer hydrogen bond-mediated cohesion (9). We also carried out two other simulation tests: *1)* we examined the stability of the DSTP model with the inclusion of the C terminus  $\alpha$ -helices proposed in ref 4, and *2)* we carried out three distinct 1-ns runs for both the BPT and DSTP structures to make sure there is no special circumstance with regard to individual simulations.

We have concluded that the DSTP is significantly more stable than the BPT and therefore a more promising candidate structure. First, we have enumerated direct and water-bridged hydrogen bonds between monomers in the BPT model, our DSTP model, and the SAT structure (see Appendix), and carried this out for three separate MD runs on each structure. We show the direct hydrogen bond counts for three different 1-ns runs of the BPT and DSTP structures in Fig. 2. For the BPT, we find  $2 \pm 1$ ,  $5 \pm 1$ , and  $2 \pm 1$  direct hydrogen bonds for the three runs (averages over the last 100-ps of simulation time), and at the last simulation time 0, 0, and 1 water-mediated hydrogen bonds. For the DSTP, we find for all three runs  $9 \pm 1$  direct hydrogen bonds for the last 100-ps of simulation time and 2, 1, and 1 water-mediated hydrogen bonds in the last simulation snapshot. In the one BPT case with a relatively high number of direct hydrogen bonds, the N terminus from one monomer has contacted with the N terminus region of another. In general, the BPT hydrogen bonds form around Q89 only, while the DSTP hydrogen bonds form in the hinge region. Note that Fig. 2 shows direct hydrogen bonds formed in the monomer-monomer interface for the DSTP to generically increase with time while those from the BPT generically decrease with MD time. In contrast to the BPT, the simulated  $\beta$ -helical portion (F140-A237) of the SAT trimer has 11 direct and 3 water-bridged hydrogen bonds (after two stage equilibration with no restraints).

Second, we remark that the domain swapping also relaxes the P101 and P104 dihedral energy by  $\sim 1.0$  kcal/mol after 1-ns of MD. Hence, the domain swapping helps relieve elastic strain as anticipated.

Third, we have verified that the DSTP structure for the PrP<sup>Sc</sup>106 can accommodate the C terminus  $\alpha$ -helices without affecting stability. This is a nontrivial point, since a rigid rotation of the monomers within the BPT is not possible due to steric constraints. As shown in Fig. 3, we find that by “peeling off” one triangular edge (residues 133–140) of the lower (C terminus) end of each  $\beta$ -helix to form a random coil segment that we can link to the  $\alpha$ -helices that begin at residue 177, with no resultant change in direct hydrogen bonding structure.

Finally, high temperature MD provides direct evidence for BPT instability; at 500K, the DSTP remains

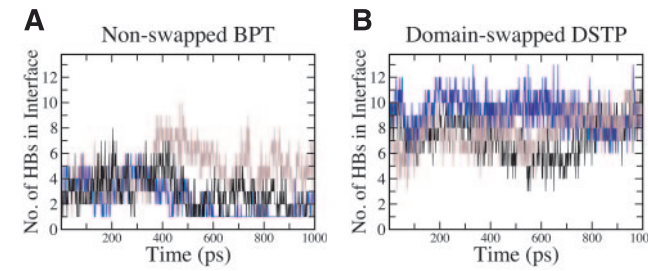


**Figure 2.** MD simulations show that the nonswapped BPT (*A*) has less direct hydrogen bonds in the interface region than the domain-swapped DSTP (*B*). In both cases we have simulated residues G89-F140. Different colors correspond to three different 1 ns MD runs in each case initialized at different initial temperatures (see Appendix).

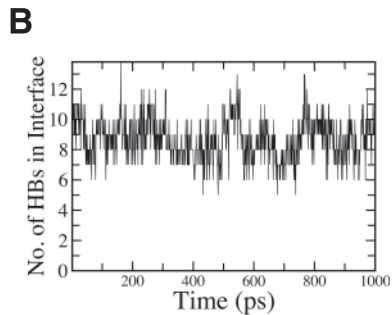
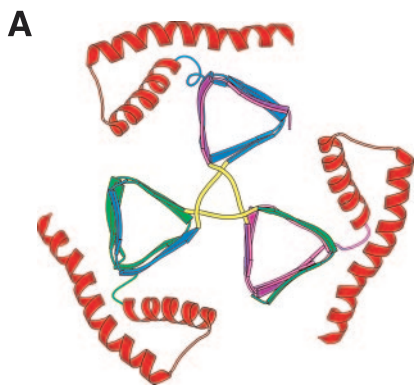


**Figure 3.** A) Model for DSTP  $\text{PrP}^{\text{Sc}}106$  (with residues G141-H176 deleted) and  $\alpha$ -helices included. Residues 133-140 have been removed from the lower rung of the  $\beta$ -helices for each monomer, converted to random coil, and attached to residue 177 of the  $\alpha$ -helices. B) Number of direct hydrogen bonds for the DSTP structure with intact  $\alpha$ -helices. The  $\alpha$ -helices have no effect on the stabilization induced by the domain swapping.

compact and entangled, while the BPT monomer-monomer separation nearly doubles. Principal component analysis, which identifies the amplitude and character of the dominant fluctuations, shows similar BPT unbinding tendencies at 300K as in the 500K simulation, but no unbinding tendencies for the DSTP. **Figure 4** shows the radius of gyration in the 500K runs as a function of simulation time. Within the 1-ns window of simulation, the BPT radius appears to keep growing, reaching about twice that of the apparently more stable DSTP structure. This stabilization through entanglement may be relevant to the unusual temperature stability of infectious prion proteins, although we cannot rule out that such stabilization is related to larger scale aggregates of prion oligomers. The entanglement may also be relevant to the inability to isolate monomeric forms of  $\text{PrP}^{\text{Sc}}$ , since the scrapies form is stabilized in this picture only in aggregate.

#### POSSIBLE RELEVANCE TO INHERITED DISEASES AND PRION STRAINS

Finally, we discuss the possible relevance of the DSTP model to inherited diseases and strains. First, proline point mutations yield heritable Creutzfeldt-Jakob disease (P105T for humans, P104T for mice) or Gerstmann-Sträussler-Scheinker disease (P102L, P105L for

humans, P101L, P104L for mice; see chapter 14, ref 1). Transgenic mice with P101I have even greater disease susceptibility whereas those with P101Y have somewhat less susceptibility than P101L (K. Nazor and G. Telling, private communication). We note that the centrality of these sites in the DSTP hinges affords possible burial of the relatively hydrophobic I, L, T, and Y side chains and a potential speed up of trimer formation through increased hinge flexibility. Moreover, the insertion of relatively hydrophobic residues into the unstructured region of the normal  $\text{PrP}^{\text{C}}$  protein will raise the energy of this structure. Indeed, it is already known that the P102L mutation is marginally less stable than the wild-type protein (see p. 694, ref 1). A decrease in the stability of the cellular protein form relative to wild-type monomers coupled to an increase in stability of the scrapies form (associated with more effective hydrophobic burial of the mutant residue) should lead to more rapid conversion kinetics via ramping of the overall free energy surface slope in favor of the scrapies form.

In **Fig. 5** we illustrate two ways in which strains might breed true if the monomer content within an oligomer encodes the strain information. With this assumption, strains can breed true either by 1) oligomer conversion and crystallization on membranes (Fig. 5A), with local shape matching favoring homogeneous growth in a manner analogous to the oriented aggregation of nanoparticles (17), or 2) via interneuronal, epitaxially templated conversion across the synaptic cleft or interneuronal gaps (Fig. 5B). The plausibility of the latter conjecture rests on the length of unstructured N terminus  $\text{PrP}^{\text{C}}$ , which is  $\sim 100$  residues, or  $\sim 30$  nm stretched out, easily sufficient to span the interneuronal gaps of 10–20 nm. Both of these models would enjoy enhanced conversion kinetics in the presence of unconverted or “soft” oligomers of  $\text{PrP}^{\text{C}}$  (18); the interneuronal mechanism in this case would allow for exponential growth via oligomeric autocatalytic conversion. We note that a different domain swapping model

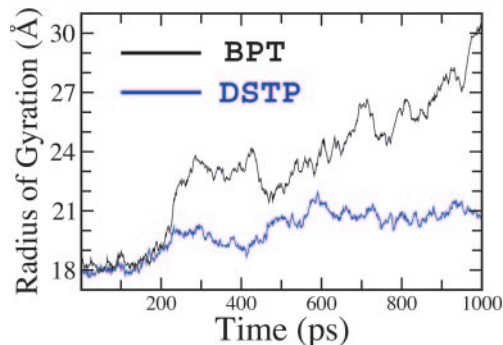
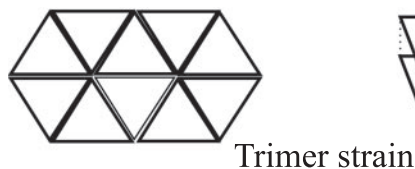


**Figure 4.** The entanglement due to domain swapping introduces additional stability for the DSTP relative to the BPT as revealed by high temperature ( $T=500\text{K}$ ) simulations, where the radius of gyration of the BPT increases more rapidly than that of the DSTP, which reflects unbinding of the BPT. Principal component analysis at 300K reveals a similar unbinding tendency.

## A Intraneuronal templating



## B Interneuronal templating

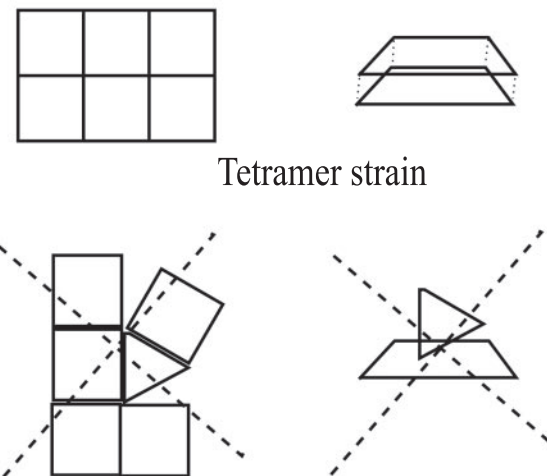


**Figure 5.** Schematic models for strains breeding true under the assumption that strain is encoded in monomer number. For simplicity, we assume one strain is encoded as trimers, one as tetramers. A) Areal aggregation. Given local size or orientation mismatches between trimers (upper image) and tetramers (lower image), energetics will, for example, disfavor growth of trimers off of tetramer seeds (lower image). B) Interneuronal templating. Assuming that seeds template conversion across interneuronal gaps or the synaptic cleft, trimers will seed trimer growth (upper image), tetramers will seed tetramer growth (middle image), and there will be no cross-seeding between trimers and tetramers.

for strains has been conjectured previously (19); separately, domain-swapped prion dimers have been crystallized (20). The latter result is consistent with prion oligomerization via intermolecular disulfide bonding as has been shown by redox induced prion fibrillization *in vitro* (21), although only intramolecular disulfide bonding has so far been observed *in vivo* (22). Other specific domain swapping mechanisms than those we have discussed here may play a critical role in amyloid fibril formation for prions as has been observed for other proteins (24–26). For the PrP 27-30 scrapies form, the large loop (residues E145-R163) of ref 4 made from some of the deleted residues of the PrP<sup>Sc</sup>106 structure could serve as a hinge region for alternative domain-swapped structures.

## PROPOSED EXPERIMENTAL TESTS

While the DSTP structure may ultimately be testable directly on recombinant infectious prion oligomers, as

have been synthesized by Prusiner and collaborators recently (2), we first propose testing an analog system by FRET labeling. Poly-Q peptides are of considerable interest because of the polyglutamine diseases (especially Huntington's). The “critical” length near 36 glutamine repeats for disease is suggestive of a left-handed  $\beta$ -helix structure, as discussed elsewhere (4, 6, 27). The key experiment we propose is to construct synthetic peptides of the form Q12(KPSPK)Q<sub>m</sub>, where  $m = 24–36$ . The goal is to label the N terminus Q's in half the peptides with a donor, the K's with a different donor, and in the other half put in N terminus Q acceptors and K acceptors. If the argument about stress relaxation and hydrogen bond stabilization works for the prion, it should also work here. There should be intense K-K FRET given intermonomer separations of the side chains by  $\sim 4 \text{ \AA}$  if the domain swapping arises. There will also be weak N terminus-Q- N terminus-Q FRET. Presumably there could be an N terminus-Q-to-N terminus-Q FRET signal arising with time if the trimers are first formed and then they fibrillize, since the corresponding distances would get reduced by  $\sim 60\%$  case assuming stacking of the  $\beta$ -helices. If this works on the synthetic peptide it should be attempted on recombinant prion protein prior to *in vitro* aggregation as per ref 2. We would anticipate little interfering contributions from other lysines in the prion protein sequence that are far from the hinge region.

## SUMMARY

We propose a domain-swapped trimer model for the minimal infectious prion oligomer, and note that the domain swapping stabilizes the oligomer relative to the earlier proposed model by reducing stress in proline containing loops, increasing intermonomer hydrogen bonding, and promoting entanglement. We conjecture that domain swapping may play a role in explaining the temperature stability of the scrapies form of the prion protein, the absence of PrP<sup>Sc</sup> monomers, inherited prion disease phenotypes associated with mutating prolines in hinges of the DSTP, and that conformation may be encoded in the monomer number in a given oligomer. Finally, we propose experimental tests based on FRET labeling of principally lysine residues near the crucial prolines, which should produce intense FRET response if the domain swapping is present. FJ

## Appendix

The simulations were carried out with the AMBER8 molecular dynamics package (28) with the AMBER parm99 force field and explicit TIP3P waters, following these procedures. 1) Before we start a molecular dynamics simulation, we perform an energy minimization of 2000 steps to partially relax the entire molecular system. 2) We perform a two-stage equilibration to further relax the protein and the surrounding solvent. In the first stage, we start the system from a low temperature

of approximately 100K and gradually heat up to 300K over 20-ps of simulation time. We perform this stage of equilibration with the volume held constant. In the second stage, we equilibrate the system using pressure and temperature control to adjust the density of water to experimental values. We have equilibrated the system for a total of 40-ps. During the first two steps, the backbone heavy atoms of the  $\beta$ -helical (and also the  $\alpha$ -helical if applicable) portions are positionally restrained using a harmonic potential. The hinge loops and the regions linking the  $\beta$ -helical and  $\alpha$ -helical domains are allowed to freely move. To achieve the three different MD runs for the BPT and DSTP structures, we start with different initial temperatures that seed a different run through a different initial thermal distribution of atom velocities. Finally, we carry out a 1-ns production run at constant pressure and temperature with no positional restraints. For the high temperature ( $T=500$ K) simulations, the production runs are performed at constant volume with a reduced time step of integration to prevent any possible system blowup.

Hydrogen bonds are calculated based on the following criteria: 1) direct hydrogen bonds in interface are counted with a donor-acceptor distance of 3.5 Å and a hydrogen-donor-acceptor angle of 60°, and 2) water-bridged hydrogen bonding in interface is counted if a water molecule couples by criterion 1) to an atom from each of two monomers.

D.L.C. thanks useful conversations with R. R. P. Singh and K. W. Plaxco; we also acknowledge fruitful discussions with P.G. Wolynes. This work was supported by the U.S. Army grant NP020132 and NSF Grants PHY0216576 and PHY0225630. Computing resources were supported by the San Diego Supercomputer Center and the NSF-sponsored Center for Theoretical Biological Physics.

## REFERENCES

- Prusiner, S. B. (2004) *Prion Biology and Diseases*, Cold Spring Harbor Press, Cold Spring Harbor, New York
- Legname, G., Baskakov, I. V., Nguyen, H. O., Riesner, D., Cohen, F. E., DeArmond, S. J., and Prusiner, S. B. (2004) Synthetic mammalian prions. *Science* **305**, 673–676; Castilla, J., Sa'a, P., Hetz, C., Soto, C. (2005) In vitro generation of infectious scrapie prions. *Cell* **121**, 195–206
- Wille, H., Michelitsch, M. D., Guenepaut, V., Supattone, S., Serban, A., Cohen, F. E., Agard, D. A., and Prusiner, S. B. (2002) Structural studies of the scrapie prion protein by electron crystallography. *Proc. Natl. Acad. Sci. USA* **99**, 3563–3568
- Govaerts, C., Wille, H., Prusiner, S. B., and Cohen, F. E. (2004) Evidence for assembly of prions with left-handed  $\beta$ -helices into trimers. *Proc. Natl. Acad. Sci. USA* **101**, 8342–8347
- Lindskog, S. (1997) Structure and mechanism of carbonic anhydrase. *Pharmacol. Ther.* **74**, 1–20
- Stork, M., Giese, A., Kretzschmar, H. A., and Tavan, P. (2005) Molecular dynamics simulations indicate a possible role of parallel  $\alpha$ -helices in seeded aggregation of poly-Gln. *Biophys. J.* **88**, 2442–2451
- Guo, J. T., Wetzel, R., and Wu, Y. (2004) Molecular modeling of the core of  $\text{A}\beta$  amyloid fibrils. *Proteins* **57**, 357–364
- Kishimoto, A., Hasegawa, K., Suzuki, H., Tauchi, H., Namba, K., and Yoshida, M. (2004)  $\alpha$ -helix is a likely core structure of yeast prion Sup35 amyloid fibers. *Biochem. Biophys. Res. Commun.* **315**, 739–745
- Pye, V. E., Tingey, A. P., Robson, R. L., and Moody, P. C. E. (2004) The structure and mechanism of serine acetyltransferase from *Escherichia coli*. *J. Biol. Chem.* **279**, 40729–40736
- Lysek, D. A., and Wuthrich, K. (2004) Prion protein interaction with the C-Terminal SH3 domain of Grb2 studied using NMR and optical spectroscopy. *Biochemistry* **43**, 10393–10399
- Bennett, M., Choe, S., and Eisenberg, D. (1994) Domain swapping: entangling alliances between proteins. *Proc. Natl. Acad. Sci. USA* **91**, 3127–3131
- Bennett, M. J., Schlunegger, M. P., and Eisenberg, D. (1995) 3D domain swapping: a mechanism for oligomer assembly. *Protein Sci.* **4**, 2455–2468
- Yang, S., Cho, S. S., Levy, Y., Cheung, M. S., Levine, H., Wolynes, P. G., and Onuchic, J. N. (2004) Domain swapping is a consequence of minimal frustration. *Proc. Natl. Acad. Sci. USA* **101**, 13786–13791
- Bergdoll, M., Remy, M.-H., Cagnon, C., Masson, J.-M., and Dumas, P. (1997) Proline-dependent oligomerization with arm exchange. *Structure* **5**, 391–401
- Rousseau, F., Schymkowitz, J. W. H., Wilkinson, H. R., and Itzhaki, L. S. (2001) Three-dimensional domain swapping in p13suc1 occurs in the unfolded state and is controlled by conserved proline residues. *Proc. Natl. Acad. Sci. USA* **98**, 5596–5601
- Rousseau, F., Schymkowitz, J. W. H., and Itzhaki, L. S. (2003) The unfolding story of three-dimensional domain swapping. *Structure* **11**, 243–251
- Sugimoto, T. (2003) Formation of monodispersed nano- and micro-particles controlled in size, shape, and internal structure. *Chem. Eng. Technol.* **26**, 313–321
- Mobley, D. L., Cox, D. L., Singh, R. R. P., Kulkarni, R. V., and Slepoy, A. (2003) Simulations of oligomeric intermediates in prion diseases. *Biophys. J.* **85**, 2213–2223
- Cohen, F. E., and Prusiner, S. B. (1998) Pathologic conformations of prion proteins. *Annu. Rev. Biochem.* **67**, 793–819
- Knaus, K. J., Morillas, M., Swietnicki, W., Malone, M., Surewicz, W. K., and Yee, V. C. (2001) Crystal structure of the human prion protein reveals a mechanism for oligomerization. *Nat. Struct. Biol.* **8**, 770–774
- Lee, S., and Eisenberg, D. (2003) Seeded conversion of recombinant prion protein to a disulfide-bonded oligomer by a reduction oxidation process. *Nat. Struct. Biol.* **10**, 725–730
- Welker, E., Raymond, L. D., Scheraga, H. A., and Caughey, B. (2002) Intramolecular versus intermolecular disulfide bonds in prion proteins. *J. Biol. Chem.* **277**, 33477–33481
- May, B.C.H., Govaerts, C., Prusiner, S.B., Cohen, F.E. (2004) Prions: so many fibers, so little infectivity. *Trends Biochem. Sci.* **29**, 162–165
- Liu, Y., Gotte, G., Libonati, M., and Eisenberg, D. (2001) A domain-swapped RNase A dimer with implications for amyloid formation. *Nat. Struct. Biol.* **8**, 211–214
- Janowski, R., Kozak, M., Jankowska, E., Grzonka, Z., Grubb, A., Abrahamson, M., and Jaskolski, M. (2001) Human cystatin C, an amyloidogenic protein, dimerizes through three-dimensional domain swapping. *Nat. Struct. Biol.* **8**, 316–320
- Sinha, N., Tsai, C.-J., and Nussinov, R. (2001) A proposed structural model for amyloid fibril elongation: domain swapping forms an interdigitating  $\beta$ -structure polymer. *Protein Eng.* **14**, 93–103
- Wetzel, R. (2002) Ideas of order for amyloid fibril structure. *Structure* **10**, 1031–1036
- Pearlman, D. A., Case, D. A., Caldwell, J. W., Ross, W. R., Cheatham, T. E., III, DeBolt, S., Ferguson, D., Seibel, G., and Kollman, P. (1995) AMBER, a computer program for applying molecular mechanics, normal mode analysis, molecular dynamics and free energy calculations to elucidate the structures and energies of molecules. *Comp. Phys. Commun.* **91**, 1–41

Received for publication April 1, 2005.  
Accepted for publication July 5, 2005.

## Prion Disease: Exponential Growth Requires Membrane Binding

Daniel L. Cox,\*† Rajiv R. P. Sing,\* and Sichun Yang†

\*Department of Physics, University of California, Davis, California 95616; and †Center for Theoretical Biological Physics, University of California, San Diego, La Jolla, California 92093

**ABSTRACT** A hallmark feature of prions, whether in mammals or yeast and fungi, is exponential growth associated with fission or autocatalysis of protein aggregates. We have employed a rigorous kinetic analysis to recent data from transgenic mice lacking a glycosylphosphatidylinositol membrane anchor to the normal cellular  $\text{PrP}^C$  protein, which show that toxicity requires the membrane binding. We find as well that the membrane is necessary for exponential growth of prion aggregates; without it, the kinetics is simply the quadratic-in-time growth characteristic of linear elongation as observed frequently in *in vitro* amyloid growth experiments with other proteins. This requires both: i), a substantial intercellular concentration of anchorless  $\text{PrP}^C$ , and ii), a concentration of small scrapies seeding aggregates from the inoculum, which remains relatively constant with time and exceeds the concentration of large polymeric aggregates. We also can explain via this analysis why mice heterozygous for the anchor-full/anchor-free  $\text{PrP}^C$  proteins have more rapid incubation than mice heterozygous for anchor-full/null  $\text{PrP}^C$ , and contrast the mammalian membrane associated fission or autocatalysis with the membrane free fission of yeast and fungal prions.

Received for publication 19 January 2006 and in final form 17 March 2006.

Address reprint requests and inquiries to D. L. Cox, E-mail: cox@physics.ucdavis.edu.

Prions are distinguished from other amyloid diseases both by their infectious character and the observed exponential growth of infectious material *in vivo* (1). There is a correspondence to this of prion-like proteins in yeast and fungi, for which spontaneous fission is reported *in vitro* (2). In fact, it has been argued that the replication necessary for infection in mammals and non-Mendelian inheritance in yeast/fungi requires the fission or autocatalysis that drives the exponential growth (1). It has been established for yeast prions that additional chaperone proteins most likely facilitate the fission of aggregates in living cells (1). It is an open question what mechanism drives the exponential growth in mammals. Here we show by a rigorous kinetic analysis of recent disease time course data that the exponential growth is tied to membrane anchoring of the prion protein, suggesting that either mechanical fission of areal prion aggregates or oligomeric autocatalysis of membrane bound prions explain the observed behavior.

Chesebro et al. (3) recently studied transgenic (Tg) mice lacking a GPI membrane anchor to the normal cellular  $\text{PrP}^C$  protein and discovered that these mice grew infectious prions without suffering neuronal death. We denote these anchorless cellular prions as  $\text{PrP}_{\text{Tg}}^C$ , and anchor-full wild-type (WT) cellular prions by  $\text{PrP}_{\text{WT}}^C$ . When inoculated with infectious scrapies prions ( $\text{PrP}^{\text{Sc}}$ ) at a dose that induces clinical symptoms within 140–160 days for WT mice, the Tg mice were symptomless up to 400–600 days, even though proteinase resistant  $\text{PrP}$ -res, an indicator of infectivity, accumulated and surpassed the maximal WT levels.

In Fig. 1 the Tg mice  $\text{PrP}$ -res concentration (*crosses*) of Chesebro et al. (3) are plotted versus the square of time, together with a linear regression fit (*line*) with a high regression

coefficient ( $R = 0.97$ ). This time dependence is consistent with short time kinetics described by linear polymer elongation via monomer addition without fission or autocatalysis (4), illustrated schematically in Fig. 2. Assuming the  $\text{PrP}$ -res concentration to be a proxy for the total protein content in aggregate, simple kinetic arguments predict a behavior, before monomer depletion and seed nucleus depletion, of

$$[\text{PrP-res}](t) \propto (1/2)(p + [\text{PrP}_{\text{Tg}}^C])^2 [\text{PrP}_n^{\text{Sc}}] t^2, \quad (1)$$

with  $p + [\text{PrP}_{\text{Tg}}^C]$  the elongation rate at intercellular monomer Tg prion concentration  $[\text{PrP}_{\text{Tg}}^C]$ , and  $[\text{PrP}_n^{\text{Sc}}]$  is the intercellular concentration of seeding nuclei from inoculated scrapies protein after initial hydrodynamic clearance. The validity of Eq. 1 at long times suggests that: i), there is a substantial homeostatic concentration of intercellular  $\text{PrP}_{\text{Tg}}^C$  presumably due to slow clearance, and ii),  $[\text{PrP}_n^{\text{Sc}}]$  is hardly changed implying either that only a small fraction of seeds grow into large polymers or  $[\text{PrP}_n^{\text{Sc}}]$  is maintained by steady proteolytic degradation of large remnant aggregates from the dose. Given a similar *de novo* production rate of  $\text{PrP}_{\text{WT}}^C$  in inoculated WT mice, we speculate that the associated saturation of  $[\text{PrP-res}]$  arises from loss of  $\text{PrP}_{\text{WT}}^C$  after cell death.

This elongation hypothesis is testable by: i), genetically engineering mice to overexpress  $\text{PrP}_{\text{Tg}}^C$ , which will quadratically modulate the  $\text{PrP}$ -res concentration (4), and ii), by varying the initial dose of  $\text{PrP}^{\text{Sc}}$ , which will linearly modulate the  $\text{PrP}$ -res concentration.

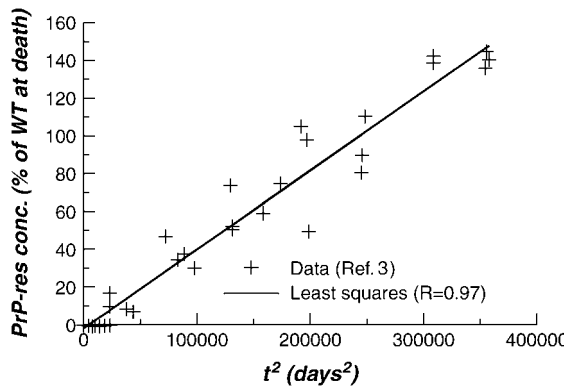


**FIGURE 1** Quadratic-in-time fit to infectious prion time course data of Chesebro et al. (3).

Another striking observation of Chesebro et al. (3) was that mice heterozygous for expression of  $\text{PrP}_{\text{WT}}^{\text{C}}$  and  $\text{PrP}_{\text{Tg}}^{\text{C}}$  display shorter incubation time upon inoculation than mice with one  $\text{PrP}_{\text{WT}}^{\text{C}}$  copy and one inactive fusion construct. We argue that this is due to an enhanced concentration for  $\text{PrP}_{\text{Tg}}^{\text{C}}$  relative to  $\text{PrP}_{\text{WT}}^{\text{C}}$  and that PrP-res obtained from  $\text{PrP}_{\text{Tg}}^{\text{C}}$  also templates  $\text{PrP}_{\text{WT}}^{\text{C}}$  conversion. The latter is speculative but should be testable.

To establish the expectation that the  $\text{PrP}_{\text{WT}}^{\text{C}}$  concentration is lower than  $\text{PrP}_{\text{Tg}}^{\text{C}}$  in the WT/Tg heterozygotes, it is sufficient to establish that  $\text{PrP}_{\text{WT}}^{\text{C}}$  concentration in WT mice is lower than  $\text{PrP}_{\text{Tg}}^{\text{C}}$  concentration in the anchorless Tg mice. To make this clear, we compare estimates for cellular prion concentrations in homozygous WT mice with homozygous Tg mice. Before the postulated cell-death driven saturation of infectious material, WT mice inoculated with a concentration  $[\text{PrP}_n^{\text{Sc}}]$  of scrapies seeds will have a time course of the general form (4)

$$[\text{PrP-res}](t) \propto A_+ (\cosh[\lambda t] - 1), \quad (2)$$

where  $\lambda = \ln(2)/t_2$  is the percentage growth rate and  $t_2$  is the doubling time. The coefficient  $A_+$  can be determined from

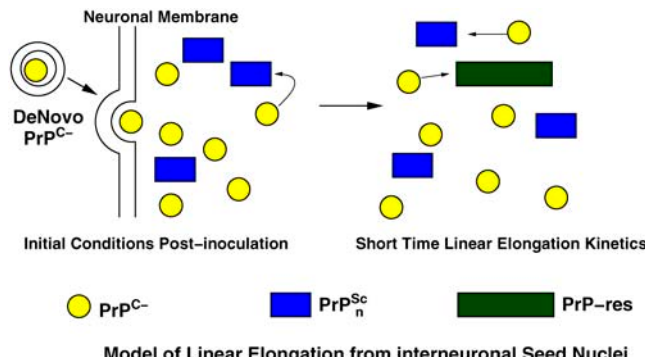


**FIGURE 2** Schematic model for linear elongation driven growth of infectious prion material from inoculated seeds and anchorless cellular prion proteins.

the short time behavior of Eq. 2, which, like Eq. 1, is described by linear elongation given by

$$1/2 A_+ (\lambda t)^2 = 1/2 (p_+ [\text{PrP}_{\text{WT}}^{\text{C}}])^2 [\text{PrP}_n^{\text{Sc}}] t^2, \quad (3)$$

where  $[\text{PrP}_{\text{WT}}^{\text{C}}]$  is the homeostatic concentration of membrane bound WT PrP<sup>C</sup> and we have assumed that the WT and Tg mice have the same PrP-res elongation coefficient  $p_+$ .

On the other hand, at long times (but before saturation) Eq. 2 gives

$$[\text{PrP-res}](t) \propto 1/2 A_+ \exp(\lambda t). \quad (4)$$

Now, we set  $t_+ = N_d^+ t_2$  as the time it takes WT mice to reach clinically detectable levels of PrP-res concentration at the inoculum level generating a seed nuclei concentration  $[\text{PrP}_n^{\text{Sc}}]$ , where  $N_d^+$  is the number of doublings experienced in that process, and  $t_-$  is the time it takes Tg mice to reach the same clinical concentration of PrP-res for the same initial inoculation dose. By taking suitable ratios to eliminate  $A_+$ ,  $[\text{PrP}_n^{\text{Sc}}]$ , and  $p_+$ , the ratio of homeostatic concentrations of cellular prions from the WT mice to the Tg mice is given by

$$[\text{PrP}_{\text{WT}}^{\text{C}}]/[\text{PrP}_{\text{Tg}}^{\text{C}}] = (1/2) \ln(2) N_d^+ (t_-/t_+) \times \exp(-\ln(2)(N_d^+ / 2)). \quad (5)$$

From Chesebro et al. (3),  $t_+ = 150$  days, and  $t_- = 400$  days. A reasonable estimate (5) for the number of doublings is  $N_d^+ = 20$  for the dose of Chien et al. (1). With these numbers, Eq. 5 gives a concentration ratio (and hence elongation rate ratio) for WT/Tg mice of 0.036. This is reasonable given that likely slower PrP<sup>C</sup> clearance in the Tg case will lead to a higher extracellular concentration of cellular prion protein. By employing the arguments of Chien et al. (1) we obtain elongation rate values of 0.13/day(Wt) and 3.5/day (Tg). The former is in good agreement with estimates made elsewhere for linear elongation based upon analysis of dose-incubation curves (6).

Hence, in the WT/Tg and WT/null heterozygotes explored in Chesebro et al. (3), we anticipate in each case the membrane bound  $\text{PrP}_{\text{WT}}^{\text{C}}$  concentration to be about half that of the homozygous WT mice, whereas the intercellular  $\text{PrP}_{\text{Tg}}^{\text{C}}$  concentration should be about half that of the homozygous Tg mice. Because, as shown with infectious prions bound to electrodes (7), templating and conversion can be driven by scrapies material not bound to the membrane surface, we expect the incubation time of the WT/Tg heterozygotes to be significantly accelerated relative to the WT/null heterozygotes as is observed.

We note that membrane associated exponential growth might be due to: i), as yet undiscovered membrane specific enzymes splitting aggregates, in analogy to the role of Hp104a for yeast prions (1); ii), mechanical breakage of aggregates due to membrane curvature or membrane undulations (8); iii), oligomeric autocatalysis arising from interneuronal

templating by infectious oligomeric seeds bound to one or the other membrane (9).

## ACKNOWLEDGMENTS

We are grateful for conversations with H. Levine, J. N. Onuchic, M. Oldstone, A. N. Parikh, and J. Weissman.

We acknowledge the support of the U.S. Army (Congressionally Directed Medical Research Program, grant NP020132) (D.L.C. and R.P.P.S.), National Science Foundation grant PHY0216576 (D.L.C. and S.Y.), and the J. S. Guggenheim Memorial Foundation (D.L.C.).

## REFERENCES and FOOTNOTES

1. Chien, P., J. S. Weissman, and A. H. DePace. 2004. Emerging principles of conformation based prion inheritance. *Annu. Rev. Biochem.* 73: 617–656.
2. Collins, S. R., A. Douglass, R. Vale, and J. S. Weissman. 2004. Mechanism of prion propagation: amyloid growth occurs by monomer addition. *PLoS Biol.* 2:10–18.
3. Chesebro, B., M. Trifilo, R. Race, K. Meade-White, C. Teng, R. LaCasse, L. Raymond, C. Favara, G. Baron, S. Priola, B. Caughey, E. Masliah, and M. Oldstone. 2005. Anchorless prion protein results in infectious amyloid disease without clinical scrapie. *Science.* 308:1435–1439.
4. Ferrone, F. A. 1999. Analysis of protein aggregation kinetics. *Methods Enzymol.* 309:256–274.
5. Carlson, G. A., C. Ebeling, S. L. Yang, G. Telling, M. Torchia, D. Groth, D. Westaway, S. J. DeArmond, and S. B. Prusiner. 1994. Prion isolate specified allotypic interactions between the cellular and scrapie prion proteins in congenic and transgenic mice. *Proc. Natl. Acad. Sci. USA.* 91:5690–5694.
6. Kulkarni, R. V., A. Slepoy, R. R. P. Singh, D. L. Cox, and F. Pazmandi. 2003. Theoretical modeling of prion disease incubation. *Biophys. J.* 85:707–718.
7. Flechsig, E., I. Hegyi, M. Enari, P. Schwarz, J. Collinge, and C. Weissmann. 2001. Transmission of scrapie by steel-surface-bound prions. *Mol. Med.* 7:679–684.
8. Slepoy, A., R. R. P. Singh, F. Pazmandi, R. V. Kulkarni, and D. L. Cox. 2001. Statistical mechanics of prion disease. *Phys. Rev. Lett.* 87:058101.
9. Yang, S. C., H. Levine, J. N. Onuchic, and D. L. Cox. 2005. Structure of infectious prions: stabilization by domain swapping. *FASEB J.* 19: 1778–1782.

This un-edited manuscript has been accepted for publication in Biophysical Journal and is freely available on BioFast at <http://www.biophysj.org>. The final copyedited version of the paper may be found at <http://www.biophysj.org>.

## A mechanism for copper inhibition of infectious prion conversion

Daniel L. Cox, Jianping Pan, and Rajiv R.P. Singh

Department of Physics, University of California, Davis, 1 Shields Avenue, Davis, CA 95616

**ABSTRACT** We employ *ab initio* electronic structure calculations to obtain two structural models for copper bound in the strongest binding site of the noninfectious form of the prion protein. The models are compatible with available experimental constraints from electron spin resonance data. The bending of the peptide backbone attendant with the copper binding is not compatible with the requisite straight beta-strand backbone structure for the same sequence contained in two recently proposed models of the prion protein structure in its infectious form. We hypothesize that copper binding at this site is protective against conversion to the infectious form, discuss experimental data which appear to support and conflict with our hypothesis, and propose tests using recombinant prion protein, genetically modified cultured neurons, and transgenic mice.

Received for publication "Staff will complete" and in final form "Staff will complete"

Address reprint requests and inquiries to [cox@physics.ucdavis.edu](mailto:cox@physics.ucdavis.edu)

The functional role of the normal cellular prion protein ( $\text{PrP}^C$ ) may well be related to copper binding, potentially protecting against oxidative damage in the synaptic region by sequestering divalent copper<sup>1</sup>. This suggestion is supported by data for transgenic knockout mice devoid of the gene for expressing  $\text{PrP}^C$ ; these mice appear to suffer late stage oxidative degradation in the neuronal synaptic regions where surface bound prion protein is preferentially concentrated in wild type mice<sup>2,3</sup>. The strongest copper binding site is in the protein region which converts to beta sheet structure in the infectious ( $\text{PrP}^{\text{Sc}}$ ) form<sup>1</sup>. We use electronic structure calculations to study two possible geometries for the bound copper- $\text{PrP}^C$  complex; we find that these geometries are incompatible with recently proposed models<sup>4,5</sup> for  $\text{PrP}^{\text{Sc}}$  oligomers, and we thus hypothesize a mechanism for inhibition of  $\text{PrP}^C$ -to- $\text{PrP}^{\text{Sc}}$  conversion via copper binding.

Copper binds principally to mammalian  $\text{PrP}^C$  at octarepeat sites of highly conserved form (though not number) in a now well understood pyramidal geometry with binding to the peptide backbone, histidine side chains, and axial waters<sup>6</sup>. These octarepeats (residues 60-91 in humans) are not essential to  $\text{PrP}^{\text{Sc}}$ , which remains infectious even after proteinase exposure that leaves residues 92-230 intact. One strong copper binding site is present in the  $\text{PrP}^{\text{Sc}}$  core region, containing the sequence 92-96 GGGTH for humans. Electron spin resonance data suggest there is binding to the H96 (H95 in mice) side chain and the G94 amide group<sup>1</sup>. It is not known whether the primary peptide coordination is to four nitrogens

(NNNN) or to three nitrogens and an oxygen (NNON), although the former structure has been conjectured to be more likely<sup>1</sup>.

We have studied this problem computationally with the SIESTA local orbital based density functional theory code using conjugate gradient based energy minimization to examine possible GGGTH-Cu(II) geometries<sup>7,8</sup>. We have considered the NNNN structure and an NNON structure compatible with the ESR data<sup>1</sup> and our results are shown in the upper two panels of the figure for the mouse prion. We built initial candidate structures of the form  $\text{Ac-Cu}(\text{H}_2\text{O})_6(\text{GGGTH})-\text{NH}_2$  using ChemSite Pro (ChemSW, Fairfield CA) and VMD<sup>9</sup>. For each geometry, the lowest energy sampled provides our model bound copper-prion complex. We used double-zeta (DZ) basis sets for light atoms (H, C, N, O) and double-zeta polarized orbitals for copper. We used the Troullier-Martins norm-conserving pseudopotential. We employed the Perdew-Becke-Ernzerhof based generalized gradient approximation exchange correlation energy functional. Our energy cutoff for matrix element integration was 120 Rydberg. All calculations were carried out in a periodic unit cell size: 30.7 Å x 30.7 Å x 30.7 Å. Geometry minimization was carried out to a force tolerance of 32pN.

Our main result is inferred from comparing the two possible GGGTH-Cu(II) geometries to recently proposed  $\beta$ -helical  $\text{PrP}^{\text{Sc}}$  trimer models<sup>4,5</sup>. We see that the backbone bending induced by copper binding is not compatible with formation of  $\beta$ -strands in the left handed helices. (It is

unclear if another recently proposed model has the same characteristics<sup>10</sup>. ) Hence, copper in the non-octarepeat sequence GGGTH can protect against PrP<sup>C</sup>-to-PrP<sup>Sc</sup> conversion; removal of this copper by pH reduction associated with synaptic fluctuations or endocytosis may be a key step in the conversion pathway. This picture is supported by the observation that only the GGTH sequence is required for binding, and eutherian prion sequences reveal high conservation of either GGTH or the very similar GGSH sequence in the converting region<sup>11</sup>.

Removal of this copper by pH reduction may be a key step in the PrP<sup>C</sup>-to-PrP<sup>Sc</sup> conversion pathway since it is known that acidic conditions favor detachment of the copper<sup>12</sup>. We note two routes for such a pH reduction with accompanying conversion of PrP<sup>C</sup>. First, upon endocytosis into the cell, the pH is reduced. Assuming that some PrP<sup>Sc</sup> is endocytosed as well as PrP<sup>C</sup>, then conversion can take place within the endocytosed compartments after the copper is expelled. Second, given that PrP<sup>C</sup> is preferentially concentrated near the synapse, then from signal bearing vesicles released near or at the synapse<sup>13</sup> can reduce the pH locally and facilitate copper expulsion.

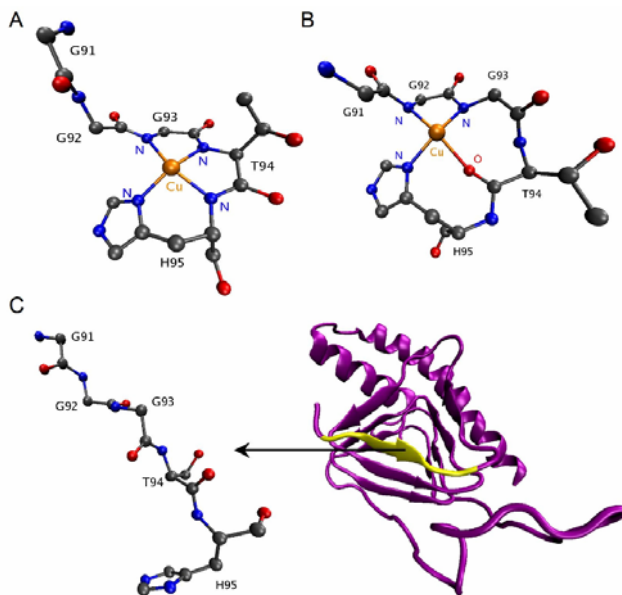


**Figure:** Potential copper binding motifs in the converting region of the normal (PrP<sup>C</sup>) mouse prion protein which are consistent with ESR data<sup>1</sup> are shown in panels (A,B). The corresponding copper free stretch of the left handed beta helix model of the infectious (PrP<sup>Sc</sup>) protein from Ref. (4) is shown in (C).

Three experimental results support our proposed mechanism indirectly: (1) Post-mortem studies show copper depletion in regions of infection, with 80-90%

reduction of copper content in the corresponding prion proteins<sup>14</sup>. This result is consistent with our mechanism, since this GGGTH binds Cu(II) first with potential cooperative enhancement of subsequent binding to other sites. If infection promotes removal of copper from this site, then it is more likely that copper will not be retained at the other sites assuming near-equilibrium conditions. (2) Copper uptake in infected cultured neurons is suppressed approximately 10 fold compared to control cells<sup>15</sup>. Again, this is consistent with the hypothesis, although this requires an understanding of how the prion, which is easily shown to contain less than 1% of cellular copper, can shutdown copper transport. (3) Copper in solution inhibits *in vitro* growth of amyloid fibrils<sup>16,17</sup>. This is a more direct corollary to our hypothesized protective role of copper.

Other experiments provide mixed support for our mechanism. The copper chelator D-penicillamine inoculated *in vivo* delays disease onset, which is at apparent odds with our hypothesis<sup>18</sup>. The chelator cuprizone, however, is known to induce a spongiosis (vacuolation of brain tissue) very similar to that of prion disease although it also induces demyelination of neurons and no transmissibility<sup>19,20</sup>. Moreover, it is also known that copper confers proteinase resistance to the cellular prion protein in the weaker binding octarepeat regions<sup>21</sup>. This is significant for two reasons. First, proteinase resistance is one of the generic hallmarks of the infectious form of the disease (although not all infectious prion protein is in fact proteinase resistant). Second, the octarepeat deletion does not remove infectivity from PrP<sup>Sc</sup>. However, in transgenic mice without octarepeats, disease incubation upon direct intracerebral inoculation is slowed<sup>22</sup>. Hence, these octarepeats are not necessary for disease, but (i) they can impart structure in the presence of copper that confers proteinase resistance to the prion protein, and (ii) their presence enhances disease incubation. Indeed, it is known that the octarepeat region adopts a unique structural motif when copper is bound<sup>23</sup>. We can rationalize these data by assuming the following affinity ranking: cuprizone > non-octarepeat site > D-PEN > octarepeat site. This ranking is plausible given the hexadentate chelation of cuprizone versus at most tetradentate coordination of D-PEN. With this assumption, D-PEN lifts the proteinase resistant structure associated with copper binding to octarepeats, and this slows conversion to the infectious form. These assumptions may be tested by performing competitive binding experiments *in vitro* with D-PEN<sup>18</sup>, cuprizone<sup>19</sup> and the relevant copper binding segments of the prion protein. We note that the high affinity of cuprizone for divalent copper apparently leads to stripping of copper from other proteins so that the *in vivo* phenomena need not be limited to prions; if our assumptions are correct, these

non-prion related effects must lead to more rapid degeneration of neurons than conversion to  $\text{PrP}^{\text{Sc}}$ .

To further test the mechanism, it is desirable to perform mutation studies on the stretch GGSH or GGTH. The key idea is to mutate out the H for, e.g., A,Y,G or other amino acids which should severely mitigate copper binding. We propose first that recombinant mutant  $\text{PrP}^{\text{C}}$  from residues 90-230 (with, e.g., H96A in the human form) be allowed to aggregate in copper-ful and copper-free environments. Using the reduced length prion will avoid the confounding effects from the octarepeat regions discussed above. If the mechanism is correct, the fibril formation rate should be approximately the same as wild type fibrils grown in copper free solutions. Second, one can transfet cultured neurons with the mutated DNA construct and look for increased susceptibility to infection. Third, assuming positive results from the fibril growth and cultured neuron experiments, transgenic mice with the H95 mutated away; these mice should prove to have shorter incubation times for a given dose than wild type mice. Finally, fibrillization experiments on recombinant marsupial  $\text{PrP}^{\text{C}}$  with and without copper should be informative since the H is replaced with Y<sup>24</sup>; our prediction based upon the present hypothesis would be that the copper should have reduced inhibition of fibril formation relative to growth of recombinant human prion protein.

## ACKNOWLEDGEMENTS

We acknowledge the support of the U.S. Army (Congressionally Directed Medical Research Program, grant NP020132), NSF Grant PHY0216576 for the Center for Theoretical Biological Physics (CTBP) of UC San Diego (D.L.C.), and the J.S. Guggenheim Memorial Foundation (D.L.C.). We are grateful for conversations with D. Kleinfeld, G.S. Millhauser, and A. Nordlund, and for correspondence with E.D. Britt and J. Graves. We thank the CTBP for use of their computers. We are grateful to C. Govaerts for sharing the coordinate file for his model of Ref. (4).

## REFERENCES AND ENDNOTES

1. Burns, C. S., et al., 2003. Copper coordination in the full-length, recombinant prion protein. *Biochem.* **42**: 6794-6803.
2. Klamt, F., et al., 2001. Imbalance of antioxidant defense in mice lacking cellular prion protein. *Free Rad. Biol. Med.* **30**: 1137-1144.
3. Sakudo, A., et al., 2004. Prion protein suppresses perturbation of cellular copper homeostasis under oxidative conditions. *Biochim. Biophys. Res. Comm.* **31**: 850-855.
4. Govaerts, C., H. Wille, S. B. Prusiner, & F. E. Cohen. 2004. Evidence for assembly of prions with left-handed  $\beta$ -helices into trimers. *Proc. Natl. Acad. Sci. U.S.A.* **90**: 8342-8347.
5. Yang, S., H. Levine, H. J.N. Onuchic, & D.L. Cox. 2005. Structure of infectious prions: stabilization by domain swapping. *FASEB* **19**: 1778-1782.
6. Burns, C.S., et al. 2002. Molecular features of the copper binding sites in the octarepeat domain of the prion protein. *Biochem.* **41**: 3991-4001.
7. Ordejon, P., E. Artacho, & J.M. Soler. 1996. Self-consistent order-N density-functional calculations for very large systems. *Physical Review B* **53**: 10441-10444.
8. Soler, J. M. et al. 2002. The SIESTA method for ab initio order-N materials simulation. *Journal of Physics-Condensed Matter* **14**: 2745-2779.
9. Humphrey, W., A. Dalke, & K. Schulten. 1996. VMD: Visual molecular dynamics. *J. Mol. Graph.* **14**: 33-38.
10. DeMarchi, M.L. and V. Daggett. 2004. From conversion to aggregation: Protofibril formation of the prion protein. *P. Nat. Acad. Sci. (USA)* **101**: 2293-2298.
11. Horn, F., G. Vriend, and F.E. Cohen. 2001. Collecting and Harvesting Biological Data: The GPCRDB & NucleaRDB Databases. *Nucleic Acids Res.* **29**: 346-349, and <http://www.receptors.org/Prion/>.
12. Aronoff-Spencer, E., et al.. 2000. Identification of the  $\text{Cu}^{2+}$  binding sites in the N-terminal domain of the prion protein by EPR and CD spectroscopy. *Biochem.* **39**: 13670-13771.
13. Chesler, M. 2003. Regulation and modulation of pH in the brain. *Physiol. Rev.* **83**: 1183-1221.
14. Wong, B.-S., et al.. 2001. Aberrant metal binding by prion protein in human prion disease. *J. Neurochem.* **78**: 1400-1408.
15. Rachidi, W., et al.. 2003. Prion infection impairs copper binding of cultured cells. *J. Biol. Chem.* **278**: 14595-14598.
16. Giese, A., J. Levin, U. Bertsch, & H. Kretzschmar. 2004. Effect of metal ions on de novo aggregation of full-length prion protein. *Biochem. Biophys. Res. Comm.* **320**: 1240-1246.
17. Bocharova, O. V., L. Breydo, V.V. Salnikov, & I. Baskakov. 2005. Copper(II) inhibits in vitro conversion of prion protein into amyloid fibrils. *Biochem.* **44**: 6776-6787.
18. Sigurdsson, E.M., et al.. 2003. Copper chelation delays the onset of prion disease. *J. Biol. Chem.* **278**: 46199-46202.
19. Pattison, I.H. & J.N. Jebbett. 1971. Histopathological similarities between scrapie and cuprizone toxicity in mice. *Nature* **230**: 115-117.
20. Pattison, I.H. & J.N. Jebbett. 1973. Clinical and histological recovery from the scrapie like spongiform encephalopathy produced in mice by feeding them wth cuprizone. *J. Pathol.* **109**: 245-250.
21. Quaglio, E., R. Chiesa, & D.A. Harris. 2001. Copper converts the cellular prion protein into a protease-resistant species that is distinct from the scrapie isoform. *J. Biol. Chem.* **276**: 11432-11438.
22. Supattapone, S., et al.. 1999. Prion protein of 106 residues creates an artificial transmission barrier for prion replication in transgenic mice. *Cell* **96**: 869-878.
23. Zahn, R. 2003. The octapeptide repeats in mammalian prion protein constitute a pH dependent folding and aggregation site. *J. Mol. Biol.* **334**: 477-488.
24. Premzl, M., et al. 2005. The prion protein gene: identifying regulatory signals using marsupial sequence. *Gene* **349**: 121-134.

## One-dimensional model of yeast prion aggregation

K. C. Kunes, D. L. Cox, and R. R. P. Singh

Department of Physics, University of California, Davis, California 95616, USA

(Received 3 May 2005; revised manuscript received 14 July 2005; published 9 November 2005)

Mammalian prion proteins (PrP) are of significant public health interest. Yeasts have proteins, which can undergo similar reformation and aggregation processes to PrP, without posing a threat to the organism. These yeast “prions,” such as SUP35, are simpler to experimentally study and model. Recent *in vitro* studies of the SUP35 protein found long aggregates, pure exponential growth of the misfolded form, and a lag time which depended weakly on the monomer concentration. To explain this data, we have extended a previous model of aggregation kinetics along with a stochastic approach. We assume reformation only upon aggregation and include aggregate fissioning and an initial nucleation barrier. We find that for sufficiently small nucleation rates or seeding by a small number of preformed nuclei, the models achieve the requisite exponential growth, long aggregates, and a lag time which depends weakly on monomer concentration. The spread in aggregate sizes is well described by the Weibull distribution. All these properties point to the preeminent role of fissioning in the growth of misfolded proteins.

DOI: 10.1103/PhysRevE.72.051915

PACS number(s): 82.39.Fk

## I. INTRODUCTION

Bovine spongiform encephalopathy (BSE) in cows, Scrapies in sheep, Creutzfeldt-Jakob Disease (CJD) and Kuru in humans are all diseases caused by a specific misfolded protein residing on neurons [1,2]. This prion protein (denoted PrP<sup>c</sup> in its normal form and PrP<sup>sc</sup> in its misfolded form) is present in all mammals and its full function, to date, is still unknown. A growing body of evidence strongly implies that this disease propagates not by nucleic acids, such as DNA or RNA, but by misfolded proteins (PrP<sup>sc</sup>) [3,4]. In our current understanding of prion diseases, the autocatalytic misfolding of the prion proteins plays a central role. The misfolded form PrP<sup>sc</sup> entices normal versions of the cellular prion protein (PrP<sup>c</sup>) to change conformation to the misfolded or disease causing form. Although PrP<sup>c</sup> and PrP<sup>sc</sup> have the same amino acid sequence (230 amino acids or residues), PrP<sup>sc</sup> has a higher beta sheet content than its normal form [1]. In humans, the disease is mostly sporadic, perhaps caused by a rare spontaneous misfold of the protein. But, infectious forms are also known to occur, such as in the case of new-variant CJD caused by eating BSE infected meat. In the latter case, infectious agents are presumably misfolded “seeds” that have entered the body from outside. Developing an understanding of the misfolding process should provide insights to prevention and/or cure of these diseases.

A class of proteins in yeast (SUP35) undergo a conformation change similar to the mammalian PrP. However, in case of yeast, this does not kill the organism. In fact, reconfigured, aggregated forms lead to a new phenotype [5]. Because they are not toxic, the misfolding is much easier to study for these proteins. Besides, it has been shown that aggregates produced *in vitro* can lead to the same phenotype, when added to a yeast cell [6–8]. Thus, it is possible to study the molecular aggregation processes for yeast prions in a test tube in tremendous detail, and a large quantity of experimental data is indeed available [9,10].

In this paper, we explore, using conventional kinetic as well as stochastic models, the aggregation dynamics for model yeast prions with a particular goal of explaining *in vitro* data [9,10] including (i) linear aggregates which grow by monomer addition, (ii) a modest concentration dependence of initial aggregate growth time varying roughly inversely as the square root of the monomer concentration, (iii) an observed distribution of aggregate sizes with a mode that is large (10s–100s of monomers), and (iv) a sigmoidal growth that is nearly exponential. We extend the nucleation and fissioning model of Collins *et al.* [9,10] from a moments-only model to monitor individual polymer lengths and show that we can readily obtain the above listed features in the data. In particular, we argue against a model based upon rapid equilibration with micelles, which can also provide a weak concentration dependence to initial aggregation times [11,12], but not the exponential growth implied by including explicit fission of aggregates. The fission rate plays a central role in determining the time scales as well as the mean aggregate length. The range of aggregate sizes assumes a Weibull distribution, also well known from other processes where fissioning is important. Thus the agreement with experiments highlights the importance of fissioning in the growth dynamics.

We study our kinetics both with continuous time modeling and via the discrete time stochastic Gillespie algorithm. The motivation for applying the latter is to determine where stochastic effects from the relatively rare processes of large length polymer generation may be observable in experiment.

In considering the relevance of these studies to mammalian prions, there is an important caveat that arises from the fact that mammalian prions are glycosyl phosphatidyl-inositol (GPI) anchored on neuron cells and, thus, move in a two-dimensional plane and, hence, can lead to areal aggregates [13,14]. The aggregation and fissioning processes are likely to be very different there. Nevertheless, the dominance of fissioning can lead to long-time growth kinetics, which are in many ways closely related.

# 1D Prion Aggregation Model

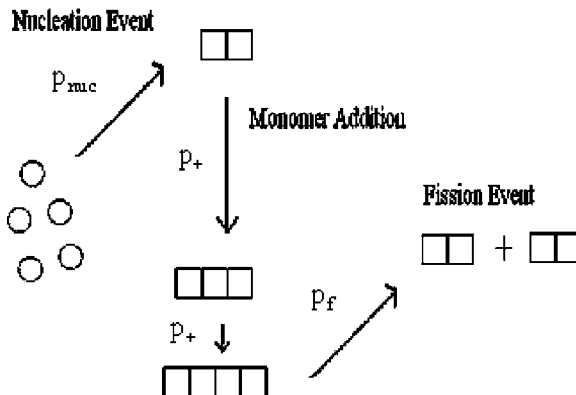


FIG. 1. Aggregation model where circles are normal proteins ( $\text{psi}^-$ ) and squares are the misfolded type [ $\text{PSI}^+$ ].

## II. MODELS

We consider a one-dimensional aggregation model that includes a nucleation barrier, elongation by monomer addition, and fission (Fig. 1). The same kind of kinetics was considered by Collins *et al.* in the form of moments of the full polymer kinetic equations, but not in the explicit length resolved form considered here [9,10]. The assumption that monomer (rather than oligomer) addition dominates and the need for fission are underscored by the data we seek to describe on yeast prions [9,10]. We shall distinguish the model quantitatively from a nonfission based model later in the paper.

A nucleation event occurs very rarely and is composed of two normal [ $\text{psi}^-$ ] proteins interacting in such a way that a misfold occurs and they bind together; this two prion aggregate is called a [ $\text{PSI}^+$ ] dimer. The actual size of the nucleus is not a critical parameter in our model, as long as the nucleation process is much slower than aggregation. Once an aggregate has been created, it can elongate by monomer addition. Our model does not consider fusion between two oligomers. The rate of fissioning becomes important only when an oligomer of large enough size arises. After an oligomer has fissioned into smaller pieces, the individual pieces can grow and fission. When a fission leads to a monomeric product, we assume that it returns to the properly folded state. This process leads to a steady state distribution of oligomer sizes and a pure exponential growth. It continues until the monomer concentration begins to dwindle significantly.

We note that the lag time for the *in vitro* growth of yeast prion-like proteins is reproducible in experiments, and shows a weak dependence on monomer concentration. Hence, it is not likely that it can be associated with pure nucleation (at least at low initial monomer concentration), which being a rare event will lead to a distribution of time scales as well as a rather strong dependence on monomer concentration, depending on the size of the nucleus. We will assume that the lag time arises from the growth of misfolded material to an observability threshold. This assumption is valid if the nucleation time scales, which are long compared to other micro-

scopic time scales, are still shorter than this latter time scale. It is also valid when a small number of nucleated seeds exist at the time of the preparation of the experimental samples. As shown elsewhere, a weak concentration dependence to lag time can derive from rapid equilibration of monomer concentration with nonfibrillar oligomers [11,12]; this model is not supported in the current context, and we shall discuss this later in this section.

### A. Kinetic model

Our first approach is to use kinetic equations to describe the aggregation process [15,16]. In order to use the rate equations, one must assume a large number of monomers. The kinetic rate equations for our model are as follows

$$\frac{dn_1}{dt} = -2p_{nuc}n_1^2 - 2p_+n_1 \sum_{i=2}^{N-1} n_i + 2p_f \sum_{i=2}^{N-1} n_i, \quad (1)$$

$$\frac{dn_2}{dt} = p_{nuc}n_1^2 - 2p_+n_1n_2 - p_f n_2 + 2p_f \sum_{i=3}^{N-1} n_i, \quad (2)$$

$$\frac{dn_k}{dt} = 2p_+n_{k-1}n_1 - 2p_+n_kn_1 - (k-1)p_f n_k + 2p_f \sum_{i=k+2}^{N-1} n_i, \quad (3)$$

$$\frac{dn_N}{dt} = 2p_+n_{N-1}n_1 - p_f(N-1)n_{N-1}, \quad (4)$$

where  $n_1$  is the monomer concentration,  $n_k$  is the concentration of  $k$ -mers, and  $N$  is the longest oligomer kept in the calculation. The parameters  $p_{nuc}$ ,  $p_+$ , and  $p_f$  can be adjusted to change the rate of nucleation, fusion, and fission, respectively. Since one of these parameters can be absorbed into the definition of the time  $t$ , we will set  $p_+=1$ . Furthermore, we will set the initial monomer concentration to unity. The equations listed above form a system of  $N$ -coupled differential equations which cannot be solved analytically because of the nonlinear terms.

An analytical solution is possible if  $n_1$  can be assumed to be a constant and  $n_2$  and higher are much, much smaller than the monomer concentration. Then the set of equations become linear and can be solved by several techniques, such as a Laplace transformation. This is not a bad approximation, for, as we will see, during much of the growth process the monomer concentration is nearly constant. Only at the end, the monomer concentration begins to dwindle and the amount of misfolded monomers saturates. It is useful to define the zeroth and first moments of the aggregate size distribution as

$$A = \sum_{i=2}^N n_i, \quad (5)$$

$$M = \sum_{i=2}^N i * n_i, \quad (6)$$

where  $A$  is the number of polymer aggregates and  $M$  is the total number of monomers in aggregate. Since the overall number of proteins is conserved, the rate of change of  $M$  is given by

$$\frac{dM}{dt} = -\frac{dn_1}{dt}, \quad (7)$$

whereas the rate of change of  $A$  is given (ignoring the cutoff  $N$ ) by the equation

$$\frac{dA}{dt} = p_{nuc}n_1^2 - p_f n_2 + p_f \sum_{i=3} (i-3)n_i. \quad (8)$$

If we ignore the terms depending on  $n_2$  and assume  $n_1$  is a constant, we get two linear coupled equations,

$$\frac{dA}{dt} = \text{const} + p_f M - 3p_f A, \quad (9)$$

$$\frac{dM}{dt} = \text{const} + (2p_f n_1 - 2p_f)A. \quad (10)$$

We set  $p_+ = 1$  to set the unit of time. Anticipating  $M \gg A$ , which means that the mean aggregate size is much bigger than unity. The above equations mean that the  $M$  and  $A$  both grow exponentially as  $e^{\lambda t}$ , with  $\lambda$  given by

$$\lambda = \sqrt{2p_f(n_1 - p_f)} \approx \sqrt{2p_f n_1}. \quad (11)$$

During the exponential growth, the mean aggregate size is given by

$$\bar{L} = \frac{M}{A} = \sqrt{\frac{2n_1}{p_f}}. \quad (12)$$

If we further assume that the lag time is given by the time it takes for the misfolded proteins to reach a detectable threshold  $M_f$ , then the lag time is given by

$$t_{lag} \sim \frac{\ln \frac{M_f}{C(n_1)^2}}{\sqrt{2p_f n_1}}, \quad (13)$$

where  $C$  is a constant and the  $n_1$  dependence comes from the logarithm. We will see that these results are confirmed by a complete numerical integration of the differential equations. Thus, this model demonstrates the requisite  $t$ -lag dependence seen in the experimental data, namely the inverse square root dependence on the monomer concentration, up to logarithms, shown in Fig. 2. We note that the fit in Fig. 2 is not sensitive to the logarithmic terms.

#### Kinetic model results

A numerical integration approach was used to study the full set of equations. We used the fourth order Runge-Kutta algorithm for solving differential equations and to obtain

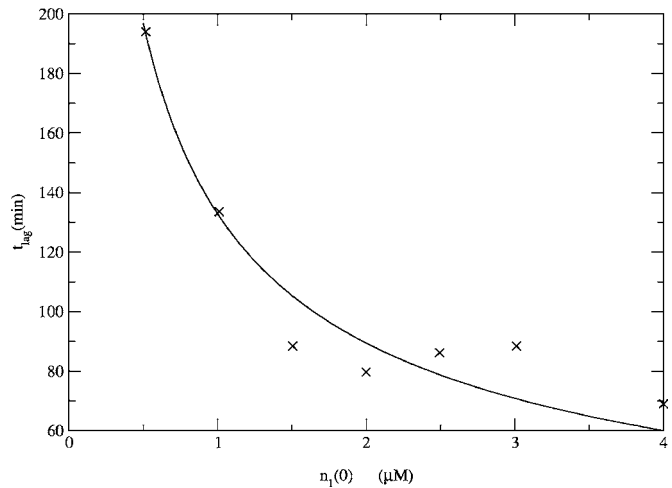


FIG. 2. Lag time ( $t_{lag}$ ) vs initial monomer concentration [ $n_1(0)$ ]. The crosses are data from Collins *et al.* in Ref. [9]. The continuous curve is a fit to the equation  $t_{lag} = a_0 [n_1(0)]^{-1/2} \log a_1/n_1(0)$ , with  $a_0 = 9.22 \text{ min} * (\mu\text{M})^{1/2}$  and  $a_1 = 1.80 \times 10^6 \mu\text{M}$ , following Eq. (13).

length distributions and growth curves for the system.

In Fig. 3, we show plots of  $\log(M)$  as a function of time. We have chosen a set of parameters yielding mean lengths in the 10s–100s and displaying manifest exponential growth in  $M(t)$  vs  $t$  plots. It is evident that there is a regime where  $\log(M)$  varies linearly with time, implying a pure exponential growth. This region of exponential growth is not limited to just a few chosen parameter values, but can be achieved over a wide range of  $p_f$  values. In Fig. 3, we plot the total number in aggregate vs time, now on a linear scale. The sigmoidal growth is now evident as the exponential increase tapers off when the monomers begin to deplete. This is also consistent with the experimental results [9].

As discussed earlier, the mean length of the aggregates has a simple inverse square-root dependence on the rate of fission. Thus by tuning the rate of fission, it is possible to obtain mean aggregate lengths (see Fig. 4), which appear

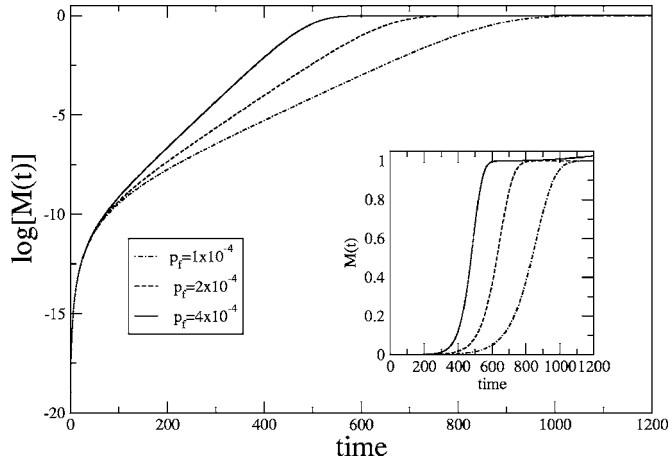


FIG. 3.  $\log[M(t)]$  vs time, with parameter values  $n_1(0) = 1$ ,  $p_+ = 1$ ,  $p_{nuc} = 10^{-8}$ . The linear regions illustrate regions of pure exponential growth.  $M(t)$  vs time illustrating sigmoidal growth is shown in the inset. Note that time is in units of  $1/[n_1(0)p_+]$ .

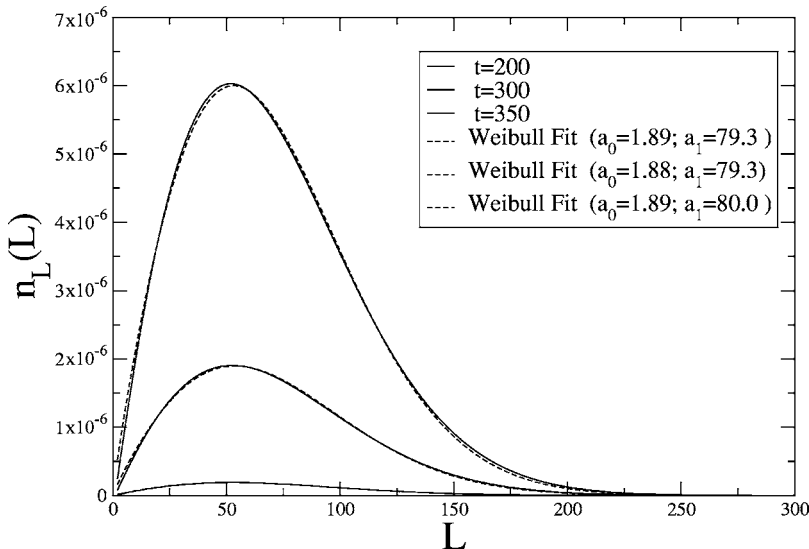


FIG. 4. Length distribution,  $n_l$  vs length  $L$ , from the kinetic equations during the exponential growth phase, compared with the Weibull distribution, Eq. (14).

qualitatively consistent with those observed experimentally displaying lengths in the tens of hundreds (see especially slide 9 at Ref. [10]). In Fig. 5, this mean length is plotted vs time for a different fission rate  $p_f$ . We see that the mean aggregate length is constant during the exponential growth. In Fig. 6, we show the variation of the exponential growth rate with  $p_f$  compared with the analytic calculations. One can see that they agree closely. Note also that  $p_f$  values of order  $10^{-4}$  will give the lengths seen *in vitro*.

We can also determine the distribution of aggregate sizes in our calculations. The concentration of aggregates of different sizes relative to the initial concentration of monomers are shown in Fig. 4 for a given value of the fission parameter ( $p_f=4 \times 10^{-4}$ ) at three different times during the exponential growth phase of the simulation. Clearly, the distribution is fairly stable during the exponential growth phase, further strengthening the argument for a simple steady state. These length distributions are well fitted by a Weibull distribution given by the relation,

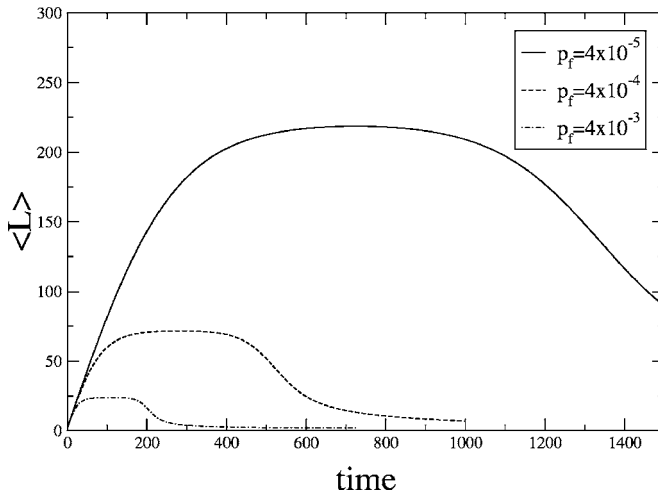


FIG. 5. Mean length vs time for different  $p_f$ ;  $n_1(0)=1$ ,  $p_+=1$ ,  $p_{nuc}=10^{-8}$ . The plateau corresponds to the constant mean length during the exponential growth phase. Note that time is in units of  $1/[n_1(0)p_+]$ .

$$f(x) = \frac{a_0}{a_1} \left( \frac{x}{a_1} \right)^{a_0-1} \exp \left[ - \left( \frac{x}{a_1} \right)^{a_0} \right]. \quad (14)$$

Apart from an overall normalization, the two key parameters of the distribution are the mean  $a_1$  and the power law at small  $x$  set by  $a_0-1$ . This distribution is found to be ubiquitous in nature [17]. For example, a dropped piece of coal will have shattered pieces that follow an asymmetrical distribution with more pieces on the smaller end. Our model follows a similar idea (i.e., taking a larger length and shattering it into smaller lengths) and a similar distribution. In our simulations, the quantity  $a_0$  is close to 2 for a range of parameters studied. During subsequent times, the peak of this curve shifts to the left as saturation occurs and the only process left is to fission. (The shift in peak at later times are not shown here.)

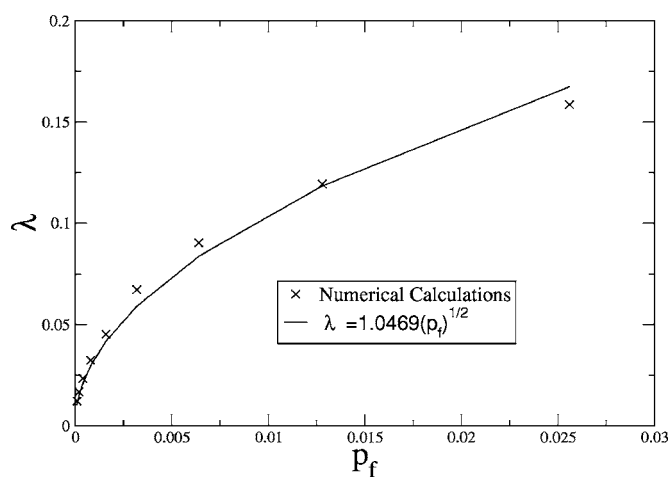


FIG. 6. Exponential growth rate  $\lambda$  vs  $p_f$  compared with simple square-root dependence predicted by Eq. (11) for different parameter values,  $n_1(0)=1$ ,  $p_+=1$ ,  $p_{nuc}=10^{-8}$ .

## B. Comparison to nonfissioning micelle model

The coupling of the observation of weak concentration dependence with exponential growth strongly supports a model dominated by fissioning of aggregates constructed by monomer addition. Indeed, centrifugation studies confirm that monomers are the dominant species in the *in vitro* medium, and examination of the aggregation kinetics suggests a critical nucleus of small size [9].

It is thus important to contrast with other models for which a weak concentration dependence can be derived. Notably, the work of Lomakin *et al.* [11,12] considers kinetics with monomer growth of polymers as well as micellar oligomers composed of  $\mathcal{M}$  monomers of concentration  $n_{\mathcal{M}}$  which may or may not be off pathway. This model may be of relevance to other *in vitro* studies of yeast prion aggregation [18] for which there is evidence of oligomer formation and growth and a weak concentration dependence to the lag time. If the oligomers are off pathway, then assuming an equilibration with monomers leads to a buffering of the monomer concentration assuming an initially high input concentration and sufficiently rapid equilibration. There is a crossover or critical concentration  $n^*$  for this dictated by the equilibrium constant  $K_{\mathcal{M}}$  between monomers and micelles ( $K_{\mathcal{M}}=n_{\mathcal{M}}/n_1^{\mathcal{M}}$ ) given by

$$n^* = (\mathcal{M}K_{\mathcal{M}})^{1/1-\mathcal{M}}. \quad (15)$$

Lomakin *et al.* argue that for a total equilibrated protein concentration  $n_T$  obtained prior to fibril growth,

$$n_T = n_1 + \mathcal{M}n_{\mathcal{M}} \quad (16)$$

$$= n_1 + n^* \left( \frac{n_1}{n^*} \right)^{\mathcal{M}}. \quad (17)$$

From these equations, it is clear that there is an approximate two-state behavior provided  $\mathcal{M} \gg 1$ . For  $n_T \ll n^*$ , then  $n_T \approx n_1$  and aggregation kinetics can be strongly concentration dependent. However, for  $n_T \geq n^*$ , then  $n_1 \approx n^*$ , that is, the micelles buffer the monomer concentration. This would lead to a weak dependence of fibrillar growth upon subsequent increase of initial monomer concentrations.

There are two routes by which this model can be applied to the data of Collins *et al.* [9,10]. First, if the fibrils are formed from monomer addition to the micelles without resulting fission of fibrils, then one will expect a quadratic growth in time [19,20] to the total number of aggregated proteins, namely

$$M(t) \approx \frac{1}{2} p_+^2 n_1^2 n_{\mathcal{M}} t^2, \quad (18)$$

$$\approx \frac{1}{2\mathcal{M}} p_+^2 n_1^{2+\mathcal{M}} (n^*)^{1-\mathcal{M}} n_{\mathcal{M}} t^2, \quad (19)$$

which is very weakly dependent upon  $n_1(0)$  provided  $n_1(0) \approx n_T \geq n^*$ , but varies strongly as  $n_1(0)^{2+\mathcal{M}}$  in the opposite limit. Solving for where  $M(t_{\text{lag}})=M_c$  characteristic of the observability threshold yields

$$t_{\text{lag}} = \frac{1}{p_+ n_1} \sqrt{\frac{2M_c(n^*)^{\mathcal{M}-1}}{(n_1)^{\mathcal{M}}}}. \quad (20)$$

For  $n_1(0) \ll n^*$ ,  $t_{\text{lag}}$  varies as  $n_1(0)^{-(1+\mathcal{M}/2)}$ , at odds with experiment [9], while for  $n_1(0) \geq n^*$  and  $\mathcal{M} \gg 1$ ,  $t_{\text{lag}}$  is approximately independent of  $n_1(0)$  [it will decrease weakly with increasing  $n_1(0)$ ].

Second, if the micelles are off pathway, then their principal impact on the fibrillar aggregation is on buffering. Assuming a critical fibrillar nucleus of length  $p$ , which equilibrates with the monomers via a constant  $K_p = n_p/n_1^p$ , the same considerations of aggregation kinetics as in the preceding paragraph give a lag time given by

$$t_{\text{lag}} = \frac{1}{p_+ n_1} \sqrt{\frac{2M_c}{K_p (n_1)^p}}. \quad (21)$$

For  $n_1(0) \ll n^*$ , this varies as  $n_1(0)^{-(1+p/2)}$  is at odds with Collins *et al.* [9], while it is approximately independent of  $n_1(0)$  for  $n_1(0) \geq n^*$  and  $p \geq 2$ . For small nuclei ( $p \approx 2-5$ , say), the dependence can be relatively strong on  $n_1(0)$  even in this limit.

Hence, via either on-pathway or off-pathway micelles, in this model there is a route to weak dependence of lag time (defined as the threshold for observation) upon initial monomer concentration requiring  $n_1(0) \geq n^*$  and  $\mathcal{M}, p \geq 1$ . However, there are several problems in connecting this to the experiments of Collins *et al.* First, exponential growth is unambiguously observed, indicating that fission of fibrils occurs. The micelle model of this subsection has no fission. This highlights the important role of fission for the prion phenomenon. Second, in these experiments, the starting solution contains almost entirely monomers and not micelles. This implies that even if micelles form, one is always in the limit of  $n_1(0) \ll n^*$ , leading to strong concentration dependence. Third, the width of the fibrils obtained in this experiment is apparently monomeric, which is not readily compatible with growth by monomer addition to micelles, and rather must be obtained by addition to a critical fibril nucleus. The data suggest that this critical fibril nucleus is of length  $p \leq 6$ , not consistent with the assumption  $p \geq 1$ .

Hence, we do not believe that the micelle based model can explain the data of Collins *et al.* [9,10].

## C. Stochastic model

In this section, we develop a stochastic treatment of the model, similar to a model proposed by Pöschel *et al.* [21]. Our main motivation is to be able to treat species with small numbers, in which case the continuous deterministic approach will break down. As we will see, the stochastic approach largely agrees with the deterministic model for the parameter values considered here for aggregate quantities [e.g.,  $M(t)$ ]. However, for distributions there can be substantial stochastic noise at short times. Another advantage of the stochastic approach is that it can be readily extended to study

TABLE I. Propensities of stochastic processes.

Nucleation propensity	Fusion propensity for monomer addition		Higher order fusion term	Fission propensity for monomer		Higher order fission term
	Chain length 2	Chain length 3		Chain length 2	Chain length 3	
$g_{nuc}N_1(n_1-1)$	$2g_+N_1N_2$	$2g_+N_1N_3$	...	$g_fN_2$	$2g_fN_3$	...

two-dimensional aggregates as well as the problem of multiple prion “strains,” in which case the treatment of a small number of heteroaggregates would be important to model the extent to which strains breed true.

The Gillespie algorithm provides an exact way to treat the stochastic problem of chemical reactions [22]. In our case, the polymers of different lengths are the different chemical species. The processes of nucleation, monomer addition, and fission are assumed to be stochastic. In other words, the number of polymers of different length at time  $t$ , only define the propensities (or normalized probability) for the different reactions to happen at that time. Once a reaction takes place, the number of polymers is altered and the propensities are changed. The Gillespie algorithm is a Monte Carlo treatment that deals with the stochastic process by using a pair of random numbers at each step, one to decide which event will occur next and another to decide how long will it be until the next event takes place. This process can be repeated to follow the dynamical behavior of the system.

Our model has the corresponding propensities

$$g_{nuc}N_1(N_1-1) + 2g_+N_1\sum_{i=2}^{\infty} N_i + g_f\sum_{i=2}^{\infty} (i-1)N_i, \quad (22)$$

where  $g_{nuc}$ ,  $g_+$ , and  $g_f$  are, respectively, the nucleation, fusion, and fission parameters in the stochastic model. In our model, each propensity was assigned a bin in an array. A random number generator decides which bin is selected.

Table I illustrates physically the propensities at a given time. A normalized random number generator selects which element in the array will occur and the time it took to create that event. After an event occurs, the corresponding propensities are updated and the process is repeated.

In order to compare the results achieved from the continuous to stochastic model, a mapping of the Gillespie parameters to the kinetic parameters is required. For this, we need to develop an approximate equation satisfied by the monomer concentration in the stochastic simulations and compare it with the rate equations. In the stochastic case, one has a master equation that relates the probability distribution associated with a different number of polymers at time  $t+dt$  to those at time  $t$ . We will make a mean-field approximation for different kind of  $k$ -mers, namely  $\langle N_i * N_k \rangle = \langle N_i \rangle * \langle N_k \rangle$ . Thus, we can consider the approximate master equation, which only tracks changes in the monomer number. We arrive at the equation,

$$P_1(N_1, t+dt) = P_1(N_1, t) \left[ 1 - g_{nuc}N_1(n_1-1)dt - g_+N_1\sum_{i=2}^{\infty} N_i dt \right. \\ \left. - 2g_f\sum_{i=2}^{\infty} N_i dt \right] + 2P_1(N_1-1, t)g_f\sum_{i=3}^{\infty} N_i dt \\ + P_1(N_1-2, t)g_fN_2 dt + P_1(N_1+1, t)g_+N_1 \\ \times \sum_{i=2}^{\infty} N_i dt + P_1(N_1+2, t)g_{nuc}N_1(N_1-1)dt, \quad (23)$$

where  $N_1$  is the number of monomers,  $P_1(N_1, t+dt)$  is the probability to have  $N_1$  monomers at a later time  $t+dt$ .  $P_1(N_1, t)$  is the probability to have  $N_1$  monomers at time  $t$ . It is multiplied by the probability that no reaction occurs in time  $dt$  that changes  $N_1$ . The rest of the terms represent the probability to have a different number of monomers at time  $t$  but then a reaction happens in time  $dt$  leading to  $N_1$  monomers at time  $t+dt$ .

Now using the definition of the derivative, one can rearrange the equation and multiply both sides by  $N_1$  to get the average rate of change of  $N_1$ . After shifting some indices to get every probability to have the form  $P_1(N_1, t)$  and using the appropriate volume element (denoted by  $V$ ) to normalize the counts to a concentration, one arrives at the equation for the mean number of monomers,

$$\frac{1}{Vg_+ dt_{gil}} \frac{dn_1}{dt} = -2g_{nuc}n_1^2 - 2n_1\sum_{i=2}^{\infty} n_i + 2\frac{g_f}{V} \sum_{i=2}^{\infty} n_i. \quad (24)$$

By comparing with the rate equations discussed before, we obtain the parameter mapping

$$p_+ = 1, \quad (25)$$

$$p_{nuc} = g_{nuc}, \quad (26)$$

$$p_f = \frac{g_f}{V}, \quad (27)$$

$$t_{kinetic} = g_+ V t_{gillespie}. \quad (28)$$

### Results stochastic approach

After achieving the parameter mapping, we studied the stochastic models with  $10^6$  initial monomers. The numerical results are shown in the next few figures. In Fig. 7, the growth of the aggregate material is shown on a logarithmic

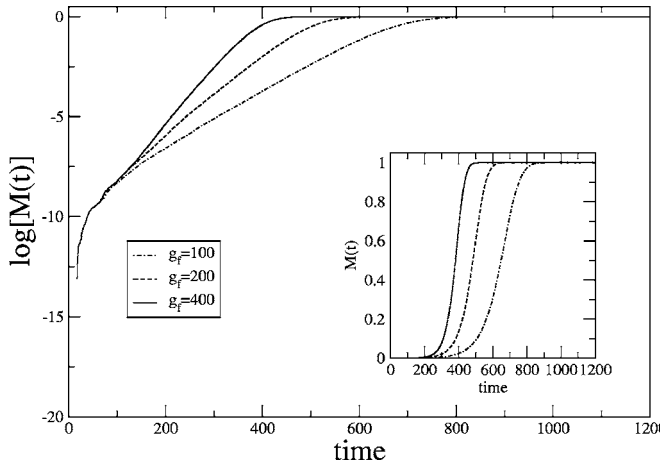


FIG. 7.  $\log[M(t)]$  and  $M(t)$ , shown in the inset, vs time obtained by the Gillespie algorithm with  $N_1(0)=10^6$ ,  $g_+=1$ ,  $g_{nuc}=10^{-8}$  for different fission rate  $g_f$ . Note that time is in units of  $1/g_+$ .

and on a linear scale. It is evident that they are in excellent agreement with the corresponding calculations for the kinetic model. In Fig. 8, we show plots of the mean length as a function of time, and in Fig. 9, the corresponding distribution of length scales during the exponential growth phase. It is again evident that there is a steady state during the exponential growth and the mean lengths reach a plateau value. The stochastic effects are much larger in the distribution and in the mean length, but the overall results agree well with the kinetic model. The fits to the Weibull distribution are again good with comparable parameters. The differences between the kinetic and stochastic Weibull parameters ( $a_0$  and  $a_1$ ) are less than 10%. This shows that for  $10^6$  monomers and for mean aggregate lengths up to a few hundred, the dominant species still occur in large enough numbers so that stochastic effects do not change the results in a significant way.

### III. DISCUSSION

In this paper, we have used a deterministic kinetic and a stochastic Monte Carlo approach to model the dynamics of

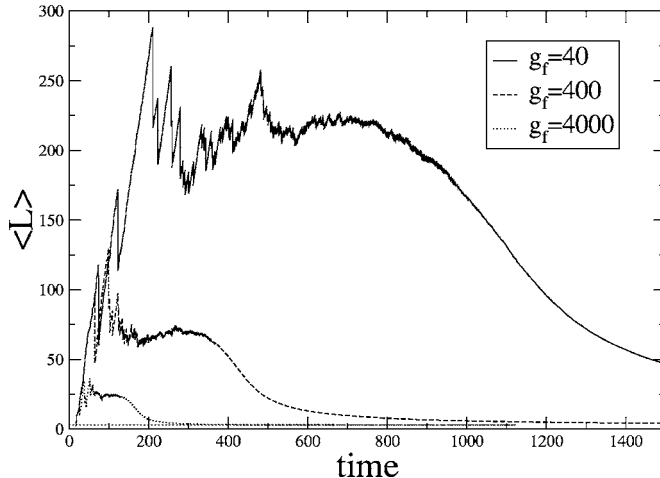


FIG. 8. Mean length vs time in units of  $1/g_+$  for different fission rates  $g_f$  obtained by the Gillespie algorithm. The parameter values are  $N_1(0)=10^6$ ,  $g_+=1$ ,  $g_{nuc}=10^{-8}$ .

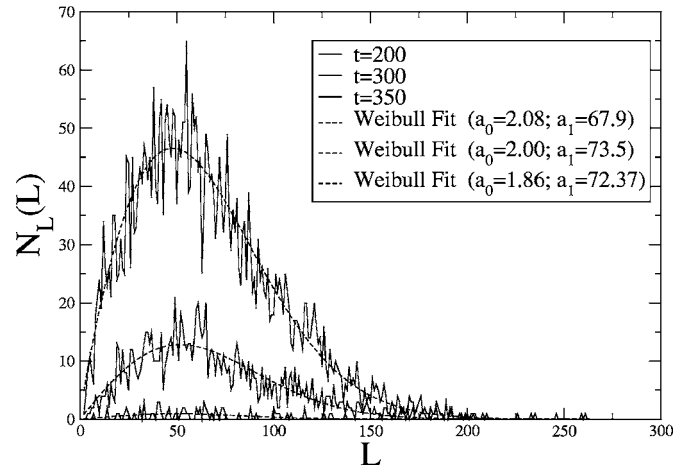


FIG. 9. Length distributions at different times during the exponential growth phase obtained by the Gillespie algorithm for  $g_f=400$  and fitted by the Weibull distribution.

yeast prion growth. For the parameters relevant to *in vitro* experiments, where mean aggregate size is of order 100s of monomers, and the number of monomers is larger than  $10^6$ , the two approaches agree well with each other, showing that stochastic effects are not dominant. The studies confirm that the key experimental features of the growth of yeast prions can be well captured by these nucleation-growth-fissioning models. They lead to an exponential and/or sigmoidal growth, an inverse square-root dependence of the lag time on the monomer concentration, and aggregate sizes that depend on the rate of fission. We predict that the aggregate size distributions should be Weibullian, reflecting the importance of fissioning in the growth process. We also predict, for sufficiently large times, that the steady state aggregate length will drop as fissioning converts large aggregates to those of minimal size. We have argued that models in which monomers equilibrate with micelles but do not fission [11,12], which are capable of producing lag times having a weak concentration dependence for a sufficiently high initial monomer concentration, are in fact not appropriate for the data of Collins *et al.* [9,10].

We note that the *in vitro* aggregation work of Serio *et al.* [18] appears to come to different conclusions than that of Collins *et al.* [9] and may be ripe for a discussion in terms of the micelle models. We do not understand the discrepancies between these two sets of experiments.

We note that the results on yeast prions discussed here and recent work on mammalian prions stripped of their GPI membrane anchors [23,24] suggest that a fundamentally different mechanism for fission is at play for the latter proteins *vis-à-vis* yeast. In the recent experiments, transgenic mice expressing the cellular prion protein without the residues necessary for the GPI anchor are exposed to anchorless infectious prions; in time course experiments, prion aggregates are produced which retain infectivity. However, the infected mice with anchorless  $\text{PrP}^C$  do not show clinical symptoms. Moreover, the time course data {see Fig. 1(c) of Chesebro *et al.* [24]} show two remarkable characteristics: (i) they are nonsigmoidal in shape, with the infectious prion content at long times significantly exceeding that of infected wild type

mice at death, (ii) the time scales to reach the levels of infectivity characteristic of wild type mice at the corresponding infectious dose are quite long. Indeed, the time course data can be fit roughly by a quadratic in time curve characteristic of nonfissioning aggregation to an initial concentration of infectious seeds. Evidently, the binding of cellular mammalian prions to the membrane is critical to the fissioning process, while for yeast prions fissioning of aggregates *in vitro* is observed [9].

In the future, we hope to extend this model to study yeast prion strains, where we expect the stochastic treatment to be the key to dealing with rare heteroaggregates. An under-

standing of this process should lead to insights into the important problem of strain dynamics in mammalian prions.

## ACKNOWLEDGMENTS

We acknowledge the support of the U.S. Army Congressionally Mandated Biomedical Research Fund (Grant No. NP020132) and acknowledge the support of the NSF sponsored Center for Theoretical Biological Physics (NSF Grant Nos. PHY0216576 and 0225630). D.L.C. acknowledges the support of the J. S. Guggenheim Memorial Foundation.

---

[1] For a general introduction to prion biology, see S. B. Prusiner, *Prion Biology and Diseases*, 2nd ed. (C.S.H.L. Press, Cold Spring Harbor, NY, 2004).

[2] A. Aguzzi and M. Polymendou, *Cell* **116**, 313 (2004).

[3] S. B. Prusiner, *Science* **216**, 136 (1982).

[4] G. Legname, I. Baskakov, H. Nguyen, D. Riesner, F. Cohen, S. DeArmond, and S. Prusiner, *Science* **305**, 673 (2004).

[5] R. B. Wickner, *Science* **264**, 566 (1994).

[6] H. E. Sparrer, A. Santosh, F. C. Szoka, Jr., and J. S. Weissman, *Science* **289**, 595 (2000).

[7] C. Y. King and R. Diaz-Avalos, *Nature (London)* **428**, 319 (2004).

[8] M. Tanaka, P. Chien, L. Z. Osherovich, and J. S. Weissman, *Nature (London)* **428**, 323 (2004).

[9] S. R. Collins, A. Douglass, R. Vale, and J. S. Weissman, *PLoS Biol.* **2**, 10 (2004).

[10] <http://online.itp.ucs.edu/online/bionet03/collins/>

[11] A. Lomakin, D. S. Chung, G. B. Benedek, D. A. Kirschner, and D. A. Teplow, *Proc. Natl. Acad. Sci. U.S.A.* **93**, 1125 (1996).

[12] A. Lomakin, D. B. Teplow, D. A. Kirschner, and G. B. Benedek, *Proc. Natl. Acad. Sci. U.S.A.* **94**, 7942 (1997).

[13] A. Slepoy, R. R. P. Singh, F. Pazmandi, R. V. Kulkarni, and D. L. Cox, *Phys. Rev. Lett.* **87**, 058101 (2001).

[14] Holger Wille, Melissa D. Michelitsch, Vincent Guénebaut, Surachai Supattapone, Ana Serban, Fred E. Cohen, David A. Agard, and Stanley B. Prusiner, *Proc. Natl. Acad. Sci. U.S.A.* **99**, 3563 (2002).

[15] D. Hall and H. Edskes, *J. Mol. Biol.* **336**, 775 (2004).

[16] J. Masel, V. A. A. Jansen, and M. A. Nowak, *Biophys. Chem.* **77**, 139 (1999).

[17] W. Brown and K. Wohletz, *J. Appl. Phys.* **78**, 2758 (1995).

[18] T. R. Serio, A. G. Cashikar, A. S. Kowal, G. J. Sawicki, J. J. Moslehi, L. Serpell, M. F. Arnsdorf, and S. L. Lindquist, *Science* **289**, 1317 (2000).

[19] F. Ferrone, *Methods Enzymol.* **309**, 256 (1999).

[20] S. Chen, F. A. Ferrone, and R. Wetzel, *Proc. Natl. Acad. Sci. U.S.A.* **99**, 11884 (2002).

[21] T. Pöschel, N. V. Brilliantov, and C. Frömmel, *Biophys. J.* **85**, 3460 (2003).

[22] D. Gillespie, *J. Comput. Phys.* **22**, 403 (1976).

[23] P. Chien and J. Weissman, *Nature (London)* **410**, 223 (2001).

[24] B. Chesebro, M. Trifilo, R. Race, K. Meade-White, C. Teng, R. LaCasse, L. Raymond, C. Favara, G. Baron, S. Priola, B. Caughey, E. Masliah, and M. Oldstone, *Science* **308**, 1435 (2005).

# The Materials Science of Protein Aggregation

D.L. Cox, H. Lashuel, K.Y.C. Lee, and R.R.P. Singh

## Abstract

Numerous human diseases are associated with conformational change and aggregation of proteins, including Alzheimer's, Parkinson's, prion diseases (such as mad cow disease), familial amyotrophic lateral sclerosis (ALS, or Lou Gehrig's disease), Huntington's, and type II (mature onset) diabetes. In many cases, it has been demonstrated that conformational change and aggregation can occur outside living cells and complex biochemical networks. Hence, approaches from materials and physical science have enhanced our understanding of the role of protein aggregation in these diseases at the molecular and nanoscale levels. In this article, we will review what is known about these protein structures from the perspective of materials science, focusing on the details of emergent oligomeric and nanotube-like structures, their interactions with model lipid bilayers, how the structures relate to observed biological phenomena, and how protein aggregation and amyloid formation can be employed for the good in biology and materials science.

**Keywords:** amyloid diseases, complex adaptive matter, emergent behavior, prion diseases, protein aggregation, protofibrils, nanotubes, nanowires.

## Amyloid Diseases: A Truly Emergent Phenomenon

The primary goal of the study of complex adaptive matter is to identify the key organizing principles that govern materials phenomena at given length and time scales. In the case of the folding of individual globular proteins into their functional structures, we know a great deal. For example, the local rules governing  $\alpha$ -helical secondary structure have been understood in detail for some 40 years;<sup>1,2</sup> indeed, the  $\alpha$ -helix was predicted by Pauling and collaborators prior to discovery.<sup>3</sup> For the global tertiary structure of the protein, extensive experiments and simulation studies show that proteins engineered by evolution to experience minimal frustration in the interactions between closely contacted amino acids (or residues) develop funneled energy landscapes and relatively rapid (and multiple) pathways to folding after synthesis.<sup>4</sup> As discussed in the article by Ramirez in this issue, "frustration" refers to the effect of competing interactions that make it impossible to favorably lower the interaction energy.

However, we have comparatively little understanding of the organizing principles governing structure formation for proteins interacting with other proteins or membranes. This lack of knowledge is problematic, because proteins left alone tend to spontaneously aggregate, often by formation of  $\beta$ -sheet structures, which are not governed by local formation rules like  $\alpha$ -helices (the distances between hydrogen bonding residues along the backbone can be great).  $\beta$ -sheets are formed from approximately linear stretches of peptide that hydrogen-bond from line to line. These structures are especially prone to protein aggregation due to favorable edge-to-edge hydrogen bonding between sheets.<sup>5</sup> This aggregation tendency is an obstacle in high-throughput proteomics, where one is interested in measuring the properties of individual proteins.<sup>6</sup>

Purposeful biological aggregation of monomeric proteins, as in the assembly of actin filaments or microtubules,<sup>7</sup> is usually highly regulated and energetically con-

trolled (we will discuss tightly controlled and biologically useful  $\beta$ -sheet self-assembly later in the article). Living organisms have evolved an effective quality-control system to prevent protein misfolding and aggregation, where chaperone proteins provide "safe houses" for folding proteins,<sup>8</sup> and the ubiquitin/proteasome system ensures rapid degradation or disposal of misfolded proteins.

Table I conveys the tragic side of uncontrolled  $\beta$ -sheet self-assembly: it summarizes the key aspects of seven (out of dozens) prominent human amyloid diseases. Amyloid means "starch-like"—the aggregates stain like starch. These diseases typically arise in old- or middle-aged populations, and frequently arise spontaneously or sporadically rather than from genetic predisposition. Indeed, for spontaneous Alzheimer's, Parkinson's, prion, and immunoglobulin light chain diseases, incidence varies little between countries. Moreover, prion diseases, the lone infectious type of amyloid disease, show highly reproducible dose-versus-incubation-time distributions for intercerebrally inoculated animals.<sup>9</sup> Remarkably, infectious protein-only prion aggregates have been grown *in vitro*,<sup>10</sup> proving that the protein interaction properties alone, without additional biochemical guidance, account for the disease.

These observations suggest that these diseases can be studied from the perspective of materials growth, without extensive biological modulation. Indeed, it appears that the growth of amyloid structure has much in common with the oriented aggregation of inorganic, nearly monodispersed nanoparticles.<sup>11</sup> We seek here to portray the growing scientific movement toward the use of concepts and tools from materials science in the study of amyloidogenic proteins to elucidate the mechanisms of disease and design new materials.

## Amyloid Structures: Plaques, Protein Nanotubes, and Oligomers Plaques

The extracellular and/or intracellular accumulation of amyloid fibrils in the form of plaques or inclusions (Lewy bodies) in the brain is a defining hallmark for several neurodegenerative diseases (Figure 1). For example, Alzheimer's disease patients have large quantities of postmortem brain plaques, predominantly composed of 40–42-amino-acid-long A $\beta$  peptides that are cleaved by protease proteins from the Alzheimer's precursor protein (BAPP).<sup>12</sup> These micrometer-scale plaques are composed of multi-polymeric strands of the peptide, called fibrils (Figure 1e), which

**Table I: Aspects of Some Human Amyloid Diseases with Associated Protein Aggregation.**

Disease	Protein/Peptide	Function	Heritable Component	Incidence	Onset Age* (Years)
Alzheimer's <sup>51</sup>	$\beta$ -42 (from BAPP) and $\tau$	?	~25%	~50% of post-85-yr-old population	>65
Parkinson's <sup>52</sup>	$\alpha$ -synuclein	?	5–10%	~1% of post-50-yr-old population	55–60 yrs
Huntington's <sup>23</sup>	huntingtin	?	100%	1 in 20,000 (Caucasian)	35–40
Familial ALS (Lou Gehrig's disease) <sup>53</sup>	Superoxide dismutase (20% of cases)	Lowers oxidative stress	100% (5–10% of all ALS)	2 in $10^6$	46
Type II diabetes <sup>54</sup>	IAPP	?	High (obesity trigger)	$14 \times 10^6$ per year (U.S.)	>40
Immunoglobulin light chain <sup>55</sup>	IG light chain	Immune response	Small/unknown	1 in $10^5$	64
Prion diseases <sup>35</sup>	PrP <sup>c</sup>	Lowers oxidative stress?	10–15%	~1 in $10^6$	63

\*Incidence/onset age is for non-heritable sporadic disease, unless otherwise noted.

have high quantities of  $\beta$ -sheet structure as revealed by crystallography, circular dichroism (which detects the different light polarization rotation tendencies of  $\alpha$ -helices and  $\beta$ -sheets), and more recently, solid-state magnetic resonance studies. These  $\beta$ -strands are aligned perpendicular to the fibrillar axis, in a so-called "cross- $\beta$ " structure, shown in Figure 1f. Postmortem plaques and inclusions from a variety of

diseases are shown in Figure 1.<sup>13</sup> We note that the amyloid fibrils are protein nanotubes, hollow in the middle, with diameters of the order of 10–20 nm.

Despite a dominant research focus on both structure measurements and computer modeling on plaques, an emerging perspective is that the plaques may represent disease end points having little to do with toxicity.<sup>14</sup> This view is supported by

observations such as (1) the abundant  $\text{A}\beta$  plaques observed in the brains of individuals displaying no symptoms of Alzheimer's disease and (2) the non-uniformity of plaque observation in prion diseases: for example, victims of kuru (a disease among the Fore people of New Guinea, arising from ritual cannibalism of deceased tribe members) exhibit them, while victims of spontaneous Creutzfeldt-Jakob disease usually do not.<sup>15</sup> In this view, toxicity is engendered by small  $\beta$ -sheet aggregates, possibly on the pathway to amyloid fibrils.

## $\beta$ -Helices

Accordingly, attention has turned to small  $\beta$ -sheet motifs with multiple assembly outcomes, especially the left-handed  $\beta$ -helix (LHBH) structures shown in Figure 2,<sup>16</sup> recently proposed as the  $\beta$ -sheet unit for infectious mammalian prion trimers on the basis of cryogenic electron microscopic data.<sup>17</sup> The LHBH  $\beta$ -sheet structure has also been proposed for yeast prion-like proteins,<sup>18</sup> Alzheimer's disease,<sup>19</sup> and Huntington's disease.<sup>16,20</sup> This LHBH motif was first observed in several bacterial enzymes and the "antifreeze" protein of the spruce budworm; to date, there are 11 structures in the protein data bank (<http://www.rcsb.org/pdb/>) confirmed to have LHBHs. LHBHs are usually presumed (or, in two cases, observed)<sup>21,22</sup> to be in protein trimers. The LHBH motif has a fundamental repeat unit of triangular cross section, consisting of 18 amino acids with two per bend region and four per

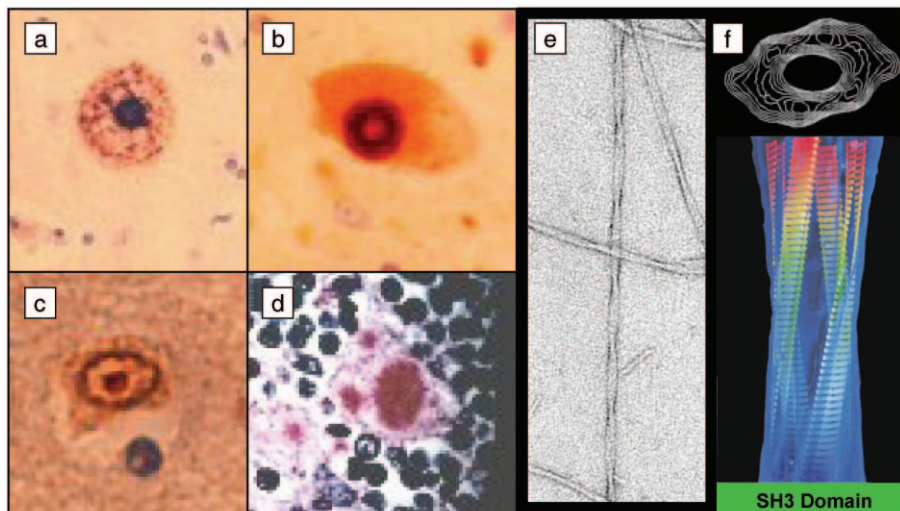


**Figure 1. Plaques and fibrils.** (a)–(d) Postmortem tissue plaques from human amyloid disease patients (from Reference 13): (a)  $\text{A}\beta$ 42 (Alzheimer's) plaque, (b)  $\alpha$ -synuclein (Parkinson's) plaque, (c) huntingtin plaque (Huntington's disease), and (d)  $\text{PrP}^{\text{Sc}}$  (kuru) plaque. (e) Transmission electron microscope images of amyloid fibrils (H. Lashuel, unpublished data). (f) Model of a hollow-core SH3 domain fibril: upper panel shows a density map cross section, lower panel shows the cross- $\beta$  structure.<sup>56</sup>

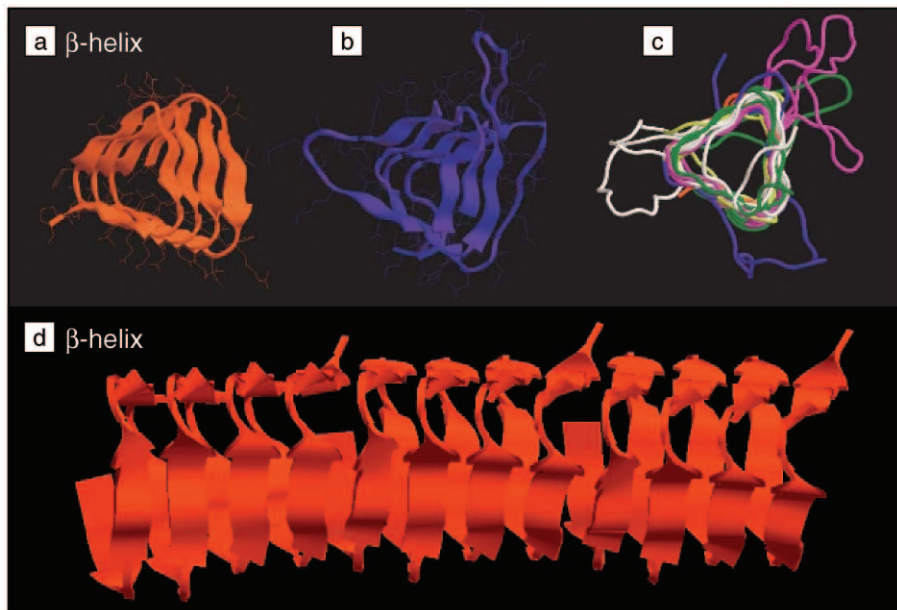


Figure 2. (a) Peptide backbone of measured left-handed  $\beta$ -helix (LHBH) structure of 1FWY protein. (b) Proposed LHBH structure of infectious prion protein (after Reference 16). Parallel, hydrogen-bonded  $\beta$ -sheets are shown as strips. (c) Superposed structure of six LHBH backbones, illustrating the uniform cross section of the helical structure (red, 1FWY protein; blue, proposed infectious prion protein; yellow, 1HMO protein; white, 1J2Z protein; green, 1LOS protein; fuchsia, 1T3D protein). (d) LHBH "nanotube" formed from a stack of three 1FWY helices. All images generated with the RASTOP molecular viewing program (see [www.geneinfinity.org/rastop/](http://www.geneinfinity.org/rastop/)); all files for the proteins 1FWY, 1HMO, 1J2Z, 1LOS, and 1T3D input to RASTOP are from the Protein Data Bank (<http://www.rcsb.org>), except for the  $\text{PrP}^{\text{Sc}}$  model, which is courtesy of C. Govaerts.

$\beta$ -strand, alternating between hydrophobic and hydrophilic in the strand. The triangular cross section is very uniform across observed LHBHs (Figure 2c); each edge is  $\sim 1.9$  nm in length. In Figure 2d, we show how multiple copies of the LHBH of an enzyme from *E. coli* (labeled 1FWY on the protein data base at [www.rcsb.org/pdb](http://www.rcsb.org/pdb)) can be assembled into a kind of  $\beta$ -nanotube. This raises the natural and intriguing question: are amyloid fibrils composed of such "nanofilaments"?<sup>19</sup>

The LHBH has a tantalizing connection to Huntington's and other polyglutamine repeat diseases, where pathology derives from an inherited excess number of repeats of the amino acid glutamine on one end (the N-terminus) of the huntingtin protein.<sup>23</sup> A polyglutamine repeat number  $p$  of less than  $\sim 24$  is normal; for  $p > 36$ , disease is certain. Note that 36 is the number of amino acids or residues in two turns of a LHBH that has fully saturated internal hydrogen bonds.<sup>19</sup>

The LHBH presents a challenge to theory and simulation. At present, this motif has not emerged from any molecular dynamics simulations or semi-analytic (Hamiltonian or cellular automata) ap-

proaches. The complicating factor is the long-range coupling along the backbone (bonded amino acids are separated by 18 residues). On the other hand, the remarkable conservation of the shape and helical cross section suggest that this is a motif ripe for study.

### Nanoscale Oligomers

$\beta$ -sheet oligomers obtained from *in vitro* growth of aggregates have been studied extensively.<sup>13</sup> One common form seems to be a spherical micelle-like aggregate of  $\beta$ -converted proteins, which have been implicated as precursors for the chain-like (protofibril) and annular oligomers that are also seen frequently during *in vitro* amyloid formation by most amyloidogenic proteins.<sup>24</sup> Figure 3 shows a compendium of oligomers and protofibrils from amyloid disease proteins.<sup>25,26</sup> The annular oligomers underlie the proposed toxicity mechanism discussed later in this article. We note that all atomic force microscope (AFM) measurements of spherical, chain-like, and annular oligomers share the same height and diameter, suggesting that the spherical aggregates are the precursors to the larger chain and annular pore-like structures.

The diversity of pre-fibrillar oligomer structures, the formation of which are highly dependent upon protein sequence and environmental conditions (e.g., pH, salt concentration, and levels of molecular crowding), may explain the mystery of prion disease strains. Strains, for a given mammal, have unique incubation-time versus dose distributions, tissue lesion profiles, and distributions of post-translationally attached sugars: the prion protein can have 0, 1, or 2 sugars attached.<sup>27,28</sup> Moreover, strains breed true upon multiple passage in animals. This means that upon passage from a diseased animal to a healthy animal, the same properties (incubation time, lesion profile, sugar binding) are preserved. There is considerable evidence that strain is encoded in prion conformation but no detailed understanding of the underlying mechanisms.<sup>27,28</sup> Prion oligomers<sup>17</sup> might have a spectrum of different shapes, and oriented aggregation of such protein "nanoparticles" might "breed" the conformation true (nonmatching shapes will be energetically unfavorable).

### Domain Swapping

A separate way to generate fibrils and oligomers is by "domain swapping,"<sup>29,30</sup> in which, say, two identical copies (A,B) of a protein exchange a domain (a well-defined protein region attached to a flexible section of peptide). The domain of monomer A binds to the corresponding region of B and vice versa. The swapping is not limited to dimers; it can lead to filamentary structures in which the  $i$ th protein swaps with the  $(i + 1)$ th protein, for example, closed-chain oligomers (where filament ends are brought together to domain-swap) or two-dimensional structures.

Domain swapping has been proposed to play a role in prion strains.<sup>31</sup> Domain swapping in protein–protein interactions generically and amyloid diseases in particular seems certain to emerge as a critical theme in the coming years. At the conceptual level, the study of coarse-grained protein models with molecular dynamics has shown that the formation of domain-swapped dimers will proceed down a funneled landscape if the dimer enjoys minimal frustration.

### Aggregation Pathways and Kinetics

AFM and kinetic modeling, well known to materials scientists, have been instrumental in advancing our understanding of the structural properties of the protein aggregates linked to disease and their growth kinetics. Figure 4 schematically shows accepted models on amyloid conversion/aggregation kinetics. We note

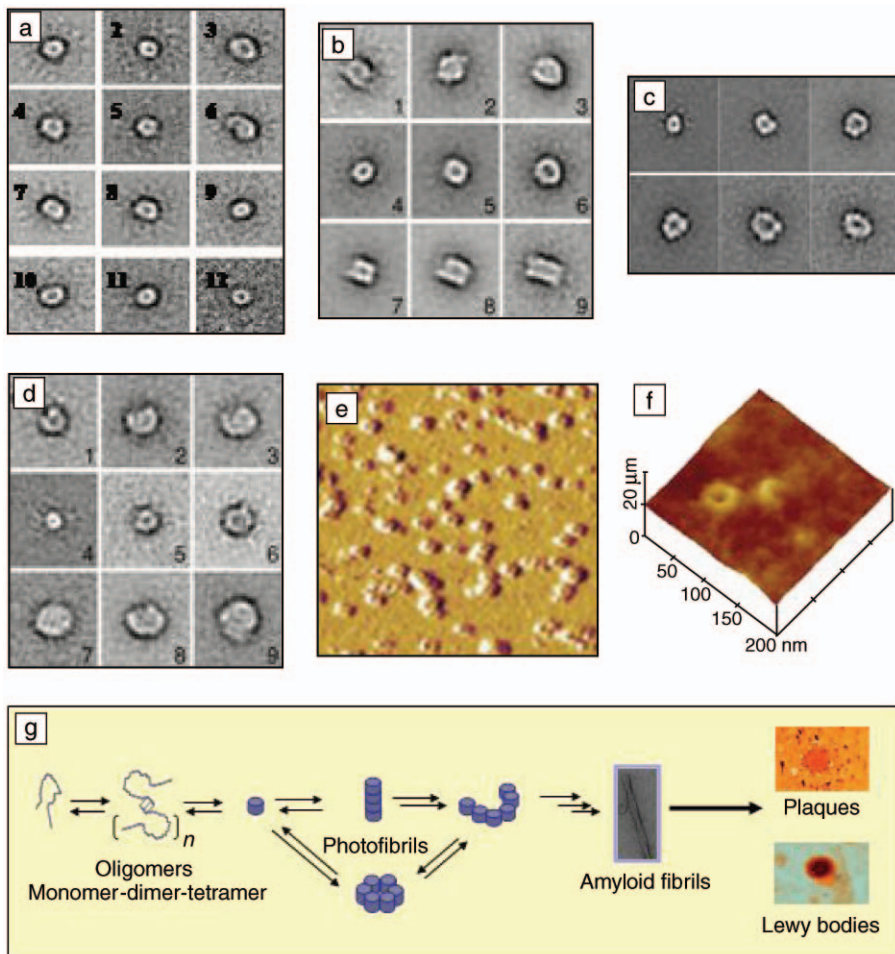


**Figure 3. Amyloid oligomers.** (a)  $\text{A}\beta$  peptide implicated in Alzheimer's disease, observed by electron microscopy (scale, 50 nm/box) (from Reference 24). (b) Nine different oligomers of mutant  $\alpha$ -synuclein, implicated in Parkinson's disease, observed by electron microscopy (scale, 40.5 nm/box) (from Reference 25). (c) Six oligomers of mutant SOD1, implicated in familial ALS (from Reference 56).<sup>57</sup> (d) Nine mutant  $\alpha$ -synuclein oligomers (scale, 40.5 nm/box) (from Reference 25). (e) Atomic force microscope (AFM) images of  $\text{A}\beta$  oligomers inserted in a supported lipid bilayer (from Reference 26). Clearly resolved annular oligomers have outer diameters of  $\sim 16$  nm. (f) AFM image of  $\alpha$ -synuclein oligomer on supported lipid bilayer (from Reference 25). (g) Schematic illustration of oligomerization pathways. Here, the subscript  $n$  in the second stage represents the number of monomers in an oligomer.

that  $\beta$ -sheet conversion is typically concomitant with aggregation (i.e., conformational changes and protein assembly are linked),<sup>32,33</sup> with the possible exception of polyglutamine proteins,<sup>34</sup> and requires templating either by spontaneously formed (and rare) nuclei or by external seeding of aggregates.<sup>33</sup> Also, fission of mammalian prions is necessary for disease propagation and exponentially growing aggregates in mammals; prion-like proteins in yeast have fission effected by another protein<sup>35</sup> (although the fission can occur spontaneously *in vitro*).<sup>36</sup> Why mammalian prions fission and other amyloidogenic proteins do not remain a mystery.

*In vitro* and theoretical studies of conversion/aggregation suggest that the late-

age onset in amyloid diseases derives from slow underlying molecular processes. For example, *in vitro* kinetics experiments for polyglutamine peptides extrapolated to *in vivo* concentrations of huntingtin protein suggest that within the "sampling window" of a human lifespan, toxic aggregate concentrations should arise only for glutamine number  $p > 36$ , consistent with clinical observations.<sup>34</sup>

For prion diseases, theoretical modeling of two-dimensional aggregation and fission (prions live mostly on neuronal membranes) yielded a sporadic incubation time distribution that peaked at  $\sim 100$  times that obtained from dilute seeding for physiological concentrations of the normally expressed protein called  $\text{PrP}^c$

that misfolds in the diseased form.<sup>37</sup> Given a mean incubation time for kuru of 12 years,<sup>38</sup> this suggests that endemic sporadic prion disease requires  $\sim 1000$ -year life spans! Meanwhile, the  $1 \times 10^6$  sporadic disease background incidence may reflect the low-amplitude, pre-peak tail in the incubation time distribution.<sup>38</sup>

## Amyloid–Membrane Interaction and Toxicity

Many amyloidogenic proteins associate with lipid membranes. AFM studies on supported bilayers and molecular modeling have helped support a potential unifying hypothesis for amyloid disease toxicity: that small oligomers pierce cell membranes, triggering cell death through superfluous ion pores. It was proposed in detail that a pair of  $\beta$ -coupled annular tetramers of  $\text{A}\beta$  peptides can insert into the neuronal membrane leaflets and create an ion pore.<sup>39</sup> *In vitro*-grown oligomers qualitatively consistent with this hypothesis have been found (Figure 3) and studied with AFM on supported bilayers (Figure 3f); these are evidently composed of 4 nm spherical oligomers, much larger than the peptide tetramers of Reference 39. These oligomers permit excess calcium flux, which is toxic to cultured neurons.<sup>26</sup> Intracerebral inoculation of rats and mice with a solution presumed rich in oligomeric  $\text{A}\beta$  particles leads to a reversible short-term memory deficit.<sup>40</sup> A recent theoretical study found strong correlations between the membrane insertion configuration and the pore model for 4 of 5 mutations leading to early-onset Alzheimer's disease.<sup>41</sup> While the pore model is not universally accepted, and may not apply to all the diseases (the prion trimer model, for example, will not allow ion passage), it remains a vibrant area of research.

## Amyloids for Good in Biology and Materials Science Biologically Useful Amyloids

Emerging evidence suggests that amyloid structures can provide useful biological functions. Some examples are

1. *Heritable amyloid structure in yeast.* As alluded to previously, prion-like proteins in yeast form aggregates that fission upon cell division, can actively confer phenotype, and may provide some stress protection.<sup>42</sup>

2. *Spider silk.* Spiders produce insoluble filaments of fibroin protein that possess 30 $\times$  greater extensibility and toughness than steel. Recent circular dichroism studies show that significant amyloid-like cross- $\beta$  structure develops in a region of reduced

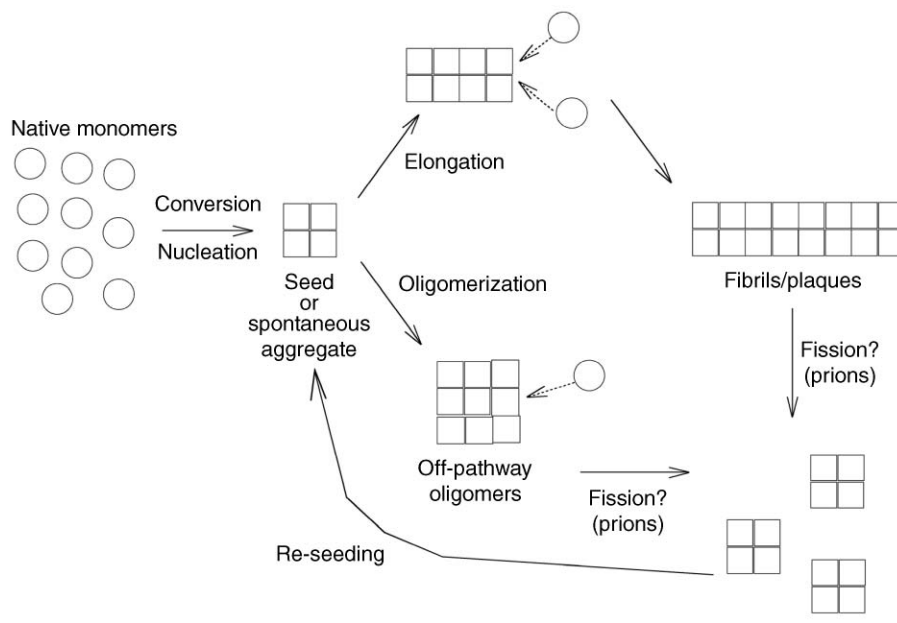


**Figure 4.** Schematic illustration of amyloid conversion and aggregation. Native monomers of the relevant peptides or proteins are shown as circles and high- $\beta$ -content converted proteins as squares. Peptides can either spontaneously convert or be seeded. Subsequent aggregation and conversion can generate either proto-fibrils via the elongation step, which then form amyloid fibrils and plaques, or pass to “off-pathway” oligomers. In the case of prions, the oligomers and/or fibrils can fission, which then re-seeds the initial conversion/aggregation process. Prions are the only known amyloid proteins to spontaneously fission in the converted form either *in vitro* or *in vivo*. It is assumed (but not shown explicitly here) that both oligomers and native monomers experience some level of removal by cellular systems *in vivo*.

pH downstream from the initial extrusion site.<sup>43</sup>

3. *Chorion in fish and insect egg shells.* Truncated peptides from the central regions of two chorion proteins self-assembled into spherulites possessing  $\beta$ -structure, which then converted to fibrils upon maturation, suggesting amyloid character in actual egg shells.<sup>44</sup>

4. *Amyloid-like structure in synapses of Aplysia (slugs).* The N-terminus region of the *Aplysia* synapse protein CPEB is glutamine-rich, like huntingtin protein. Engineered expression of CPEB in yeast yields prion-like aggregates similar to the native ones discussed earlier; hence, prion-like states of CPEB might effect long-term strengthening of synaptic contacts.<sup>45</sup>

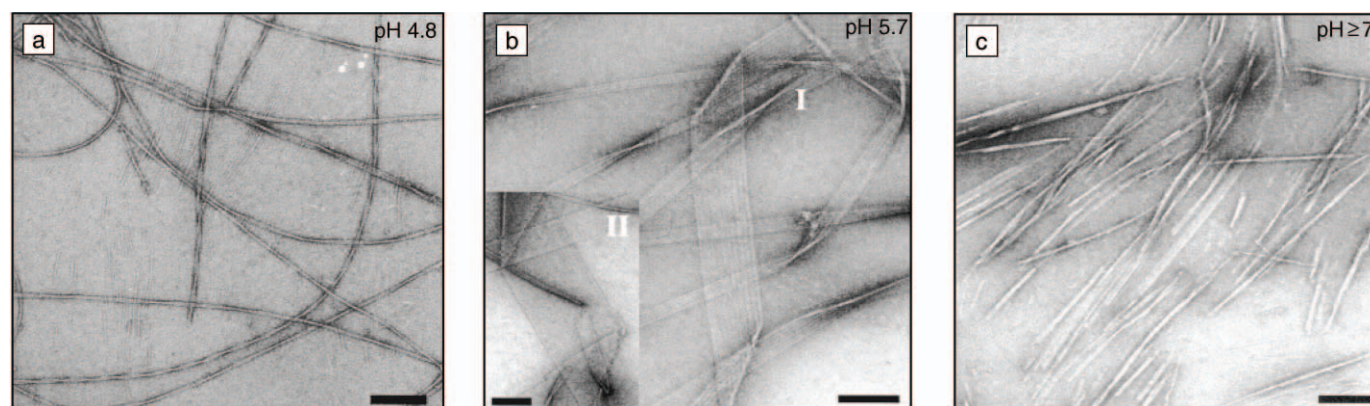


**Figure 5.** (a)–(c) Images from electron microscopy showing pH-dependent fibril growth of designed peptidomimetic molecules (from Reference 49). Scale bars are 100 nm.

### Amyloids in Materials Science

The regular diameter and periodicity of the amyloid fibrils make them good materials templates. One group employed yeast prion-like proteins to template ~100-nm-wide gold nanowire growth; the gold-coated protein filaments after initial decoration by small gold nanoparticles were found to bind to genetically engineered cysteine residues.<sup>46</sup> Silver nanowires of 20 nm width were grown *inside* filamentary cross- $\beta$  tubes grown from a diphenylalanine peptide.<sup>47</sup> Engineering of controllably switched  $\beta$ -sheet materials could prove valuable for tissue growth scaffolding, as one example.<sup>48</sup> Hybrid molecules including eight amino acids—four per strand, but with non-amino bonds—have been developed that controllably self-assemble into different  $\beta$ -sheet structures (as shown in Figure 5) depending upon the pH, analogous to spider silk.<sup>49</sup> Clearly, the future of engineered amyloid structures in materials science looks bright.<sup>50</sup>

### Conclusion

In this article, we have developed themes that bring together the fields of amyloid diseases and materials science. Protein misfolding and aggregation phenomena are intimately linked to many serious public health issues. However, many aspects of the phenomena have close analogies in synthesized materials, and their full molecular understanding requires experimental and modeling tools more familiar in the physical and materials sciences. In addition to the possible medical breakthroughs that such multidisciplinary studies can lead to, there is a growing possibility that understanding the mechanisms of amyloid formation can have wide impact in fields ranging from basic neurobiology to materials science.

## Acknowledgments

D.L. Cox and R.R.P. Singh acknowledge the support of the U.S. Army Congressionally Directed Medical Research Fund, grant NP02013. D.L. Cox thanks the NSF Center for Theoretical Biological Physics, grant PHY 0120999, and S. Yang, H. Levine, and J. Onuchic for many useful discussions. We thank C. Govaerts for sharing the coordinates of the model prion trimer and R. Lal for sharing the second paper in Reference 26 prior to publication. This article is reflective of scientific discussions and presentations from two workshops on the physical properties of amyloids sponsored by the Institute for Complex Adaptive Matter (San Francisco, November/December 2001; Boston, February 2004).

## References

1. B.H. Zimm and J.K. Bragg, *J. Chem. Phys.* **31** (1958) p. 526.
2. S. Lifson and A.J. Roig, *J. Chem. Phys.* **34** (1961) p. 1963.
3. L. Pauling, R.B. Corey, and H.R. Branson, *Proc. Natl. Acad. Sci. USA* **37** (1951) p. 205.
4. P.G. Wolynes, J.N. Onuchic, and D. Thirumalai, *Science* **267** (1995) p. 1619; J.N. Onuchic and P.G. Wolynes, *Curr. Opin. Struct. Biol.* **14** (2004) p. 70.
5. M. Stefani and C.M. Dobson, *J. Mol. Med.* **81** (2003) p. 678.
6. P.S. Lee and K.H. Lee, *Biotech. Bioeng.* **89** (2004) p. 195.
7. J.E. Bear, M. Krause, and F.B. Gertler, *Curr. Opin. Cell. Biol.* **13** (2001) p. 158; S. Inouye, *J. Struct. Biol.* **118** (1997) p. 87.
8. P.L. Clark, *Trends Biochem. Sci.* **29** (2004) p. 527.
9. S.B. Prusiner, J. Safar, and S.J. DeArmond, in *Prion Biology and Diseases* (Cold Spring Harbor Laboratory Press, Cold Spring Harbor, NY, 2004) p. 143.
10. G. Legname, I.V. Baskakov, H.-O.B. Nguyen, D. Riesner, F.E. Cohen, S.J. DeArmond, S.B. Prusiner, *Science* **306** (2004) p. 673.
11. R.L. Penn, *J. Phys. Chem. B* **108** (2004) p. 12707.
12. P.H. St. George-Hyslop, *Sci. Am.* **283** (2000) p. 76.
13. All plaque/inclusion images are from the laboratory of M. Feany, <http://feany-lab.bwh.harvard.edu/link2/> (accessed April 2005).
14. B. Caughey and P.T. Lansbury Jr., *Annu. Rev. Neurosci.* **26** (2003) p. 267.
15. S. J. deArmond, J.W. Ironside, E. Bouzamondo-Bernstein, D. Peretz, and J.R. Fraser, in *Prion Biology and Diseases* (Cold Spring Harbor Laboratory Press, Cold Spring Harbor, NY, 2004) p. 777.
16. J. Jenkins and R. Pickersgill, *Prog. Biophys. Mol. Biol.* **77** (2001) p. 111.
17. C. Govaerts, H. Wille, S.B. Prusiner, and F.E. Cohen, *Proc. Natl. Acad. Sci. USA* **101** (2004) p. 8342.
18. A. Kishimoto, K. Hasegawa, H. Suzuki, H. Taguchi, K. Namba, and M. Yoshida, *Biochem. Biophys. Res. Commun.* **315** (2004) p. 739.
19. J.-T. Guo, R. Wetzel, and Y. Xu, *Proteins: Struct. Funct. Bioinformatics* **57** (2004) p. 357.
20. M.F. Perutz, J.T. Finch, J. Berriman, and A. Lesk, *Proc. Natl. Acad. Sci. USA* **99** (2002) p. 5591; R. Wetzel, *Structure* **10** (2002) p. 1031.
21. V.E. Pye, A.P. Tingey, R.L. Robson, and P.C.E. Moody, *J. Biol. Chem.* **279** (2004) p. 40729.
22. C. Kisker, H. Schindelin, B.E. Alber, J.G. Ferry, and D.C. Rees, *EMBO J.* **15** (1996) p. 2323.
23. H.Y. Zoghbi and H.T. Orr, *Annu. Rev. Neurosci.* **23** (2000) p. 217.
24. H.A. Lashuel, D.M. Hartley, B.M. Petre, J.S. Wall, M.N. Simon, T. Walz, and P.T. Lansbury, *J. Mol. Biol.* **332** (2003) p. 795.
25. H.A. Lashuel, B.M. Petre, J. Wall, M. Simon, R.J. Nowak, T. Walz, P.T. Lansbury, *J. Mol. Biol.* **322** (2002) p. 1089.
26. A. Parbhoo, H. Lin, J. Thimm, and R. Lal, *Peptides* **23** (2002) p. 1265; A. Quist, I. Doudevski, H. Lin, R. Azimova, D. Ng, B. Frangione, B. Kagan, J. Ghiso, and R. Lal, et al., preprint submitted to *Nat. Struct. Biol.* (2005).
27. S.B. Prusiner, M.R. Scott, S.J. DeArmond, and G. Carlson, in *Prion Biology and Diseases* (Cold Spring Harbor Laboratory Press, Cold Spring Harbor, NY, 2004) p. 187.
28. M. Scott, D. Peretz, R.M. Ridley, H.F. Baker, S.J. DeArmond, and S.B. Prusiner, in *Prion Biology and Diseases*, Cold Spring Harbor Laboratory Press, Cold Spring Harbor, NY (2004) p. 435.
29. M.J. Bennett, M.P. Schlunegger, and D. Eisenberg, *Protein Sci.* **4** (1995) p. 2455; M.P. Schlunegger, M.J. Bennett, and D. Eisenberg, *Adv. Protein Chem.* **50** (1997) p. 61; Y. Liu, G. Gotte, M. Libonatti, and D. Eisenberg, *Nat. Struct. Biol.* **8** (2001) p. 211.
30. S.C. Yang, S.S. Cho, Y. Levy, M.S. Cheung, H. Levine, P.G. Wolynes, J.N. Onuchic, *Proc. Natl. Acad. Sci. USA* **101** (2004) p. 13786.
31. F.E. Cohen and S.B. Prusiner, *Annu. Rev. Biochem.* **67** (1998) p. 793.
32. T.R. Serio, A.G. Cashikar, A.S. Kowal, G.J. Sawicki, J.J. Moslehi, L. Serpell, M.F. Arnsdorf, and S.L. Lindquist, *Science* **289** (2000) p. 1317.
33. S. Chen, F.A. Ferrone, and R. Wetzel, *Proc. Natl. Acad. Sci. USA* **99** (2002) p. 11884.
34. J. Masel, V.A.A. Jansen, and M.A. Nowak, *Biophys. Chem.* **77** (1999) p. 139.
35. P. Chien, J.S. Weissman, and A.H. DePace, *Annu. Rev. Biochem.* **73** (2004) p. 617.
36. S.R. Collins, A. Douglass, R.D. Vale, and J.S. Weissman, *PLoS Biol.* **2** (2004) p. 1582.
37. A. Slepoy, R.R.P. Singh, F. Pazmandi, R.V. Kulkarni, and D.L. Cox, *Phys. Rev. Lett.* **87** 058101 (2001).
38. R.G. Will, M.P. Alpers, D. Dormont, and L.B. Schonberger, in *Prion Biology and Diseases* (Cold Spring Harbor Laboratory Press, Cold Spring Harbor, NY, 2004) p. 629.
39. N. Arispe, H. B. Pollard, and E. Rojas, *Proc. Natl. Acad. Sci. USA* **90** (1993) p. 10573; N. Arispe, H.B. Pollard, and E. Rojas, *Mol. Cell. Biochem.* **140** (1994) p. 119; S.R. Durell et al., *Biophys. J.* **67** (1994) p. 2137.
40. D.M. Walsh, I. Klyubin, J.V. Fadeeva, W.K. Cullen, R. Anwyl, M.S. Wolfe, M.J. Rowan, and D.J. Selkoe, *Nature* **416** (2002) p. 535.
41. D.L. Mobley, D.L. Cox, R.R.P. Singh, M.W. Maddox, and M.L. Longo, *Biophys. J.* **86** (2004) p. 3585.
42. H.L. True, I. Berlin, and S.L. Lindquist, *Nature* **431** (2004) p. 184.
43. C. Dicko, F. Vollrath, and J.M. Kenney, *Biomacromolecules* **5** (2004) p. 704.
44. S.J. Hamodrakas, A. Hoenger, and V.A. Iconomidou, *J. Struct. Biol.* **145** (2004) p. 226.
45. K. Si, S. Lindquist, and E.R. Kandel, *Cell* **115** (2004) p. 879.
46. T. Scheibel, R. Parthasarathy, G. Sawicki, X.M. Lin, H. Jaeger, and S.L. Lindquist, *Proc. Natl. Acad. Sci. USA* **100** (2003) p. 4527.
47. M. Reches and E. Gazit, *Science* **300** (2003) p. 625.
48. C.E. MacPhee and D.N. Woolfson, *Curr. Opin. Solid State Mater. Sci.* **8** (2004) p. 141.
49. H.A. Lashuel, S.R. LaBrenz, L. Woo, L.C. Serpell, J.W. Kelly, *J. Am. Chem. Soc.* **122** (2000) p. 5262.
50. S.H. Waterhouse and J.A. Gerrard, *Aust. J. Chem.* **57** (2004) p. 519.
51. S. Gao, H.C. Hendrie, K.S. Hall, and S. Hui, *Arch. Gen. Psychiatry* **55** (1998) p. 809.
52. S.C. Conley and J.T. Kirchner, *Postgrad. Med. Online* **106** (1) (1999), [http://www.postgradmed.com/issues/1999/07\\_99/conley.htm](http://www.postgradmed.com/issues/1999/07_99/conley.htm) (accessed April 2005).
53. M.J. Strong, A.J. Hudson, and W.G. Alvord, *Can. J. Neurol. Sci.* **18** (1991) p. 45.
54. S.R. Votey and A.L. Peters, "Diabetes Mellitus, Type II—A Review," <http://www.emedicine.com/emerg/topic134.htm> (accessed April 2005).
55. R.H. Falk, R.L. Comenzo, and M. Skinner, *New Eng. J. Med.* **337** (1997) p. 898.
56. J.L. Jimenez, J.I. Guijarro, E. Orlova, J. Zurdo, C.M. Dobson, M. Sunde, H.R. Saibil, *EMBO J.* **18** (1999) p. 815.
57. S.S. Ray, R.J. Nowak, K. Strokovich, R.H. Brown, T. Walz, and P.T. Lansbury, *Biochem. U.S.* **43** (2004) p. 4899. □

## Advertisers in This Issue

### Page No.

Cougar Labs, Inc.	Inside back cover
High Voltage Engineering	Inside front cover
Huntington Mechanical Labs, Inc.	Outside back cover
Janis Research Company, Inc.	432
MTS Systems Corporation	458
Shiva Technologies, Inc.	451

For free information about the products and services offered in this issue, check <http://advertisers.mrs.org>

[Yahoo!](#) [My Yahoo!](#) [Mail](#) Welcome, **dlcox1958** [Sign Out, [My Account](#)]

[News Home](#) [Search Home](#) [Help](#)



[Web](#) | [Images](#) | [Video](#) | [Directory](#) | [Local](#) | **News** | [Shopping](#)

Cox Singh "mad cow"

Show: [All Topics](#) | from: [last month](#) | from: [all sources](#) | from: [all locations](#) | in

[Subscriptions \(New\)](#) [Advanced Search](#) [Preferences](#)

## News Results

[Got feedback?](#) | [Suggest a Site](#)

**NEWS STORIES** Results 1 - 18 of about 18 for Cox Singh "mad cow".

[Sort Results by:](#)

1. [California researcher finds that mad cow infection spreads rapidly](#)  
<sub>Scottsbluff Star-Herald - Jun 16 8:06 AM</sub>

DAVIS, Calif. (AP) - Researchers at the University of California, Davis are trying to explain how **mad cow** so frighteningly fast.

2. [Modeling to Understand Mad Cow Disease](#)  
<sub>SAP Info - Jun 16 2:15 AM</sub>

Two physics professors at the University of California Davis, who have been researching **mad cow** disease use computerized mathematical models to explain how the disease acts so fast.

3. [Researchers explore spread of mad cow disease](#)  
<sub>CTV.ca - Jun 15 4:49 PM</sub>

DAVIS, Calif. — Researchers at the University of California, Davis are trying to explain how **mad cow** disease frighteningly fast using an unconventional tool mathematical modeling.

4. [UC Researchers Explore Spread of Mad Cow](#)  
<sub>TechNewsWorld.com - Jun 15 8:27 AM</sub>

Scientists believe the human body usually rejects misfolded proteins without harm; it's when a microscopically flawed proteins is consumed from another animal that the disease can take hold in a person or animal who would never develop the disease.

5. [The Capital City's Newspaper Online](#)  
<sub>Independent Record - Jun 14 11:12 PM</sub>

AP photo - Rajiv **Singh**, a physics professor at the University of California Davis, holds up a slide showing of a human protein cell at his campus office in Davis, Calif., on Tuesday.

6. [Mad cow computer modeling finds infection spreads rapidly](#)  
<sub>Billings Gazette - Jun 15 7:31 AM</sub>

DAVIS, Calif. -- Researchers at the University of California, Davis are trying to explain how **mad cow** disease frighteningly fast using an unconventional tool -- mathematical modeling.

7. [Mad cow computer modeling finds infection spreads rapidly](#)  
<sub>Billings Gazette - Jun 15 7:32 AM</sub>

DAVIS, Calif. -- Researchers at the University of California, Davis are trying to explain how **mad cow** disease frighteningly fast using an unconventional tool -- mathematical modeling.

8. [UC Researchers Explore Spread of Mad Cow](#)  
<sub>First Coast News - Jun 15 10:04 AM</sub>

DAVIS, CA (AP) -- Researchers at the University of California, Davis are trying to explain how **mad cow** disease frighteningly fast using an unconventional tool - mathematical modeling.

9. [Mad cow computer modeling finds infection spreads rapidly](#)  
<sub>Billings Gazette - Jun 15 7:32 AM</sub>

[SanLuisObispo.com](#) - Jun 15 3:35 AM

73

DAVIS, Calif. - Researchers at the University of California, Davis are trying to explain how **mad cow** disease frighteningly fast using an unconventional tool - mathematical modeling.

10. [UC researchers explore spread of mad cow](#) 

[Kansas City Star](#) - Jun 15 5:20 AM

DAVIS, Calif. - Researchers at the University of California, Davis are trying to explain how **mad cow** disease frighteningly fast using an unconventional tool - mathematical modeling.

11. [UC Researchers Explore Spread of Mad Cow](#) 

[RedNova](#) - Jun 15 7:26 AM

DAVIS, Calif. -- Researchers at the University of California, Davis are trying to explain how **mad cow** disease frighteningly fast using an unconventional tool - mathematical modeling.

12. [UC researchers explore spread of mad cow](#) 

[The Times Leader](#) - Jun 15 5:18 AM

DAVIS, Calif. - Researchers at the University of California, Davis are trying to explain how **mad cow** disease frighteningly fast using an unconventional tool - mathematical modeling.

13. [UC researchers explore spread of mad cow](#) 

[Macon Telegraph](#) - Jun 15 5:28 AM

DAVIS, Calif. - Researchers at the University of California, Davis are trying to explain how **mad cow** disease frighteningly fast using an unconventional tool - mathematical modeling.

14. [Mad cow computer modeling finds infection spreads rapidly](#) 

[Monterey County Herald](#) - Jun 15 3:29 AM

DAVIS, Calif. - Researchers at the University of California, Davis are trying to explain how **mad cow** disease frighteningly fast using an unconventional tool - mathematical modeling.

15. [UC researchers explore spread of mad cow](#) 

[TimesLeader.com](#) - Jun 15 5:08 AM

DAVIS, Calif. - Researchers at the University of California, Davis are trying to explain how **mad cow** disease frighteningly fast using an unconventional tool - mathematical modeling.

16. [Mad cow computer modeling finds infection spreads rapidly](#) 

[The Times Leader - Technology](#) - Jun 15 5:48 AM

DAVIS, Calif. (AP) - Researchers at the University of California, Davis are trying to explain how **mad cow** disease so frighteningly fast using an unconventional tool -- mathematical modeling.

17. [UC Researchers Explore Spread of Mad Cow](#) 

[WJLA-TV Washington D.C.](#) - Jun 15 6:08 AM

DAVIS, Calif. (AP) - Researchers at the University of California, Davis are trying to explain how **mad cow** disease ( news ) acts so frighteningly fast using an unconventional tool - mathematical modeling.

18. [UC researchers explore spread of mad cow](#) 

[Kansas City Star](#) - Jun 15 5:27 AM

DAVIS, Calif. - Researchers at the University of California, Davis are trying to explain how **mad cow** disease frighteningly fast using an unconventional tool - mathematical modeling.

---

YAHOO! NEWS by category

[News Home](#)

[World](#)

[Politics](#)

[Op/Ed](#)

[Most Popular](#)

[Top Stories](#)

[Entertainment](#)

[Local](#)

[Weather](#)

[U.S. National](#)

[Sports](#)

[Comics](#)

[Audio/Video](#)

[Business](#)

[Technology](#)

[Oddly Enough](#)

[News Photos](#)

[Full Coverage](#)

[Web](#) | [Images](#) | [Video](#) | [Directory](#) | [Local](#) | **News** | [Shopping](#)

Your Search:

Show: | [All Topics](#) | from: [last month](#) | from: [all sources](#) | from: [all locations](#) | in [English](#)

Copyright © 2005 Yahoo! Inc. All rights reserved. [Privacy Policy](#) - [Terms of Service](#) - [Copyright/IP Policy](#) - [Ad Feedback](#)